Title
Predicting coastal waves with buoy observations and global model output, a Southern California case study

Author
Crosby, Sean Christopher

Publication Date
2017

Peer reviewed|Thesis/dissertation

UNIVERSITY OF CALIFORNIA, SAN DIEGO

Predicting coastal waves with buoy observations and global model output: a Southern California case study

A dissertation submitted in partial satisfaction of the
requirements for the degree
Doctor of Philosophy

in

Oceanography

by

Sean Christopher Hunter Crosby

Committee in charge:

Robert T. Guza, Chair
Bruce D. Cornuelle
Falk Feddersen
Eugene R. Pawlak
Robert Pinkel

2017

The dissertation of Sean Christopher Hunter Crosby is approved, and it is acceptable in quality and form for publication on microfilm and electronically:

Chair

University of California, San Diego

2017

DEDICATION

To my family,

who have always supported me,

no matter my direction.

EPIGRAPH

All that in idea seemed simple became in practice immediately complex; as the waves shape themselves symmetrically from the cliff top, but to the swimmer among them are divided by steep gulfs, and foaming crests.

—Virginia Woolf, 1927

TABLE OF CONTENTS

LIST OF FIGURES

LIST OF TABLES

ACKNOWLEDGEMENTS

I owe many thanks to my thesis advisor Bob Guza, he instilled in me the importance of details (the devil's residence) and clarity (a weak point of mine). Guza also insisted that time was my most valuable asset; however, it is only now (at the 11th hour) I believe him. I also thank my coauthors, Bill O'Reilly and Bruce Cornuelle, who have shared with me their knowledge and helped steer my research in productive directions. And thanks to Falk Feddersen, Rob Pinkel, and Geno Pawlak for serving on my committee and helping shape my work. I am fortunate to have studied at Scripps Institution of Oceanography (SIO), the vibrant research community has shaped my education. My professors including, Clint Winant, Lynn Talley, Robert Pinkel, Myrl Hendershott, Jennifer MacKinnon, Dean Reommich, Bill Young, Falk Feddersen, Bob Guza, Peter Franks, and Cathy Constable all taught excellent courses that I will always refer to.

I owe many thanks to the SIO student community: My awesome PO cohort, Julia Fiedler, Martha Schonau, and Spencer Jones; I would not have survived first year classes without you. My CCS basement colleagues, Bonnie Ludka, Matt Spydell, Greg Sinnet, Dereck Grimes, Nirnimesh Kumar, and Ata Suanda; always providing engaging scientific discussion, and keeping me sane during our many years in the dark and damp. Additionally, many thanks to Julia and Bonnie, my co-teachers of ”Physics of the Ocean World” summer course.

I also thank my loving partner Eiren Jacobson, for her unwavering support and understanding. And to my family for understanding my need to stay in school another five and a half years.

This study was funded by the California Department of Parks and Recreation, Division of Boating and Waterways Oceanography Program, the United States Army Corps of Engineers, and the California Sea Grant Traineeship Program.

Chapter 2, in full, is a reprint with some additions and modifications of the paper,

”Modeling Long-Period Swell in Southern California: Practical Boundary Conditions from Buoy Observations and Global Wave Model Predictions” published in the Journal of Atmospheric and Oceanic Technology by S. C. Crosby, W. C. O’Reilly, and R. T. Guza in 2016. The dissertation/thesis author was the primary investigator and author of this paper.

Chapter 3, in full, is a reprint with some additions and modifications of the paper, ”Assimilating global wave model predictions and deep water wave observations in nearshore swell predictions” that is currently under review by the Journal of Atmospheric and Oceanic Technology. Authors include by S. C. Crosby, B. D. Cornuelle, W. C. O’Reilly, and R. T. Guza. The dissertation/thesis author was the primary investigator and author of this paper.

VITA

2009	B. S. Applied Physics, B. A. Economics, *Cum Laude* University of California, Santa Cruz
2013	M. S. Oceanography, Scripps Institution of Oceanography, University of California, San Diego
2017	Ph. D. Oceanography, Scripps Institution of Oceanography, University of California, San Diego

PUBLICATIONS

Crosby, S. C., B. D. Corunelle, W. C. O'Reilly, and R. T. Guza, Assimilating global wave model predictions and deep water wave observations in nearshore swell predictions, *J. Atmospheric and Oceanic Tech.*, Submitted 1/5/2017, in review.

Kumar, N., D. L. Cahl, S. C. Crosby, G. Voulgaris, Bulk vs. Spectral Wave Parameters: Implications on Stokes Drift Estimates, Regional Wave Modeling, and HF RadarsApplications, *J. Physical Oceanography*, Accepted 2017, in press.

Crosby, S. C., W. C. O'Reilly, and R. T. Guza, Modeling long period swell in southern California: practical boundary conditions from buoy observations and global wave model predictions, *J. Atmospheric and Oceanic Tech.*, 2016.

Ludka, B. C., T. Gallien, S. C. Crosby, and R. T. Guza. Mid-El Nino erosion at nourished and unnourished southern California Beaches, *Geophysical Research Letters*, 2016.

Collier K., T. Cunnington, S. C. Crosby, V. Fadeyev, F. Martinez-McKinney, K. Mistry, B. A. Schumm, E. Spencer, A. Taylor, M. Wilder. Microstrip electrode readout noise for load-dominated long shaping-time systems, *Nucl. Instr. Meth. Phys. Res.*, Vol. 729, 2013.

PRESENTATIONS

Crosby, S. C., B. D. Cornuelle W. C. O'Reilly, R. T. Guza. Assimilating coastal wave buoy observations and global wave model predictions in regional wave models.. *Oral presentation the American Geophysical Union Fall Meeting*, San Francisco, CA, Dec 2016.

Rhee K., S. C. Crosby, J. W. Fiedler. Observations of High-frequency Internal Wave Energy Offshore of Point Loma, California. *American Geophysical Union Fall Meeting*, New Orleans, LA, Dec 2016.

Fiedler J. W., V. M. Tamsitt, S. C. Crosby,, B. C. Ludka. Experiential Learning: High School Student Response to Learning Oceanography at Sea. *American Geophysical Union Fall Meeting*, New Orleans, LA, Dec 2016.

Crosby, S. C., B. D. Cornuelle W. C. O'Reilly, R. T. Guza. Combining global wave model predictions and regional buoy observations: a Southern California case study. *Invited seminar at US Army Corps of Engineers*, Vicksburg, MI, Nov 2016.

Crosby, S. C., B. D. Cornuelle W. C. O'Reilly, R. T. Guza. Assimilating coastal wave buoy observations and global wave model predictions in regional wave models. *Oral presentation at Eastern Pacific Ocean Conference*, Mt. Hood, Oregon, Sept 2016. *Awarded best student presentation*

Crosby, S. C., W. C. O'Reilly, R. T. Guza. Modeling long period swell in southern California: Practical boundary conditions from buoy observations and global wave model predictions. *Poster presentation at Ocean Sciences Meeting*, New Orleans, LA, Feb 2016.

Crosby, S. C., W. C. O'Reilly, R. T. Guza. Regional Nearshore Wave Prediction: A Sediments Perspective. *Oral presentation at Coastal Sediments*, San Diego, CA, May 2015.

Crosby, S. C., W. C. O'Reilly, R. T. Guza. Improved Temporal Smoothing for Wave Buoy Observations, *Poster presentation at American Geosciences Union Fall Meeting*, San Francisco, CA, Dec 2014

Crosby, S. C., W. C. O'Reilly, R. T. Guza. Improving Coastal Wave Estimates by Combining Buoy Observations with Global Wave Models. *Oral presentation at Ocean Sciences Meeting*, Honolulu, Hawaii, Feb 2014.

ABSTRACT OF THE DISSERTATION

Predicting coastal waves with buoy observations and global model output: a Southern California case study

by

Sean Christopher Hunter Crosby

Doctor of Philosophy in Oceanography

University of California, San Diego, 2017

Robert T. Guza, Chair

Accurate coastal wave predictions are needed to support nearshore process modeling (transport, erosion) and local risk assessment (flooding, inundation). Small errors in direction or frequency have relatively large impacts to transport, run-up estimates. Nearshore prediction error is often dominated by offshore uncertainties in regional models. Detailed, frequency-direction, spectra are needed offshore to accurately estimate blocking and refraction in sheltered regions, e.g. the Southern California Bight (SBC).

Here, nearshore prediction skill using both global wave model predictions and offshore buoy observations in the offshore boundary condition is compared for swell-

band wave energy (0.04-0.09Hz). Despite inherent directional ambiguity, offshore buoy observations yield a more accurate boundary condition. Analytical and ah hoc combinations global model predictions and offshore buoy observations are tested and yield worse and marginally improved predictions respectively (as compared to buoy-driven predictions).

Coastal regions often contain sheltered nearshore wave observations. Assimilating nearshore observations in regional wave models theoretically will improve regional skill. However, nonlinear wave propagation models (e.g. SWAN, WW3) are difficult to invert. Recent developments employ variational methods, but success in complex real-world environments has yet to be observed. At swell-bands wave energy propagation across narrow shelves (e.g. U.S. West Coast) is dominated by linear processes (refraction, shoaling) and well modeled by self-adjoint ray tracing. Here, a general assimilation framework is developed to estimate physically smooth (time, direction), accurate, offshore boundary conditions from offshore and sheltered buoy observations with global model predictions included as a model prior. Case studies show error reduction at validation (non-assimilated) buoy sites suggesting that assimilation of nearshore observations improves regional skill. Initial results suggest that few (1 offshore, 1-2 nearshore) buoys are needed to sufficiently resolve offshore conditions, which has implications for cost-effective buoy array design. Additionally, buoy sites with significant misfit to assimilated observations identify regions of model error suggesting missing model physics (e.g. diffraction, reflection).

Chapter 1

Introduction

Coastally incident wave energy drives erosion of cliffs and beaches; along- and cross-shore transport of sediments, pollutants, and biota; and flooding and inundation. These processes threaten our large coastal population. Additionally, rising sea levels increase exposure to wave-driven erosion and flooding, changing storm characteristics modulate local climatology (Stocker et al., 2013); and the growing global coastal population further heightens socio-economic risk (Nicholls, 2010). Quantification of existing and future vulnerabilities necessitates long-term, accurate coastal wave predictions. This dissertation develops methods to improve coastal wave predictions by combining offshore and nearshore buoy observations and global wave model predictions in regional wave models.

Wave energy, generated by distant (Snodgrass et al., 1966) and local (Hasselmann et al., 1973) winds arrives at the coast in a range of frequencies (f), and from a variety of directions (θ). Directional wave buoys equipped with GPS or accelerometers measure vertical and horizontal motions of the sea surface, and have been deployed along our coastlines for over 30 years. Directional wave buoys yield good estimates of some wave parameters, e.g. significant wave height, period, and mean direction; however, estimates are limited to individual locations and those observations provide an incomplete description of the detailed wave energy spectrum, $E(f,\theta)$ (Ochoa and Delgado-González, 1990).

Phase-averaged wave models solve for $E(f,\theta)$ in the spectral wave action equation (Hayes, 1970) to make continuous (space and time) wave estimates. The wave action balance describes energy propagation in changing depths and currents, and parameterizes high-order effects including diffraction (Holthuijsen et al., 2003), triad (Beji and Battjes, 1993) and quartet (Hasselmann et al., 1985) interactions, dissipation, and wind-wave generation (Rascle et al., 2008). Global models, e.g. WaveWatch 3 (WW3) (Tolman, 2009), are forced by satellite observations of wind stress, e.g. QuikSCAT (Ricciardulli and Wentz, 2011), and provide coastal estimates of $E(f,\theta)$[1].

At regional scales global wave model predictions are relatively coarse ($\sim$ 4km), and though parameterizations, numerics, and global wind coverage continue to improve (Ardhuin and Roland, 2013; Cavaleri et al., 2007), predictions contain errors and bias. High-resolution ($\sim$ 500m) regional wave models, e.g. Simulating WAves Nearshore (SWAN, Booij et al., 1999), are typically used for regions of interest and require wave information at offshore boundaries. Frequently global wave model predictions are used to force the offshore boundary, (e.g. García-Medina et al., 2013); however, local buoy observations are also used (e.g. O'Reilly et al., 2016). Both approaches suffer from inherent limitations: global model inaccuracies and fundamental uncertainty in directional buoy observations (Longuet-Higgins et al., 1963; Ochoa and Delgado-González, 1990, see Section 2.3).

Previous studies suggest that the offshore boundary condition uncertainty can dominate regional prediction errors (Rogers et al., 2007; O'Reilly et al., 2016), rather

[1] Storage constraints limit the output locations of complete $E(f,\theta)$ spectra. Typically at existing buoy sites and coarsely spaced coastal locations complete spectra are saved. Only integrated wave parameters are available at grid locations.

than model numerics or physics. Compared to the U.S. East Coast where bottom dissipation can be significant and complex (Ardhuin et al., 2003), the U.S. West Coast continental shelf is deep and narrow. Additionally, a majority of wave energy arrives at low frequencies (swell-band, ≤ 0.09Hz) where nonlinear spectral transfers, white capping, and wind generation are generally minimal, e.g. the Pacific Northwest (García-Medina et al., 2013). Consequently, regional swell-band energy is well modeled by simple linear assumptions (O'Reilly and Guza, 1993; O'Reilly et al., 2016), and offshore boundary condition uncertainty dominates prediction error. Sheltered regions, such as the Southern California Bight (SBC), are particularly sensitive to offshore directional details (Fig. 1.1). The patterns of sheltering by the Channel islands and Pt. Conception change rapidly with varying offshore wave angle, and therefore first-order estimates of nearshore energy are dependent on high-order offshore directional details; details that neither buoy observations nor global wave model predictions adequately describe.

In Chapter 2 (Crosby et al., 2016), offshore buoy observations (cdip.ucsd.edu/) and global wave model predictions (WW3, Chawla et al., 2011) are compared as boundary forcings for regional wave predictions in the SCB. Model skill is evaluated at a large array of buoy observations inside the SCB and results suggests that offshore buoy observations, despite inherent directional limitations, provide more accurate boundary information than global wave model predictions. Commonly used techniques to estimate $E(f,\theta)$ from directional buoy observations[2] are compared and skill is similar. Given the different limitations in global model predictions and buoy observations, two methods to combine them are developed and tested: one analytical (Long and Hasselmann, 1979), the other ad hoc. Surprisingly, results indicate worse skill for the analytical method, and only marginal improvement for the ad hoc method, as compared to buoy-driven

[2]Complete wave energy spectra, $E(f,\theta)$, can be estimated from limited directional constraints with user-specified assumptions. Commonly used methods maximize entropy (Lygre and Krogstad, 1986) or smoothness (Herbers and Guza, 1990; Hashimoto and Kobune, 1988) of the directional spectrum.

predictions. Optimal combination of buoy observations and global model predictions is not trivial owing in part to the lack of detailed uncertainties in global model predictions. Plausible uncertainty estimates are generated in Chapter 3 for a more general inverse framework.

Offshore buoy observations provide valuable information for initializing regional wave models; however, sheltered nearshore observations could add additional regional skill. Existing assimilation techniques (Walker, 2006; Veeramony et al., 2010; Orzech et al., 2013) apply variational approaches, necessitating an adjoint to the spectral action equation. This approach is computationally costly, often used in stationary homogenous conditions, and thus far has not been applied to complex real-world settings. In Chapter 3, an alternative methodology is developed to assimilate nearshore buoy observations and offshore global model predictions. The method assumes linear wave energy propagation, valid for swell energy on the U.S. west coast (Crosby et al., 2016), and employs a general Bayesian framework that is computationally rapid and allows temporal variation. Initial testing shows consistent nearshore prediction improvement for several short-term (4-day) case studies.

Buoy observations are expensive to deploy and maintain, however, working assimilation techniques allow assessment of regional value (i.e. added skill). Initial analysis of case studies suggest that for swell energy in the SCB few buoys (1-2 offshore, 1-2 nearshore) are sufficient, and additional observations do not add appreciable skill. By varying the buoy sites assimilated, those of greatest value can be identified, aiding in optimal buoy array design. Additionally, poorly predicted regions can be identified by poor fit to the assimilated model, e.g. Santa Barbara Channel (Fig. 2.1). With boundary condition uncertainty reduced, these regions indicate missing model physics, e.g. coastal reflection, diffraction, and may be corrected by identifying the missing processes or parameterizing an empirical correction.

As global wave model predictions continue to improve the necessity of existing buoy sites will diminish. Comparisons and assimilation methods detailed here will aid in the assessment of buoy observation site value to regional prediction skill. Additionally, overall regional skill is improved and allows better estimation of nearshore processes (erosion, transport, flooding) impacting increasingly populated and vulnerable coastlines.

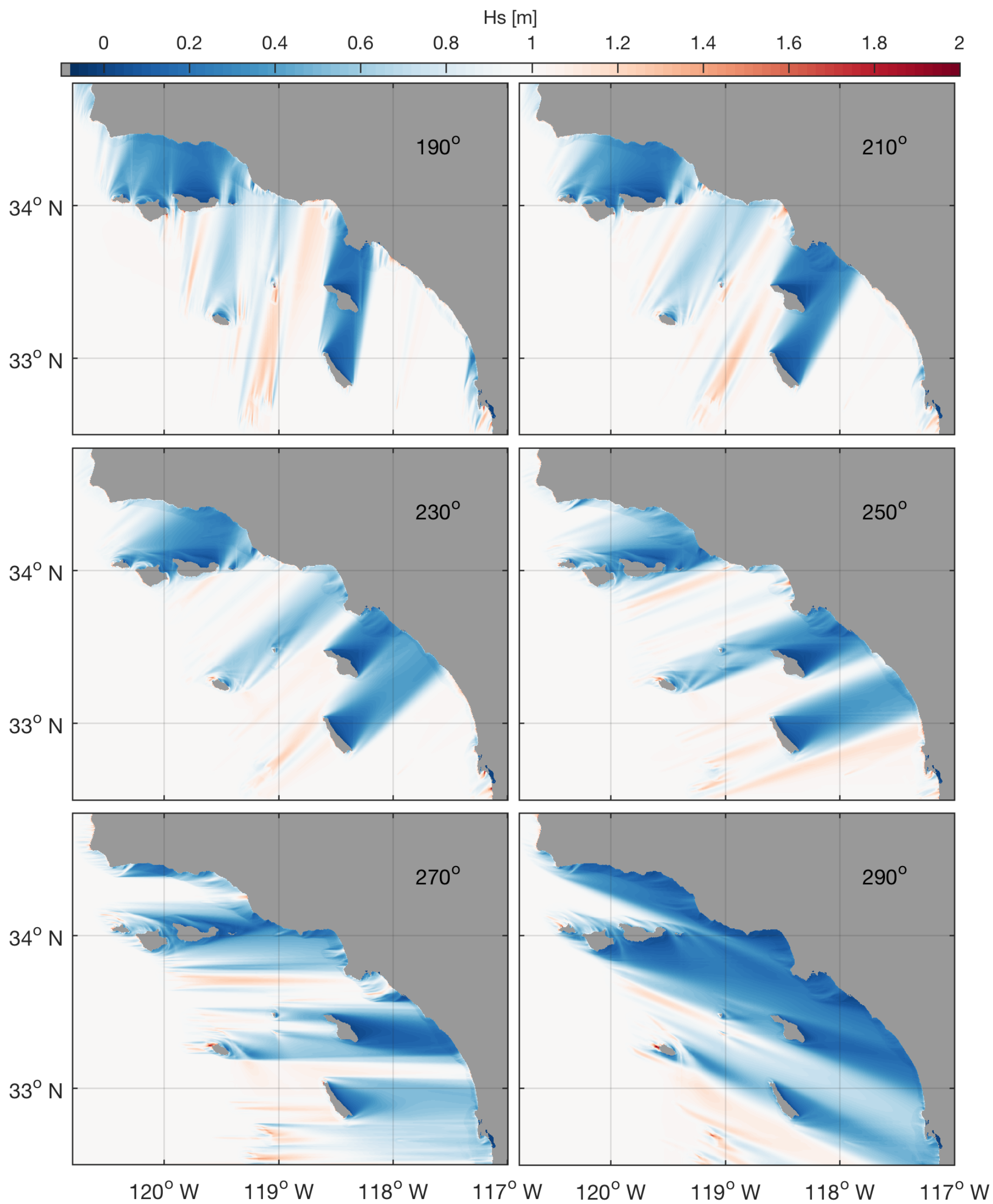

Figure 1.1: Narrow banded (0.0675-0.0725Hz) incident energy at varying directions (2-deg directional bin width) in the Southern California Bight. Offshore wave heights (white) are modulated by regional bathymetry and patterns of sheltering (blue) and focusing (red) vary rapidly in space and with incident direction (see colorbar).

Chapter 2

Boundary conditions from offshore observations and global model predictions

2.1 Abstract

Accurate, unbiased, high-resolution (in space and time) nearshore wave predictions are needed to drive models of beach erosion, coastal flooding, and alongshore transport of sediment, biota and pollutants. On sheltered shorelines, wave predictions are sensitive to the directions of onshore propagating waves, and nearshore model prediction error is often dominated by directional uncertainty offshore. Here, regional wave model skill in highly sheltered southern California is compared for different offshore boundary conditions created from offshore buoy observations and global wave model hindcasts (NOAA WW3). Spectral ray-tracing methods are used to transform incident offshore swell (0.04-0.09Hz) energy at high directional resolution (1^o). Model skill is assessed for predictions (wave height, direction, directional spread, and alongshore radiation stress) at

16 nearshore buoy sites between 2000 and 2009. Buoy-derived boundary conditions using various estimators (maximum entropy, maximum smoothness) have similar skill and all out-perform WW3-derived boundary conditions. A new method to estimate offshore boundary conditions, CMB-ADJ, combines buoy observations with WW3 predictions. Although CMB-ADJ skill is comparable to buoy-only methods, it may be more robust in varying regions and wave climatologies, and will benefit from future improvements in GWM predictions. A case study at Oceanside harbor shows strong sensitivity of alongshore sediment transport estimates to boundary condition method. However, patterns in alongshore gradients of transport (e.g. the location of model accretion and erosion zones) are similar across methods. Weak, tidally-modulated, coastal reflection is evident in both shallow and deep buoy observations, and significantly increases the observed directional spread.

2.2 Introduction

Nearshore waves impact port and waterway operations, beach recreation, boating safety, and contribute to coastal inundation. Over decades, nearshore wave energy shapes the coastline by eroding beaches and transporting sediment alongcoast. Accurate, high-resolution wave predictions are needed in hindcast, real-time, and forecast modes. Operational global wave models (GWMs) have good skill due to recent improvements of model parameterizations (Ardhuin et al., 2010), development of obstruction grids (Chawla and Tolman, 2008), faster computers, and increasing satellite global wind coverage. However, GWM spatial resolution is typically too coarse to properly resolve local islands, shoals, and rough coastline features, e.g. Southern California (SC) shown in Fig. 2.1.

Higher resolution nearshore wave predictions are obtained by dynamical downscaling, i.e. the use of regional nonlinear 3rd generation wave models, e.g. (García-Medina et al., 2013). Though large regions and long time series can require significant computational resources, statistical and/or hybrid downscaling methods can reduce computational expense (Camus et al., 2011, 2013). Hybrid methods model a small set of representative wave conditions, forming a lookup table that is used to create continuous predictions. When the local wave climatology is relatively simple, e.g. limited exposure to large ocean basis, hybrid methods work well. However, in regions with wide exposure and many energy sources, the model lookup table required to adequately represent possible conditions may become unmanageably large.

In some regions for some frequencies, e.g. swell energy on the U.S. West Coast, refraction and shoaling dominate the wave field, and nonlinear interactions and energy sources/sinks can be ignored (O'Reilly and Guza, 1993; O'Reilly et al., 2016). High spatial, directional and temporal resolution at small computational costs can be achieved by using ray-tracing methods to linearly propagate offshore energy inshore (Dorrestein, 1960; Longuet-Higgins, 1957). Here, we use these linear energy propagation techniques for swell band waves (0.04-0.09Hz) in SC, modeling $\sim$60% of the total shoreward wave energy flux (Fig. 2.2). Swell model prediction skill at nearshore buoy sites is compared for different offshore boundary condition parameterizations.

In many populated regions both offshore GWM predictions and buoy observations are available to parameterize a regional wave model boundary. These two data sources are generally independent since operational GWMs do not yet assimilate local buoy observations, though data assimilation is an active area of research (Orzech et al., 2013; Panteleev et al., 2015). When local wave observations are sporadically available (typically in the case of satellite altimetry or short-term buoy observations) biases can be removed from continuous GWM predictions (Mínguez et al., 2011), and the calibrated predictions are then used for the model boundary condition. However, when long-term offshore wave buoy records are available, it is not clear how to best specify the model boundary condition. GWM predictions have skill, but still suffer from errors and biases. Additionally, GWM predictions are not typically available in complete frequency-directional detail at all model grid points. In contrast, buoy observations provide an accurate energy distribution in frequency, but have significant directional ambiguity (Ochoa and Delgado-González, 1990). Rogers et al. (2007) created an operational wave model for southern California (SC) using offshore buoy observations for some model boundaries and GWM predictions for others. In their discussion they experimented with a combination of offshore GWM directional predictions and non-directional (e.g. energy only) buoy observations, but found that the combination could increase nearshore prediction errors during bimodal (northern and southern) conditions, common in SC. Here, we extend the preliminary discussion in Rogers et al. (2007), and consider in detail the skill of using GWM and buoy observations in the boundary condition for our SC swell wave model. We examine the predictive skill for significant wave height, wave direction, and alongshore radiation stress with different boundary forcings. We find that buoy observations provide more accurate boundary condition information than GWM predictions and that surprisingly, combinations of GWM and buoy observations are no more skillful than buoy observations alone. While our study is limited to remotely generated swell wave energy, future work will consider the more difficult question of using of GWM and buoy observations for the boundary condition at higher frequency wave energy, where local wind generation may be important.

Section 2.3 discusses the limitations of directional wave buoy observations and various methods typically used to construct directional spectra. Additionally, formulations for alongshore radiation stress and alongshore transport are reviewed. Section 2.4 describes the study region, buoy observations, wave model methodology, and boundary condition methods tested. Section 2.5 compares the skill of different boundary conditions.

Section 2.6 discusses regional model error, examines the effect of small directional biases in the context of alongshore transport, and considers the effect of weak coastal reflection.

2.3 Background

Phase-averaged offshore wave energy, $F(f,\theta)$, is decomposed into the total energy, $E(f)$, at each frequency band, f, and a normalized directional distribution, $D(f,\theta)$, such that

$$F(f,\theta) = E(f)D(f,\theta) \tag{2.1}$$

Using accelerometers or onboard GPS, directional wave buoys measure vertical and horizontal surface translations. Once transformed into frequency space, combinations of co- and quad-spectra provide estimates of $E(f)$ and four integral constraints on $D(f,\theta)$ (Longuet-Higgins et al., 1963; Long, 1980). Dropping f for clarity, the directional constraints in matrix notation are

$$\mathbf{d} = \begin{bmatrix} a_1 \\ b_1 \\ a_2 \\ b_2 \end{bmatrix} = \begin{bmatrix} \int D(\theta)\cos\theta\, d\theta \\ \int D(\theta)\sin\theta\, d\theta \\ \int D(\theta)\cos 2\theta\, d\theta \\ \int D(\theta)\sin 2\theta\, d\theta \end{bmatrix} . \tag{2.2}$$

Additionally normalization yields,

$$\int D(\theta)\, d\theta = 1\,, \tag{2.3}$$

and the energy cannot be negative,

$$D(\theta) \geq 0\,. \tag{2.4}$$

The directional constraints on $D(\theta)$ in (2.2), often referred to as low order moments, can be used to estimate the bulk directional properties: mean direction (θ), spread (σ), skewness, and kurtosis. Additionally, first (a_1, b_1) and second (a_2, b_2) low order moments can be used independently to estimate θ and σ such that

$$\begin{aligned}
\theta_1 &= \arctan(b_1/a_1) \\
\theta_2 &= 2\arctan(b_2/a_2) \\
\sigma_1 &= \sqrt{2(1-\left(a_1^2+b_1^2\right)^{1/2})} \\
\sigma_2 &= \sqrt{\tfrac{1}{2}(1-\left(a_2^2+b_2^2\right)^{1/2})}
\end{aligned} \tag{2.5}$$

(Kuik et al., 1988; Herbers et al., 1999, 2012). The 180° ambiguity in θ_2 does not differentiate between normally incident waves and their specular reflection. The corresponding σ_2 estimate is advantageous when the properties of incoming waves only are sought, whereas σ_1 is a sensitive reflection detector (Herbers et al., 1999). Statistics of directional moments and bulk properties for a finite length buoy record are in Long (1980) and Kuik et al. (1988).

Low order moments are accurately measured by a Datawell directional wave buoy (O'Reilly et al., 1996), but they do not define a unique directional spectrum (Ochoa and Delgado-González, 1990), and a continuous or finely discretized $D(\theta)$ is needed at wave model boundaries. Estimating $D(\theta)$ from limited information in (2.2,2.3,2.4) is a classic geophysical inverse problem (Backus and Gilbert, 1967) requiring an additional subjective constraint. Minimum roughness ($d^2D/d\theta^2$) yields the simplest solution consistent with the data and is often used (Constable et al., 1987). In the last four decades various constraints have been used to find $D(\theta)$ given observed buoy moments and constraints (2.3,2.4), including maximum entropy (Kobune and Hashimoto, 1986; Lygre and Krogstad, 1986), minimum roughness (Herbers and Guza, 1990), and others

(Oltman-Shay and Guza, 1984; Hashimoto and Kobune, 1988). These methods optimize different flavors of smoothness, and the ability of each constraint to accurately represent the true directional spectrum likely varies regionally and seasonally. All smoothness constraints necessarily fail when the true $D(\theta)$ is complex owing to multiple directional sources. As an alternative to smoothness, Long and Hasselmann (1979) presented a method to find the $D(\theta)$ that is consistent, in a least-squares sense, with both measured buoy moments and an a priori preferred spectrum (e.g. generated by a GWM).

The uncertainty inherent in buoy observations is illustrated in Fig. 2.3a; the same buoy observations (2.2), typical of bimodal directional spectra in SC, are input to the Maximum Entropy Method (MEM, Lygre and Krogstad, 1986), minimum roughness method (MRM, Herbers and Guza, 1990), and the Bayesian Direct Method[1] (BDM, Hashimoto and Kobune, 1988). Although the direction of the primary NW peak is fairly consistent, the estimators disagree on amplitudes and widths of the two peaks even though each of these distributions are consistent with the same deterministic low order moments. Furthermore, each of these estimates vary considerably owing to statistical fluctuations of $\mathbf{d}$ in (2.2). For a typical 1-hour buoy record, known uncertainty in the low order moments (Long, 1980) is used to generate many (N=10,000) random realizations of $\mathbf{d}$. MEM and MRM methods are then used to create many realizations of $D(\theta)$ from which a probability distributions is created illustrating the statistical uncertainty (Fig. 2.3b,d). Fig. 2.3c shows a similarly derived distribution for a method combing buoy observations and GWM predictions introduced in Section 2.4.4. Three hour averaging of buoy observations is used in our analysis to reduce the statistical blurring of $D(\theta)$.

Intuition about the fundamental limitations of buoy observations follows from considering the number of system knowns and unknowns. Buoy observations provide five knowns (2.2,2.3). A uni-modal system can be described by a mean direction, amplitude,

[1] The method is often unstable for point-source wave observations, e.g. buoy or PUV; however, we ignore the AIC criterion and seek a stable spectra with closest fit to the observed low order moments.

directional spread, skewness, and kurtosis (five unknowns). A bi-modal system can be described with two peak amplitudes, two peak directions, with one known left to describe (poorly) both peak widths. Properties of two individual peaks are blurry, and with more than two peaks, buoy moments cannot even describe peak locations and amplitudes.

Despite these inherent limitations, directional buoys measure the alongshore radiation stress, S_{xy}, exactly, without the need to estimate $D(f,\theta)$ (Longuet-Higgins and Stewart, 1964). S_{xy} is directly proportional to the low order moment $b_2^{(r)}$ where,

$$\begin{aligned} S_{xy} &= \int\int \left[\frac{c_g}{c}\right] E(f)D(f,\theta)\sin\theta\cos\theta\, d\theta\, df \\ &= \frac{1}{2}\int \left[\frac{c_g}{c}\right] E(f) b_2^{(r)}(f)\, df \end{aligned} \tag{2.6}$$

and $b_2^{(r)}$ is the buoy moment rotated into the local shore-normal reference frame. S_{xy} is an important driver of alongshore currents (Guza et al., 1986) and transport (Komar and Inman, 1970). In the frequently used CERC transport formula (Komar and Inman, 1970) the immersed weight of sediment, I, is

$$\begin{aligned} I &= KEc_g \frac{\sin 2\theta}{2}\bigg|_{breaking} \\ &= KS_{xy}c_p\Big|_{breaking} \end{aligned} \tag{2.7}$$

where c_g is group velocity, c_p is phase velocity, and K is an empirical constant typically $0.4-0.8$. The simplistic CERC formula performs similarly to sophisticated process models (Haas and Hanes, 2004).

2.4 Methods

2.4.1 Study Region

Southern California (SC) extends from Pt. Conception to the US/Mexico border (Fig. 2.1), and is exposed to distant north and south Pacific storms as well as local wind-swell (Adams et al., 2008). Complex coastal bathymetry and shadowing from offshore islands create a spatially variable nearshore wave field that is extremely sensitive to the offshore wave direction. Directional inaccuracies of the waves specified at the offshore boundary are believed to be the dominant source of wave model prediction error in southern California (O'Reilly and Guza, 1993; Rogers et al., 2007).

2.4.2 Swell Wave Model

Modern 3rd generation wave models [e.g. WaveWatch III (WW3) and Simulating WAves Nearshore (SWAN)] solve the spectral wave-action equation (Hayes, 1970) which includes refraction, shoaling, wind generation, nonlinear wave interactions, wave-current interactions, white capping, bottom dissipation, and depth-limited breaking. These commonly used, state-of-the-art models are computationally expensive with high spatial resolution and long duration. In SC, the transformation of low frequency (0.04-0.09Hz) swell is dominated by island sheltering, and bathymetry-controlled shoaling and refraction (O'Reilly and Guza, 1993; O'Reilly et al., 2016). Our SC swell wave model, limited to 0.04-0.09Hz frequencies, captures these effects using frequency-direction dependent transfer coefficients derived from backwards ray-tracing methods, see Section 2.B, Longuet-Higgins (1957), Dorrestein (1960), and Mehaute and Wang (1982). The transfer coefficients represent a linear relation between the offshore and nearshore wave field. Because energy travel time across SC can be significant, 10+ hours, frequency-direction dependent time lags are included by assuming energy propagation at the theoretical group velocity (Fig. A.1), following O'Reilly and Guza (1998) and O'Reilly et al. (2016). This methodology significantly reduces computation expense, but requires the assumption that offshore wave conditions are spatially homogenous (with time lags) in the along-crest direction (Fig. A.1). This contrasts with typical modern wave models that accept heterogeneous boundary conditions offshore. However, offshore GWM predictions confirm along-crest spatial homogeneity over the few 100km scales of SC for the remotely generated waves that dominate the swell-band (<0.09Hz), details in Appendix A. Our swell model predictions are therefore a linear function of offshore energy, $E(f,\theta)$, with an appropriate time lag, $\tau(f,\theta)$.

The swell model captures approximately 60% of offshore energy flux (Fig. 2.2b). Model transfer coefficients are created at a 0.005 Hz frequency resolution, typical of buoy hourly records, and 1^{o} directional resolution that is higher than commonly used, but desired for directionally sensitive SC. The linear framework allowed for relatively rapid testing of different boundary conditions from 2000-2009. All wave properties discussed in the following are swell-band averaged such that some property $\bar{x}$ is

$$\bar{x} = \frac{\int_{0.04}^{.09} E(f)x(f)\,df}{\int_{0.04}^{.09} E(f)\,df}.$$

2.4.3 Buoy observations

Quality controlled, hourly, Datawell directional buoy observations (energy and low order directional moments) from the Coastal Data Information Program (CDIP, http://cdip.ucsd.edu/) were smoothed with a 3-hour running mean. The reduction of statistical uncertainty with three-hour smoothing is particularly important for low-frequency narrow-banded swell where the effective degrees of freedom (EDOF) are low (Elgar, 1987). In extreme cases (e.g. 20 second SW swell) the EDOF of a 1-hour buoy record can be less than 100 for the entire swell band spectrum, corresponding to approximately a $\pm 25\%$ uncertainty (90^{th} percentile) in measured energy. Swell conditions are often stationary for three hours, and minimal temporal resolution is lost. The regional wave model is initialized with the exposed, offshore buoy, 071, in 550m water depth. The model is tested with nine coastal deep water buoys in depths ranging from 180-500m, and eight local shallow water buoys in 20m depth (Table 2.1, Fig. 2.1). Buoy site occupation duration varied (Table 1). Shallow buoys were typically deployed for the shortest times, approximately one year.

2.4.4 Boundary Conditions

Estimates of $F(f,\theta,t)$ offshore were specified from buoy 071 observations and from GWM predictions. Buoy 071 has wide directional exposure and a 10-year time series of energy, $E_b(f)$, and directional moments, $\mathbf{d_b}(f)$. For hindcast GWM predictions we use the National Oceanic and Atmospheric Administration (NOAA) WW3 reanalysis (Tolman, 2009; Chawla et al., 2011, 2013). The U.S. West Coast reanalysis has $4-$arcminute (7km) spatial resolution, 3-hour temporal resolution, 10-degree directional resolution, and logarithmic frequency spacing. Complete GWM energy-directional spectra predictions, $F_{WW3}(f,\theta,t)$, and collocated buoy 071 observations from 2000-2009 are used to specify boundary conditions. $F_{WW3}(f,\theta,t)$ is re-banded in frequency to match typical buoy spectral output (0.005Hz bandwidth from 0.04-0.09Hz) and interpolated by nearest-neighbor to 1-hour temporal and 1^{o} directional resolution. Excluded are the less than 6 months total when buoy 071 observations were unavailable. Boundary conditions tested are divided into three categories:

- GWM-only: $F_{WW3}(f,\theta)$ is used exclusively, hereafter **WW3**.
- Buoy-only: $F(f,\theta)$ is created with buoy 071 observations. Three different methods,

MEM, **MRM**, and **BDM** (See Section 2.3), are tested to estimate the discrete directional spectrum from directional buoy observations, (2.2).

- Combined (**CMB**): Buoy 071 observations are combined with GWM predictions of the normalized directional distribution, $D_{ww3}(f,\theta)$, in three different ways.

The first CMB method, hereafter **CMB-E**, multiplies the buoy E_b by D_{ww3}, after the discussion of Rogers et al. (2007). Buoy directional information is not used. The second CMB method, hereafter **CMB-LH**, combines D_{ww3} with both E_b and $\mathbf{d_b}$ (Long and Hasselmann, 1979). The optimal directional spectrum, D_{LH}, minimizes

$$\int (D_{LH} - D_{ww3})^2 \, d\theta \,, \tag{2.8}$$

while satisfying $\mathbf{d_b}$ (2.2) and constraints (2.3) and (2.4). The computationally efficient iterative method developed by Long and Hasselmann (1979) terminates when constraints are met within the expected statistical uncertainty (Lawson and Long, 1983; Long, 1980). We tested this iterative method and found that fitting constraints exactly yielded unbiased spectra with comparatively better nearshore predictive skill. Additionally, we compared the iterative method solutions to those from a modern optimization numerical solver, CVX, a package for specifying and solving convex problems (Boyd and Vandenberghe, 2004; Grant and Boyd, 2013). Both solutions were robust for most conditions, however the iterative method occasionally failed to converge for very low energy spectra. We ultimately used CVX to solve the minimization, however, we continue to refer to the solution as CMB-LH. Once found, D_{LH} is multiplied by E_b to construct $F(f,\theta)$, as in the CMB-E method.

The third CMB method, hereafter labeled **CMB-ADJ**, is not formally optimal, but relies instead on physically meaningful adjustments to D_{ww3} including a series of shifts and smoothings to minimize misfit to constraints (2.2) with $\mathbf{d_b}$. Initial testing showed the ideal simultaneous optimization was computationally burdensome and provided marginal improvement over the simpler sequential adjustment process used below at each frequency bin for each hour-record,

1. Time lag/leads in $F_{WW3}(f,\theta)$ are corrected for each 1-hour time-step by considering the optimal time lag correlation between GWM predicted energy, $\int F_{WW3}(f,\theta)\, d\theta$, and E_b inside a $\pm$36-hour window. Typically time lag/lead corrections were small ($<$3-hours) and consistent across wave events.

2. Significant peaks in D_{ww3} are found (using MATLAB's Signal Processing toolbox) that meet the following criteria:

   (a) Each peak contains at least 2% of primary peak energy

   (b) Peaks spaced less than 55^{o} are considered a single peak.

3. If D_{ww3} is uni-modal (49% of records)

   (a) Rotate D_{ww3} to match θ_1 measured by buoy 071.

   (b) Estimate σ_2 for D_{WW3} from (2.2) and (2.5). Smooth D_{ww3} by convolving with a simple boxcar repeatedly until σ_2 for D_{WW3} approximately equal to σ_2 measured by buoy 071. Here σ_2 is used to sometimes avoid over-smoothing due to buoy-observed coastal reflection.

4. If D_{ww3} is bi-modal (49% of records)

   (a) Use brute force to find the shift of energy between the two peaks in D_{WW3} such that the misfit to $\mathbf{d_b}$ by (2.2), weighted by the uncertainty in $\mathbf{d_b}$ (Long, 1980), is minimized.

   (b) Simultaneously and independently shift both peak directions (with a maximum shift of 25^{o}) to minimize misfit to $\mathbf{d_b}$.

5. If D_{ww3} contains three or more peaks (2% of records), make no directional adjustments to WW3 spectrum as buoy directional information is too limited.

Lastly, as in the previous methods, the adjusted D_{WW3} is multiplied by E_b to form $F(f,\theta)$. These adjustments to D_{WW3} include some threshold values that may be region specific. Additionally, the performance of the methods is dependent on the accuracy of the GWM; statistical chatter in buoy observations can only degrade the predictions of a theoretically error-free GWM. However, here we show that buoy-based adjustments with these thresholds do detectably improve the GWM-only, WW3, boundary condition method skill.

2.5 Results

2.5.1 Significant wave height, direction, and spread

Model predictions (using boundary conditions described above) are compared with observations at sheltered deep buoys using standard metrics (root mean square error RMSE, bias, model skill R^2, and squared-correlation r^2, see Section 2.C for definitions). Model skill varies across boundary condition, buoy validation site, and metric. Simple averages at deep buoy validation sites (Table 2.2) are used to rank boundary condition skill in Table 2.3, where lowest score is best. Bias magnitude was averaged for H_{sig} and θ_1 to avoid canceling errors. CMB-ADJ and MEM have the highest θ_1 skill, while MRM and BDM have the highest H_{sig} skill. WW3 has overall lowest skill followed by CMB-E. CMB-ADJ has the highest overall skill followed by BDM. Models using buoy observations in the boundary condition (buoy-only and CMB) outperform WW3 alone. However, directional bias is lowest for WW3 and CMB boundary conditions at local deep buoys. Bias in σ_1 predictions is negative for all boundary conditions, and largest at low frequencies (not shown), suggesting weak coastal reflection (Section 2.6.3). Comprehensive skill results for significant wave height, H_{sig}, mean direction, θ_1, and directional spread, σ_1, for all boundary conditions at all buoy validation sites are in Tables 2.5,2.6.

The spatial distribution of model skill for a subset of boundary conditions shows that WW3 initialization consistently has relatively large RMSE and bias; in Fig. 2.4 the upper left quadrant is large and dark at most buoys, for both H_{sig} and θ_1. H_{sig} from WW3 is biased high at the initialization offshore buoy 071 (+23cm), and WW3 is correspondingly high in the southern half of the model domain. In contrast, WW3 initializations are biased low for H_{sig} in the Santa Barbara Channel (SBC), closest to the initialization buoy (Fig. 2.4a) and directional errors and biases are also large. Boundary condition MRM shows particularly large positive (northward) directional bias in the southern end of the SBC. A ranking of buoy site skill, averaged across select boundary conditions (Table 2.4), indicates poorest model performance at buoy sites 107 (in SBC) and the southern most, 093.

2.5.2 Alongshore radiation stress

Mean (time-averaged) S_{xy} model predictions and shallow (20m depth) buoy observations are compared in the local shore normal reference frame estimated from depth contours onshore of each buoy; positive S_{xy} indicates northward up-coast transport (Fig. 2.5). Modeled and observed S_{xy} usually agree, at least qualitatively. Boundary conditions using offshore buoy observations generally outperform WW3 alone. No buoy-based method clearly performs best. Uncertainty bars on S_{xy} correspond to $\pm 2.5^{\circ}$ shifts of the local shore normal. At buoy 155, mean S_{xy} is near-zero, and the results are relatively sensitive to the definition of beach normal. At buoy 043 (Oceanside Harbor), different offshore boundary conditions yield the widest range of S_{xy} with WW3 biased high and MRM biased low.

Depth contours offshore of Oceanside Harbor (grey, Fig. 2.6a) were used to estimate local shore-normals (dark magenta, Fig. 2.6a) that were alongshore averaged (excluding the harbor area) to avoid the influence of slight shore normal changes on S_{xy}. Predicted H_{sig}, θ_2, and S_{xy} on the 10m-depth contour (bright green) show similar alongshore variation about constant offsets (Fig. 2.6b,c,d). WW3 predicts the highest wave heights, and the most oblique waves, resulting in the highest S_{xy}. These are compared to buoy 043 observations of S_{xy} (Fig. 2.6d, S_{xy} conserved assuming depth contours are parallel). Alongshore sediment transport estimated using the CERC formula[2], (2.7), with constant $K = 0.6$ (Fig. 2.6e) yields estimates between $2-9x10^5$ m^3/yr. Shaded regions show transport estimates for a typical range of CERC constant K ($0.4 < K < 0.8$), smoothed by 1.5km alongshore LOWESS filter. Longshore transport gradients, estimated from smoothed transport estimates, are similar for all predictions (Fig. 2.6f). Note this gradient estimate ignores the effect of the harbor and small scale ($<$ 1.5km) alongshore variations in S_{xy}.

2.6 Discussion

2.6.1 Optimal boundary condition

Offshore buoy observations improve WW3 nearshore wave prediction skill for most metrics at most buoy validation sites. However, improvement is lowest for CMB-E, where the buoy-measured energy is combined with D_{ww3}. Model skill further increases when buoy energy and directional information is used, and CMB-ADJ outperforms CMB-LH (Table 2.3). Detailed examination of CMB-LH reveals that the least-squares constraint in (8) often adds spurious directional peaks to the directional distribution. For example

[2]Waves were linearly shoaled to breaking (Ec_g = constant) with breaking constant, $\gamma = 0.7$

in Fig. 2.3a, CMB-LH creates a third peak at 100^o and adds energy in the gap between the peaks. In contrast, CMB-ADJ more physically adjusts peak amplitude, direction and width. While mathematically convenient and theoretically elegant, the CMB-LH squared difference constraint is not effective. CMB-ADJ, though crude, outperforms CMB-LH.

While buoy observations improved the WW3 boundary condition, the skill of CMB-ADJ is similar to buoy-only methods; CMB-ADJ H_{sig} skill is lower, but direction skill is higher, yielding an overall higher skill ranking (Table 2.3). Given the directional ambiguity in buoy observations (e.g. Fig. 2.3), we expected that offshore GWM directional spectra predictions offshore, informed by global wind fields and sophisticated model physics, would provide a powerful additional constraint. However, we were surprised to find that our combinations of offshore GWM spectra and buoy observations in the offshore boundary condition parameterization were similarly skilled to buoy-only methods. We show below that CMB-ADJ and buoy-only methods have similar skill because details in GWM directional spectra are often well-represented by the first four low order moments, (2.2), non-negativity, and a smoothness constraint. In other words, the present GWM directional resolution is roughly comparable to a directional wave buoy.

GWM (NOAA-WW3 hindcast) frequency-directional spectra for 1-year were used to estimate the first four low order directional moments (Eq 2) in each frequency-time bin. Using MRM, MEM, and BDM methods (Section 2.3), reconstructions of the GWM directional spectra were generated, and R^2 misfit of the reconstructed spectra to the original GWM spectra were computed. An example uni-modal reconstruction by MRM and BDM is very good ($R^2 \geq 0.9$); however, performance declines as spectra complexity increases in bi-modal and tri-modal cases (Fig. 2.7, left panels). Mean R^2 misfit values of MRM reconstructions for the entire year of GWM predictions show that high-energy events tend to have high $R^2 > 0.9$ across all frequencies (red in Fig.

2.8). Reconstructions of lower energy directional spectra have lower skill, suggesting that spectra are more complex (green/blue in Fig. 2.8). The presented skills, with the exception of normalized skill in Fig. 2.4a, are more strongly influence by moderate to high energy events that are well-represented by buoy directional moments. During these events GWM directional spectra provides little additional information, and therefore combined (CMB-ADJ) and buoy-only methods have similar nearshore predictive skill.

Overall skill for buoy-only methods is comparable, however we observed differences across metrics. MRM has lower H_{sig} RMSE, MEM has lower directional bias, and BDM is a compromise of the two. No buoy-only method is the overall best performer, and likely the ability of each method to recreate the true directional spectra depends on frequency band, wave age, and region. GWM directional spectra predictions, used as a proxy for true spectra, yield insight into method differences and the importance of diffuse reflections and scattering (Fig. 2.7). Reconstructions of GWM directional spectra from the first four low order moments using each buoy-only method (left panels) are contrasted with the addition of a small (10% of the total energy) isotropic background energy added to the GWM spectra (right panels). A constant background energy (Snodgrass et al., 1966) crudely mimics diffuse shoreline reflections and scattering. (Elgar et al., 1994) observed low levels of reflection from a natural beach, and (Ardhuin and Roland, 2012) found that constant reflection on order 10% improved GWM prediction along the coast (GWM predictions used here do not include reflection). The addition of background energy reduces MRM and BDM reconstruction skill, but improves dramatically MEM reconstruction skill. MEM is designed to identify peak directions in the presence of background energy, its roots in astronomy and image processing (Gull and Skilling, 1984); however, peaks are too sharp when background energy is lacking. In contrast, MRM and BDM are both smoother than MEM, and background energy tends to overbroaden peaks. Additionally, in the bimodal case (Fig. 2.7d), MRM and BDM peaks are slightly biased away from the overall mean. MEM better resolves incoming directional peaks in the presence of background energy, but BDM and MRM better resolve broader directional peaks with low background energy; no method is optimal. Buoy observations are fundamentally limited: these three methods are drawn from an infinite set (Ochoa and Delgado-González, 1990), and each will perform only as well as their smoothness constraint represents the true underlying directional spectra.

2.6.2 Alongshore radiation stress & transport

For most boundary condition methods, at most buoys, θ_1 bias is $< 10^{o}$, relatively small for most practical applications. However, at some buoy sites S_{xy} estimates varied significantly (Fig. 2.5); at buoy sites 043 and 172 S_{xy} estimates varied by more than a factor of two, substantial given that S_{xy} is directly proportional to alongshore transport estimates based on the CERC-formula. This variation in S_{xy} from different boundary conditions exceeds the uncertainty in the CERC constant K (Fig. 2.6f). Though boundary conditions utilizing offshore buoys yield better estimates of S_{xy} than WW3, there is no overall best performer. The positive mean S_{xy} at buoy 043, indicating northward transport, is contrary to expectations for the region (Inman and Frautschy, 1965), however this estimate is integrated only for swell energy (0.04-0.09Hz). Mean S_{xy} for the entire wave energy spectrum is typically negative (O'Reilly et al., 2016), indicating southward transport in the region.

Alongshore transport estimates from different boundary conditions differ primarily by a constant offset (Fig. 2.6e). Thus, the alongshore transport gradient, i.e. divergence of the drift indicating regions of accretion and erosion, is relatively consistent (Fig. 2.6f). Typically the gradients of uncertain quantities are increasingly uncertain, however in this case the bias between predictions in terms contributing to S_{xy}, H_{sig} and θ_2, is constant alongshore (Fig. 2.6b,c). Therefore, accretion and erosion zones (Eq 4) may be determined confidently. We suspect that at these spatial scales (Order 1 km) gradients in alongshore transport gradients are dominated by local bathymetry and high-order details of the offshore directional spectrum are insignificant. Note a single offshore normal is used to estimate S_{xy}, and small-scale variations in beach orientation are not included.

2.6.3 Coastal reflection

Weak coastal reflection ($< 10\%$) has small effects on H_{sig} and mean direction; even obliquely incident wave conditions yield little change to θ_1 and θ_2 observations, less than 4^{o} and 2^{o} respectively. Alternatively, first order directional spread (σ_1) observations are highly sensitive to coastal reflection. Including simple reflection parameterizations in GWMs significantly improves predicted σ_1 skill (Ardhuin and Roland, 2012). While not included in our linear wave model, strong negative biases in σ_1 predictions across all model boundary conditions are consistent with weak coastal reflection (Table 2.2). Strong ($> 10^{\mathrm{o}}$) tidal modulation of σ_1 is observed at local shallow buoy 172 offshore of Huntington Beach during a low-frequency event arriving from a high incident angle, 20-30^{o} southward of the local shore normal (Fig. 2.9b). At high tide, this convex beach has relatively high slope, and enhanced reflection, similar to Duck, NC (Elgar et al., 1994). A buoy also feels the effect of directional narrowing due to increased refraction as the tide falls; however, these effects (estimated assuming plane parallel contours, (Herbers et al., 1999)) are small in 20m depth for the local tidal amplitude ($< 2^{\mathrm{o}}$, black line in Fig. 2.9b), and vanishingly small in more than roughly 100m depth. The observed modulation in σ_1 at buoy 172 corresponds roughly to a 3-10% change in reflected energy, equivalent to a 2-5% change in H_{sig}; similar levels of reflection are observed in (Elgar et al., 1994). Owing to the high incident swell angle, tidal modulation of σ_2 is also observed, though at less than half the variance observed in σ_1. Coherence at tidal frequencies M2 and K2 between the local tidal elevation and observed $\sigma_1(f)$ (estimated independently at each observed frequency) is high in the swell-band (0.04-0.09Hz), peaking around 0.06Hz and falling off at higher frequencies where reflection is weaker (Fig. 2.9c). As expected for a nearby reflector, at local shallow buoys close to shore the phase lag for K1 and M2 frequencies is near zero ($< \pm 0.1$hr). At local deep buoys phase lags at K1 and M2 are scattered between ± 0.5hr (not shown).

Steep coastline slopes reflect more incoming wave energy. The SC coastline is a mix of dissipative (fine to coarse sand), intermediate (gravel), and reflective (riprap, seawall, rocky cliffs) regions shown in Fig. 2.10 (NOAA, 2006). The magnitude of σ_1 prediction bias (left half of colored square) at local buoy sites appears lower in regions with larger amounts of dissipative coastline, e.g. San Diego (Fig. 2.10). Conversely prediction bias is larger where coastlines are steeper, e.g. Santa Barbara and Los Angeles. This evidence is admittedly qualitative, and some observations suggest the opposite, e.g. buoy 092. Coherence of tidal elevation and σ_1 (colored right rectangle) is higher at shallow buoy sites and is significant at all buoys except 093 (Fig. 2.10). Coherence is lower further from the coastline because the travel times of reflected waves varies. At even larger distances (not shown), buoys are exposed to a large array of diffuse reflectors (coastline and islands), and tidal effects are blurred in direction and time (Snodgrass et al., 1966; Herbers et al., 1999).

2.6.4 Santa Barbara Channel (SBC)

Our results confirm the previously observed large H_{sig} prediction errors in the SBC (Rogers et al., 2007; O'Reilly et al., 2016). The extreme sheltering by Pt. Conception and the Channel Islands (Fig. 2.1) amplify the significance of high-order details of the offshore directional wave spectra. For example, during NW wave events the SBC is often sheltered to the dominant swell direction by Pt. Conception, making critical the accurate description of the peak shoulder (e.g. Fig. 2.C.1). A higher resolution boundary condition than provided by WW3 predictions and buoy observations may be needed. Missing model physics likely partially explain these prediction errors; reflection from the steep cliff faces of the Channel Islands could help explain the H_{sig} low bias. Also supporting reflection, the positive (northward) directional bias at buoy 107 suggests additional wave energy coming from a more southerly direction. However, further eastward in the SBC (buoys 111, 130, 131) model directional bias suggest the opposite. It is not clear if wave reflection contributes significantly to the large model errors in in the SBC. Diffraction, surface current-induced refraction, and bathymetry inaccuracies may also contribute to prediction errors.

2.7 Summary

Different methods for parameterizing regional wave model offshore boundary conditions from buoy observations and global wave model GWM predictions (NOAA-WW3) are compared. Offshore wave energy was transformed to the nearshore with ray-tracing derived transfer coefficients and frequency-direction dependent time lags (Section 2.4.2 and Section 2.B). Offshore wave conditions were assumed homogenous in the along-crest direction for each discrete frequency and direction, a valid assumption for swell-band (0.04-0.09Hz) energy in SC (Appendix A). Limiting model predictions to the swell-band allowed for the use of point-based offshore information in the boundary condition, i.e. buoy observations and frequency-direction GWM predictions. This methodology is valid for only swell energy in hindcast and nowcast modes.

Results show that for swell predictions, boundary conditions including offshore buoys performed better than those with GWM predictions alone. Buoy-only methods (MEM, BDM, MRM in Section 2.3) and the GWM-buoy combined method, CMB-

ADJ, perform similarly, and suggests that the directional "resolution" of low order buoy moments is comparable to current GWM predictions. Supporting this hypothesis the complexity in directional spectra predictions for moderate to high energy events is well represented by low order buoy directional moments and smoothness assumptions (Section 2.6a). Though GWM predictions may not currently add significant skill to buoy-only swell prediction, GWM predictions are necessary for higher frequency energy that is affected by local winds and not along-crest homogenous offshore. It is not yet clear how to extend our simple combined approach to higher frequencies. However, as GWM predictions improve the simple methodology in our CMB-ADJ method should yield higher skill for swell prediction, and may also be a robust technique in varying regions and wave climates where buoy-only smoothness may fail.

For some applications, e.g. recreational boating, our model errors are small. However, the variance in alongshore radiation stress predictions (S_{xy}) was relatively high despite small ($< 10^o$) wave direction biases. Simple 1D (CERC) transport estimates varied two fold. However, despite large S_{xy} uncertainties, the alongshore gradient of transport (e.g. the divergence of the drift) across all model predictions is surprisingly similar, suggesting that patterns of (theoretical) erosion and accretion may be insensitive to modest boundary condition errors and variations.

2.8 Acknowledgements

Chapter 2, in full, is a reprint with some additions and modifications of the paper, "Modeling Long-Period Swell in Southern California: Practical Boundary Conditions from Buoy Observations and Global Wave Model Predictions" published in the Journal of Atmospheric and Oceanic Technology by S. C. Crosby, W. C. O'Reilly, and R. T. Guza in 2016. The dissertation/thesis author was the primary investigator and author of this

paper.

Appendices

2.A Case Studies

Most mean errors (RMSE and bias) in H_{sig} and θ predictions are $< 25\%$ ($\sim$ 12cm) and $< 10^{\mathrm{o}}$ respectively (Fig. 2.4 and Table 2.2). However, errors during individual wave events can be significant; for example with an energetic unidirectional swell with offshore H_{sig} = 6m and T_m, = 16 sec (Fig. 2.C.1a,b). Directional spectra estimates for the mean frequency and peak wave height (Fig. 2.C.1c) generally agree on the peak direction, however the MEM peak is much shaper than with MRM, WW3, and CMB-ADJ. The sensitivity to energy levels at off-peak directions is clear when comparing direction spectra estimates with model energy transfer coefficients for multiple local deep buoy locations (Fig. 2.C.1d). Owing to sheltering by Pt. Conception and offshore islands the energy transfer cut-off at NW directions is rapid (e.g. Buoy 092 transfer coefficient at 275$^{\mathrm{o}}$) and the amount of energy entering the region depends on details of the tail of the offshore directional spectra (e.g. the discrepancy between MEM- and MRM-initialized models at 275$^{\mathrm{o}}$). All models severely under predicted H_{sig} inside the SBC at buoy 111, with less severe under prediction to the south offshore of Los Angeles at buoy 092 (Fig. 2.C.1e,g).The MEM-initialized model H_{sig} prediction is biased particularly low because the MEM estimate is narrowest, with the least energy on the shoulder. Counter intuitively, the best model-observation agreement is at buoy 045 near Oceanside (Fig. 2.C.1i), where the open window between 250-265$^{\mathrm{o}}$ allows only a small fraction of the total deep water energy to reach the shoreline. However, adjacent frequencies directional spread is wider (not shown) allowing more energy to buoy 045 resulting in a wave height $\sim$1m.

A second case study (Fig. 2.C.2) illustrates a moderate ($H_{\text{sig}} = 2-3$m, $T_m =$ 15sec) swell event with sometimes strong directional bimodality. Here, CMB-ADJ shifted energy from the NW peak to the SW peak and rotated both slightly southward toward the open energy window at buoys 111 and 092 (Fig. 2.C.2d). This peak placement and energy level is in general agreement with MEM and MRM buoy-only methods. Again, MEM creates a very sharp NW peak at 290$^{\text{o}}$ allowing less energy into the region than MRM and CMB-ADJ (MEM is yellow in Fig. 2.C.2e,g). The predictions for θ_1 vary by as much as 40$^{\text{o}}$ at buoy 045, although H_{sig} are in good agreement (with each other, and the observations) owing to canceling errors (Fig. 2.C.2i,j). The skill of these various boundary condition methods vary spatially. In this example, WW3 and MEM are the worst performers at buoys 111 and 092, and the best at buoy 045.

2.B Model transfer coefficients

For each nearshore location of interest, e.g. buoy validation site, backwards ray-tracing relates the nearshore arrival angle, θ, to the offshore arrival $\theta^{(o)}$ (e.g. O'Reilly and Guza, 1998, Fig. 2). Rays are traced seaward following Snell's law as phase speed changes in varying bathymetry (Dobson, 1967). Some rays terminate at offshore islands, indicating blocked arrival directions, others are terminated when they reach deep water seaward of the SC Bight. The transfer coefficient, K^2, is estimated using conservation of energy (depth-limited shoaling) and a simple relation from geometrical-optical theory such that,

$$\frac{E(f,\theta)}{E^{(o)}(f,\theta)} = K^2(f,\theta) = \frac{c_g^{(o)}(f)}{c_g(f)} \left| \frac{\Delta\theta}{\Delta\theta^{(o)}} \right| , \qquad (2.B.1)$$

where c_g is group velocity and (o) indicates offshore properties (Dorrestein, 1960). (Mehaute and Wang, 1982) show that (A2) is equivalent Snell's law and the theoretical work of (Longuet-Higgins, 1957) for slowly varying bathymetry. Rays are traced at a very high directional resolution and carefully integrated to discretize K^2 at 1$^{\mathrm{o}}$ resolution (Dorrestein, 1960). Unlike finite-difference propagation schemes, wave ray integration numerics are stable at any spatial/directional resolution and are only limited by the assumption of slowly-varying bathymetry for linear shallow water waves. Additionally, in this framework, K^2 is typically not a function of offshore position, assuming spatially homogenous and temporally stationary offshore conditions. (Dorrestein, 1960) provides a thorough discussion of this practical method for transforming wave energy nearshore.

2.C Skill Metrics

The metrics used in the paper are estimated from N hour-length records. Given observations, o, and predictions, p, the following formulas are used:

$$
\begin{aligned}
\mathrm{RMSE} &= \sqrt{\frac{1}{N}\sum_{i=1}^{N}(p-o)^2} \\
\%\mathrm{RMSE} &= \sqrt{\frac{1}{N}\sum_{i=1}^{N}\left(\frac{p-o}{o}\right)^2} \\
\mathrm{bias} &= \frac{1}{N}\sum_{i=1}^{N}(p-o) \\
\%\mathrm{bias} &= \frac{1}{N}\sum_{i=1}^{N}\frac{(p-o)}{o} \\
R^2 &= 1-\frac{\sum_{i=1}^{N}(p-o)^2}{\sum_{i=1}^{N}(o-\bar{o})^2} \\
r^2 &= \frac{\left[\sum_{i=1}^{N}(o-\bar{o})(p-\bar{p})\right]^2}{\sum_{i=1}^{N}(o-\bar{o})^2\sum_{i=1}^{N}(p-\bar{p})^2}
\end{aligned}
\tag{2.C.1}
$$

where the overbar indicates a mean. Detailed model results are contained in Tables 2.5,2.6.

Table 2.1: Wave buoy names, depths, and site occupation dates.

NOAA	CDIP	Name	Depth [m]	Start	End
Deep					
46218	071	Harvest	549	2000-Jan	2009-Dec
46216	107	Goleta	182	2002-Jun	2009-Dec
46217	111	Anacapa	114	2002-Jun	2009-Dec
46221	028	Santa Monica	363	2000-Mar	2009-Dec
46222	092	San Pedro	457	2000-Jan	2009-Dec
46223	096	Dana Point	373	2000-Jul	2009-Dec
46224	045	Oceanside	220	2000-Jan	2009-Dec
46225	100	Torrey Pines	549	2001-Jan	2009-Dec
46231	093	Mission Bay	201	2005-Oct	2009-Dec
46226	095	Point La Jolla	181	2000-Jan	2005-Oct
Shallow					
-	131	Rincon Point	21	2005-Sep	2007-Apr
46228	130	Pitas Point	20	2004-Oct	2005-Sep
46234	141	Port Hueneme	21	2007-Apr	2009-Feb
-	118	Leo Carillo	20	2003-Apr	2004-Mar
46230	172	Huntington Beach	22	2005-Jun	2006-Nov
46242	043	Camp Pendleton	20	2008-Jan	2009-Dec
46235	155	Imperial Beach	18	2006-Dec	2009-Dec
-	101	Torrey Pines Inner	20	2001-Apr	2004-Mar

Table 2.2: Mean model skill at local local deep buoys.

Model	$\mathbf{H_{sig}}$ *mean* [m]	*RMSE* [m]	$\lvert Bias \rvert$ [m]	R^2 -	r^2 -	$\bar{\theta}_1$ *RMSE* [^{o}]	$\lvert Bias \rvert$ [^{o}]	R^2 -	r^2 -	$\bar{\sigma}_1$ *RMSE* [^{o}]	*Bias* [^{o}]	R^2 -	r^2 -
WW3	0.65	0.21	0.09	0.53	0.73	15	4	0.72	0.77	14	-11	-1.53	0.41
CMB-E	0.52	0.15	0.06	0.56	0.67	13	4	0.64	0.69	13	-10	-1.61	0.34
CMB-LH	0.51	0.13	0.05	0.60	0.71	13	3	0.65	0.68	11	-9	-1.16	0.33
CMB-ADJ	0.52	0.13	0.03	0.63	0.72	11	2	0.72	0.74	11	-9	-1.06	0.42
MEM	0.51	0.13	0.04	0.63	0.72	11	3	0.69	0.76	10	-8	-0.55	0.45
MRM	0.52	0.12	0.02	0.66	0.73	13	7	0.62	0.74	11	-9	-1.16	0.37
BDM	0.51	0.12	0.03	0.66	0.74	11	5	0.69	0.77	10	-8	-0.56	0.47

Table 2.3: Model skill rankings averaged across deep local buoys for various boundary conditions and select metrics (low ranking indicates higher skill)

Boundary Condition	**H_{sig}** R^2	|Bias|	$\bar{\theta}_1$ R^2	|Bias|	**Total**	Rank
WW3	7	7	6	4	24	7
CMB-E	6	6	5	5	22	6
CMB-LH	5	5	4	2	16	4
CMB-ADJ	3	3	1	1	8	1
MEM	4	4	2	3	13	3
MRM	2	1	7	7	17	5
BDM	1	2	3	6	12	2

Table 2.4: Mean skill for best models (CMB-ADJ, MEM, BDM) ranked across local deep buoys for select metrics (low ranking indicates higher skill). Buoys are listed north to south.

NOAA	**CDIP**	**H_{sig}** R^2	|Bias|	$\bar{\theta}_1$ R^2	|Bias|	**Total**
46216	107	1	9	9	9	28
46217	111	4	8	1	5	18
46221	028	2	2	5	4	13
46222	092	3	7	4	6	20
46223	096	7	6	3	3	19
46224	045	9	5	6	1	21
46225	100	6	4	2	2	14
46231	093	8	3	8	8	27
46226	095	5	1	7	7	20

Table 2.5: Model skill at local deep buoys

NOAA	CDIP	Boundary Condition	H_s *mean* [m]	*RMSE* [m]	*Bias* [m]	R^2 -	r^2 -	$\bar{\theta}_1$ *RMSE* [^{o}]	*Bias* [^{o}]	R^2 -	r^2 -	$\bar{\sigma}_1$ *RMSE* [^{o}]	*Bias* [^{o}]	R^2 -	r^2 -
46218	071	WW3	1.28	0.40	0.23	0.75	0.87	15	2	0.86	0.87	11	-8	0.10	0.65
46216	107	WW3	0.48	0.22	-0.14	0.64	0.79	17	9	0.46	0.63	20	-18	-1.10	0.60
		CMB-E	0.48	0.25	-0.18	0.53	0.81	16	8	0.47	0.64	21	-19	-1.19	0.58
		CMB-LH	0.47	0.20	-0.14	0.69	0.85	17	8	0.37	0.54	20	-18	-1.05	0.63
		CMB-ADJ	0.48	0.16	-0.10	0.80	0.88	16	8	0.52	0.69	19	-17	-0.85	0.68
		MEM	0.47	0.17	-0.11	0.77	0.88	21	11	0.18	0.68	22	-20	-1.35	0.70
		L2	0.47	0.12	-0.04	0.89	0.91	18	11	0.37	0.66	21	-19	-1.12	0.69
		BDM	0.47	0.14	-0.07	0.86	0.91	20	11	0.27	0.71	21	-19	-1.16	0.71
46217	111	WW3	0.51	0.18	0.02	0.63	0.66	17	-4	0.74	0.76	15	-11	-1.18	0.25
		CMB-E	0.51	0.17	-0.06	0.68	0.72	17	-5	0.74	0.78	15	-11	-1.23	0.24
		CMB-LH	0.50	0.15	-0.07	0.72	0.78	14	-3	0.82	0.83	13	-9	-0.63	0.30
		CMB-ADJ	0.51	0.13	-0.03	0.80	0.81	15	-4	0.82	0.84	14	-10	-0.72	0.36
		MEM	0.50	0.16	-0.09	0.68	0.77	13	-3	0.86	0.87	11	-7	-0.09	0.45
		L2	0.50	0.12	-0.04	0.82	0.84	11	3	0.90	0.91	12	-9	-0.34	0.56
		BDM	0.50	0.13	-0.05	0.80	0.83	10	1	0.91	0.91	11	-8	-0.15	0.54
46221	028	WW3	0.57	0.15	0.04	0.59	0.71	12	-1	0.73	0.79	15	-12	-3.23	0.20
		CMB-E	0.57	0.14	-0.04	0.67	0.72	12	-2	0.73	0.78	15	-13	-3.40	0.19
		CMB-LH	0.56	0.12	-0.01	0.74	0.80	11	-1	0.78	0.78	15	-12	-3.02	0.16
		CMB-ADJ	0.57	0.12	0.02	0.73	0.81	10	-1	0.82	0.83	14	-12	-2.76	0.27
		MEM	0.57	0.11	-0.02	0.78	0.81	9	1	0.85	0.86	12	-11	-1.85	0.31
		L2	0.57	0.12	-0.01	0.74	0.81	14	9	0.67	0.82	14	-13	-2.82	0.26
		BDM	0.57	0.11	-0.01	0.78	0.82	11	5	0.80	0.86	13	-11	-1.89	0.35
46222	092	WW3	0.51	0.20	-0.09	0.54	0.72	20	3	0.72	0.74	14	-10	-0.39	0.47
		CMB-E	0.51	0.21	-0.15	0.47	0.74	20	4	0.72	0.74	13	-10	-0.35	0.49
		CMB-LH	0.49	0.18	-0.10	0.59	0.75	20	4	0.72	0.74	13	-9	-0.31	0.45
		CMB-ADJ	0.51	0.15	-0.05	0.74	0.82	16	1	0.83	0.84	14	-11	-0.38	0.60
		MEM	0.51	0.15	-0.08	0.73	0.80	15	4	0.85	0.87	9	-6	0.39	0.68
		L2	0.51	0.13	0.01	0.80	0.83	15	4	0.85	0.86	10	-7	0.21	0.62
		BDM	0.51	0.12	-0.03	0.82	0.84	14	4	0.87	0.88	9	-6	0.38	0.67
46223	096	WW3	0.59	0.18	0.03	0.40	0.63	15	-2	0.76	0.77	15	-13	-2.60	0.40
		CMB-E	0.59	0.15	-0.06	0.57	0.68	15	-2	0.76	0.78	15	-13	-2.61	0.40
		CMB-LH	0.59	0.13	-0.06	0.63	0.75	14	-2	0.76	0.76	13	-11	-1.78	0.41
		CMB-ADJ	0.59	0.13	-0.01	0.67	0.73	12	-1	0.84	0.85	13	-11	-1.80	0.46
		MEM	0.59	0.13	-0.06	0.64	0.73	11	-2	0.87	0.87	11	-9	-0.77	0.51
		L2	0.59	0.13	-0.05	0.65	0.73	16	9	0.72	0.83	12	-9	-1.19	0.39
		BDM	0.59	0.13	-0.05	0.67	0.75	12	4	0.85	0.87	10	-8	-0.52	0.55
46224	045	WW3	0.57	0.15	0.02	0.47	0.63	14	-5	0.64	0.68	15	-13	-3.66	0.25
		CMB-E	0.57	0.14	-0.05	0.53	0.66	14	-5	0.64	0.68	15	-13	-3.76	0.24
		CMB-LH	0.56	0.12	-0.04	0.62	0.71	13	-2	0.65	0.66	14	-12	-2.86	0.27
		CMB-ADJ	0.57	0.13	-0.01	0.59	0.69	10	-1	0.81	0.81	13	-12	-2.67	0.37
		MEM	0.57	0.13	-0.05	0.59	0.70	9	-1	0.83	0.85	11	-9	-1.35	0.41
		L2	0.57	0.14	-0.06	0.52	0.69	15	10	0.59	0.80	12	-10	-2.03	0.23
		BDM	0.57	0.13	-0.05	0.56	0.71	10	5	0.81	0.85	10	-9	-1.05	0.46
46225	100	WW3	0.65	0.20	0.10	0.41	0.74	13	-1	0.76	0.80	10	-8	-1.07	0.44
		CMB-E	0.65	0.13	0.00	0.74	0.79	13	-1	0.78	0.80	10	-8	-1.12	0.46
		CMB-LH	0.64	0.14	-0.00	0.70	0.81	11	-1	0.83	0.83	9	-6	-0.51	0.44
		CMB-ADJ	0.65	0.14	0.02	0.69	0.81	10	-1	0.86	0.86	8	-6	-0.32	0.53
		MEM	0.64	0.13	-0.03	0.72	0.82	10	-1	0.87	0.87	7	-5	0.01	0.53
		L2	0.64	0.13	-0.03	0.73	0.82	13	8	0.76	0.85	10	-7	-0.93	0.34
		BDM	0.64	0.13	-0.02	0.73	0.82	10	4	0.86	0.88	7	-5	-0.06	0.54
46231	093	WW3	0.69	0.22	0.12	0.40	0.75	14	5	0.77	0.82	9	-6	-0.43	0.48
		CMB-E	0.69	0.16	0.02	0.69	0.79	13	5	0.79	0.83	9	-6	-0.48	0.50
		CMB-LH	0.69	0.16	0.01	0.65	0.81	13	5	0.81	0.84	8	-6	-0.22	0.42
		CMB-ADJ	0.69	0.18	0.04	0.57	0.79	12	4	0.82	0.84	8	-5	-0.10	0.52
		MEM	0.69	0.16	-0.01	0.67	0.81	12	5	0.81	0.85	8	-5	0.02	0.49
		L2	0.69	0.16	0.00	0.66	0.81	17	12	0.64	0.83	11	-9	-1.23	0.27
		BDM	0.69	0.16	0.00	0.67	0.82	15	9	0.74	0.85	9	-6	-0.26	0.44
46226	095	WW3	0.61	0.21	0.09	0.43	0.79	13	4	0.75	0.82	11	-9	-1.74	0.35
		CMB-E	0.61	0.13	-0.01	0.77	0.84	12	4	0.77	0.83	11	-9	-1.91	0.35
		CMB-LH	0.59	0.14	-0.02	0.70	0.86	11	3	0.81	0.83	9	-7	-1.20	0.26
		CMB-ADJ	0.61	0.16	0.02	0.69	0.86	10	2	0.83	0.85	9	-7	-1.02	0.42
		MEM	0.61	0.15	-0.02	0.71	0.85	11	2	0.82	0.83	8	-6	-0.54	0.41
		L2	0.61	0.14	-0.00	0.74	0.86	14	9	0.71	0.83	12	-10	-2.17	0.32
		BDM	0.61	0.14	-0.01	0.74	0.86	11	7	0.79	0.87	9	-8	-0.92	0.44

Table 2.6: Model skill at local shallow buoys

NOAA	CDIP	Model	H_s *mean* [m]	*RMSE* [m]	*Bias* [m]	R^2 -	r^2 -	$\bar{\theta}_1$ *RMSE* [^{o}]	*Bias* [^{o}]	R^2 -	r^2 -	$\bar{\sigma}_1$ *RMSE* [^{o}]	*Bias* [^{o}]	R^2	r^2
-	131	WW3	0.35	0.17	-0.10	0.42	0.65	11	-6	0.33	0.65	17	-15	-2.39	0.14
		CMB-E	0.35	0.19	-0.14	0.34	0.71	10	-6	0.33	0.64	17	-15	-2.41	0.14
		CMB-LH	0.35	0.15	-0.10	0.56	0.75	8	-2	0.66	0.70	16	-14	-2.09	0.31
		CMB-ADJ	0.35	0.11	-0.06	0.76	0.85	8	-3	0.64	0.75	17	-15	-2.32	0.29
		MEM	0.35	0.12	-0.08	0.73	0.85	6	2	0.81	0.84	16	-14	-1.89	0.50
		L2	0.35	0.08	-0.02	0.87	0.88	6	2	0.81	0.85	16	-15	-2.16	0.47
		BDM	0.35	0.09	-0.05	0.83	0.88	5	2	0.83	0.87	16	-14	-1.99	0.50
46228	130	WW3	0.35	0.15	-0.08	0.41	0.59	10	-7	0.49	0.71	16	-14	-2.55	0.07
		CMB-E	0.35	0.16	-0.12	0.31	0.68	10	-7	0.48	0.71	16	-14	-2.61	0.07
		CMB-LH	0.35	0.13	-0.10	0.52	0.78	9	-4	0.65	0.74	16	-14	-2.40	0.15
		CMB-ADJ	0.35	0.10	-0.06	0.72	0.83	8	-4	0.69	0.79	16	-14	-2.60	0.19
		MEM	0.35	0.12	-0.08	0.61	0.79	6	-1	0.83	0.87	15	-13	-1.95	0.33
		L2	0.35	0.09	-0.04	0.81	0.85	6	0	0.83	0.84	15	-14	-2.26	0.28
		BDM	0.35	0.10	-0.06	0.76	0.84	6	-0	0.85	0.87	15	-13	-2.07	0.31
46234	141	WW3	0.50	0.16	0.08	0.30	0.58	10	4	0.68	0.72	15	-13	-4.44	0.13
		CMB-E	0.50	0.12	-0.00	0.61	0.67	10	4	0.67	0.72	15	-13	-4.57	0.15
		CMB-LH	0.50	0.11	-0.02	0.64	0.70	9	3	0.70	0.74	14	-12	-3.76	0.15
		CMB-ADJ	0.50	0.11	0.01	0.67	0.71	9	4	0.75	0.81	13	-12	-3.66	0.17
		MEM	0.50	0.11	-0.04	0.66	0.72	8	2	0.77	0.81	12	-11	-3.05	0.21
		L2	0.50	0.10	-0.01	0.73	0.75	9	4	0.74	0.81	10	-9	-1.76	0.26
		BDM	0.50	0.10	-0.02	0.73	0.75	8	3	0.77	0.82	11	-10	-2.22	0.25
-	118	WW3	0.49	0.16	0.05	-0.12	0.54	7	-4	0.64	0.73	15	-14	-5.92	0.08
		CMB-E	0.49	0.12	-0.03	0.37	0.60	7	-4	0.63	0.72	15	-14	-5.96	0.07
		CMB-LH	0.49	0.09	-0.01	0.69	0.76	7	-2	0.70	0.75	14	-13	-5.31	0.10
		CMB-ADJ	0.49	0.08	0.01	0.70	0.80	6	-3	0.77	0.84	15	-14	-5.63	0.13
		MEM	0.49	0.07	-0.01	0.77	0.81	5	-2	0.81	0.87	13	-12	-4.73	0.17
		L2	0.49	0.08	-0.02	0.73	0.83	4	0	0.86	0.86	13	-12	-4.43	0.16
		BDM	0.49	0.07	-0.02	0.77	0.83	5	-1	0.85	0.88	13	-12	-4.32	0.18
46230	172	WW3	0.49	0.18	0.03	0.06	0.56	10	-1	0.66	0.68	19	-18	-5.19	0.21
		CMB-E	0.49	0.14	-0.05	0.43	0.61	10	-1	0.64	0.67	19	-18	-5.20	0.22
		CMB-LH	0.49	0.12	-0.07	0.55	0.71	10	-2	0.60	0.63	19	-17	-4.71	0.20
		CMB-ADJ	0.49	0.11	-0.04	0.64	0.70	9	-1	0.73	0.76	18	-17	-4.51	0.25
		MEM	0.49	0.12	-0.06	0.59	0.72	10	-4	0.60	0.76	18	-16	-4.39	0.25
		L2	0.49	0.13	-0.08	0.46	0.67	8	-1	0.74	0.76	15	-14	-2.89	0.33
		BDM	0.49	0.12	-0.07	0.56	0.72	9	-3	0.69	0.79	16	-14	-3.38	0.29
46242	043	WW3	0.51	0.16	0.07	0.25	0.63	8	-3	0.46	0.53	13	-12	-4.70	0.22
		CMB-E	0.51	0.12	-0.00	0.53	0.66	7	-2	0.48	0.53	13	-12	-4.77	0.24
		CMB-LH	0.52	0.12	-0.03	0.58	0.69	6	-0	0.56	0.57	12	-11	-4.29	0.25
		CMB-ADJ	0.51	0.12	-0.00	0.58	0.66	6	-1	0.64	0.65	12	-11	-3.85	0.22
		MEM	0.52	0.12	-0.04	0.57	0.68	5	1	0.73	0.75	10	-9	-2.88	0.36
		L2	0.52	0.13	-0.06	0.50	0.68	8	6	0.25	0.70	10	-9	-3.05	0.19
		BDM	0.52	0.12	-0.05	0.55	0.69	6	3	0.64	0.75	10	-9	-2.59	0.36
46235	155	WW3	0.55	0.23	0.10	0.35	0.82	10	7	0.54	0.77	10	-9	-3.07	0.26
		CMB-E	0.55	0.18	0.02	0.60	0.83	9	6	0.58	0.79	11	-10	-3.27	0.25
		CMB-LH	0.55	0.19	0.02	0.56	0.86	11	7	0.42	0.71	10	-9	-2.92	0.20
		CMB-ADJ	0.55	0.23	0.06	0.34	0.85	10	7	0.47	0.75	10	-9	-2.92	0.31
		MEM	0.55	0.19	0.02	0.56	0.86	12	8	0.29	0.72	10	-9	-3.14	0.36
		L2	0.55	0.22	0.07	0.38	0.86	12	8	0.29	0.71	12	-11	-4.33	0.26
		BDM	0.55	0.21	0.05	0.47	0.87	12	8	0.29	0.74	11	-10	-3.56	0.35
-	101	WW3	0.49	0.16	0.04	0.70	0.80	7	-3	0.69	0.77	11	-9	-3.35	0.04
		CMB-E	0.49	0.12	-0.04	0.82	0.84	7	-3	0.68	0.78	11	-9	-3.53	0.04
		CMB-LH	0.48	0.10	-0.01	0.88	0.90	6	-3	0.73	0.80	10	-9	-2.91	0.03
		CMB-ADJ	0.49	0.11	0.01	0.85	0.89	5	-2	0.79	0.83	10	-9	-2.70	0.11
		MEM	0.48	0.09	-0.01	0.89	0.90	6	-2	0.69	0.80	10	-8	-2.54	0.13
		L2	0.48	0.10	0.01	0.87	0.91	4	1	0.85	0.86	10	-9	-3.25	0.22
		BDM	0.48	0.09	0.00	0.89	0.91	4	-0	0.86	0.89	10	-9	-2.60	0.23

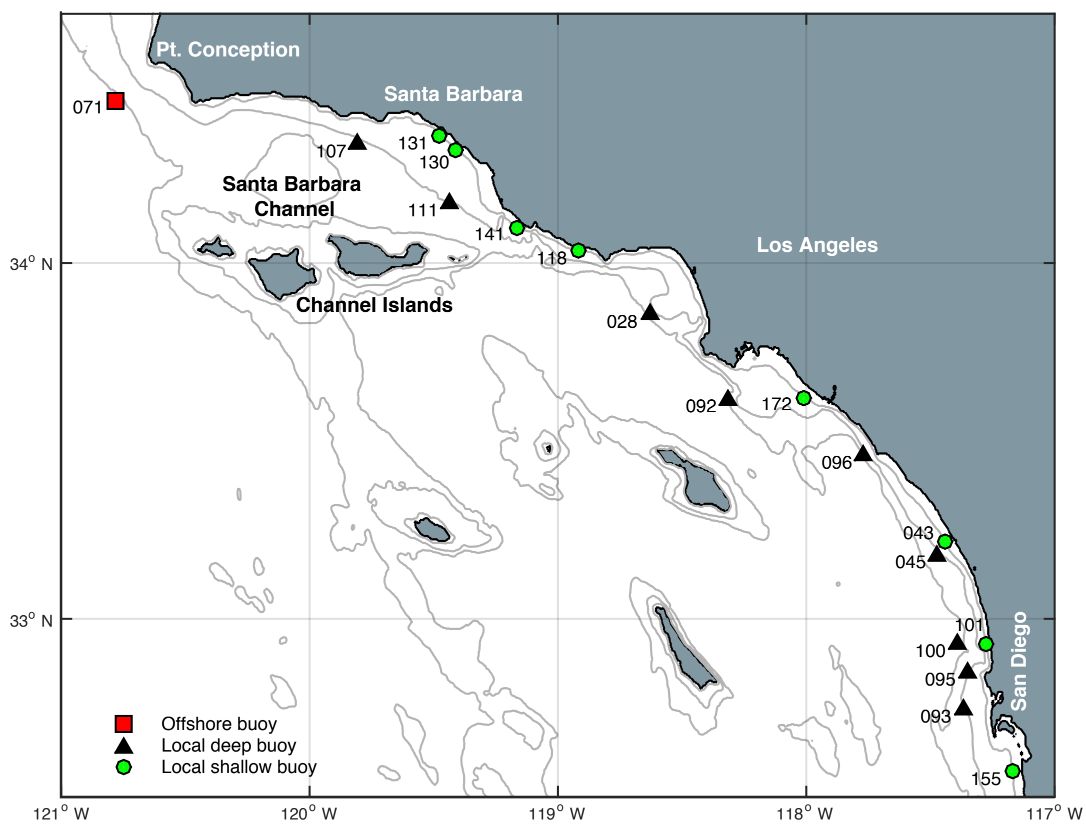

Figure 2.1: Southern California map showing offshore buoy (071, square) in 550m depth used to initialize regional model, local deep validation buoys (black triangles) in depths 100-500m, and local shallow validation buoys (circles) in 20m depth. Grey contours show 20m, 100m, and 500m isobaths

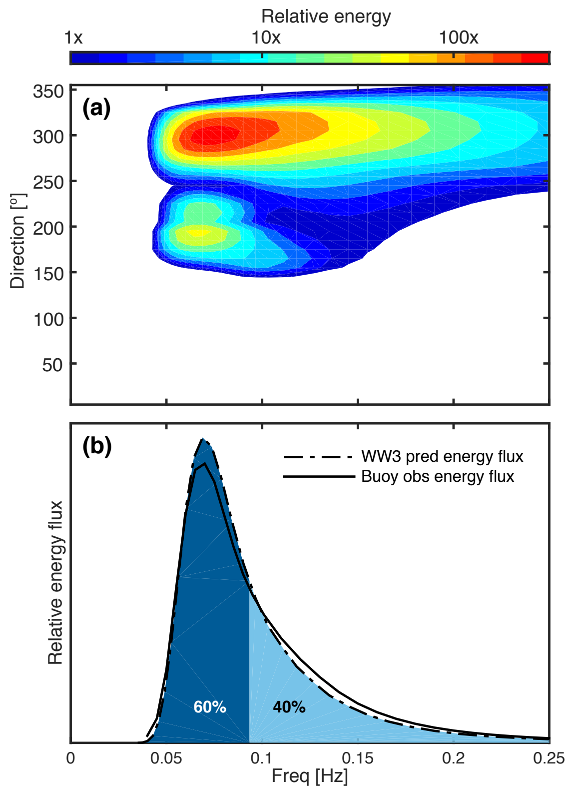

Figure 2.2: 10-year mean wave conditions at offshore buoy 071. (a) Mean GWM (NOAA-WW3) wave energy predictions (color) versus frequency and direction. (b) GWM (dashed) and buoy measured (solid) mean energy flux (Ec_g) versus frequency (integrated over direction). Swell (0.04-0.09Hz) and sea (0.09-0.25Hz) frequency bands account for 60% and 40% of the offshore energy flux respectively.

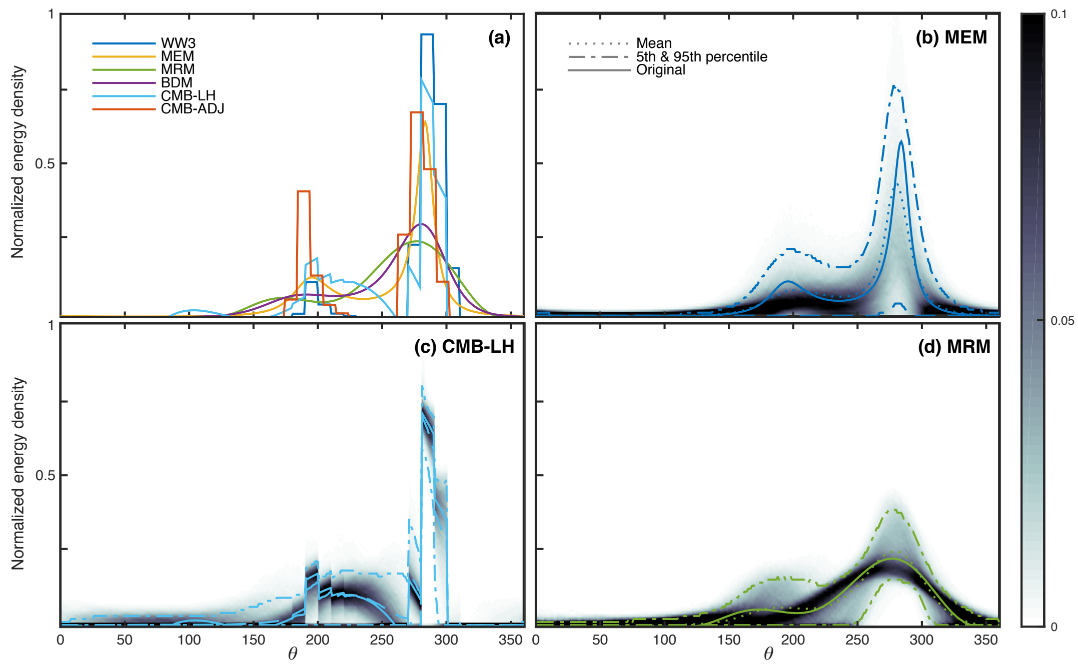

Figure 2.3: (a) Normalized (to unit area) energy density versus direction for a typical swell frequency band, at offshore buoy 071. Methods (see legend) are buoy only (MEM, MRM, BDM), model only (WW3), and combinations (CMB-LH, CMB-ADJ). (b,c,d) Probability distributions (likelihood greyscale on right) for (b) MEM, (c) CMB-LH, and (d) MRM for the expected uncertainty in a 1-hour record (DOF=64). Solid colored curves repeat curves in (a). Mean and scatter (5% and 95% levels, see legend in (b)) are also shown.

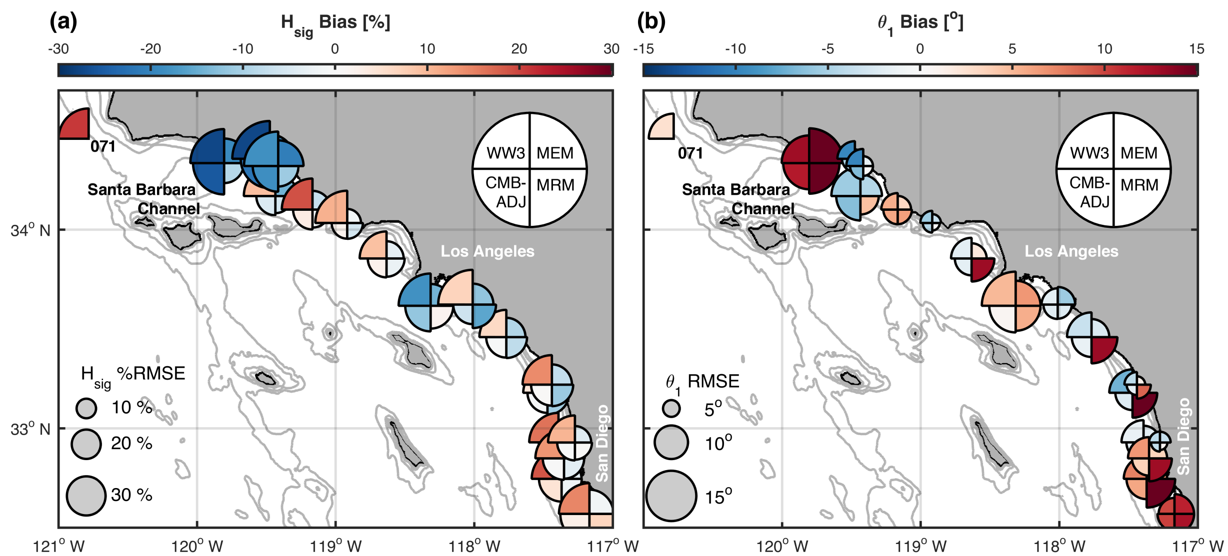

Figure 2.4: Model performance at each southern California nearshore buoy location for (a) wave height H_{sig} and (b) wave direction θ_1. Each circle quadrant shows a different boundary condition (key, upper right). Circle quadrant size shows RMSE error (key, lower left), and color shows bias (bar, above). Normalized error metrics (%RMSE and %bias, Section 2.C) are used in (a). A small quadrant indicates small RMSE error, and a pale color indicates small bias. GWM (NOAA-WW3) initialization (upper left quadrant), in all regions and for both H_{sig} and θ_1, is relatively large and dark, indicating relatively high RMSE and bias. Grey contours show 20, 50, 100, and 500m depth isobaths.

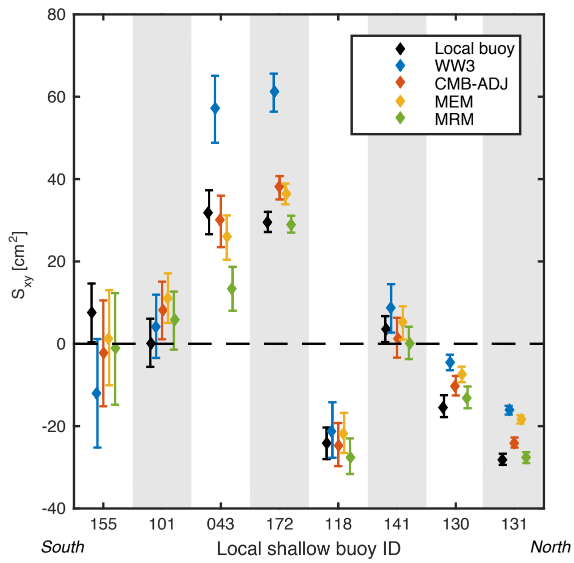

Figure 2.5: Observed (black, local buoy) and predicted (using methods in legend) mean S_{xy} at local shallow (20m depth) buoy sites (arranged South to North on x-axis). Positive S_{xy} values indicate northward up-coast transport. Bars indicate S_{xy} range for $\pm 2.5^o$ local shore normal rotation. Predictions are offset horizontally for clarity.

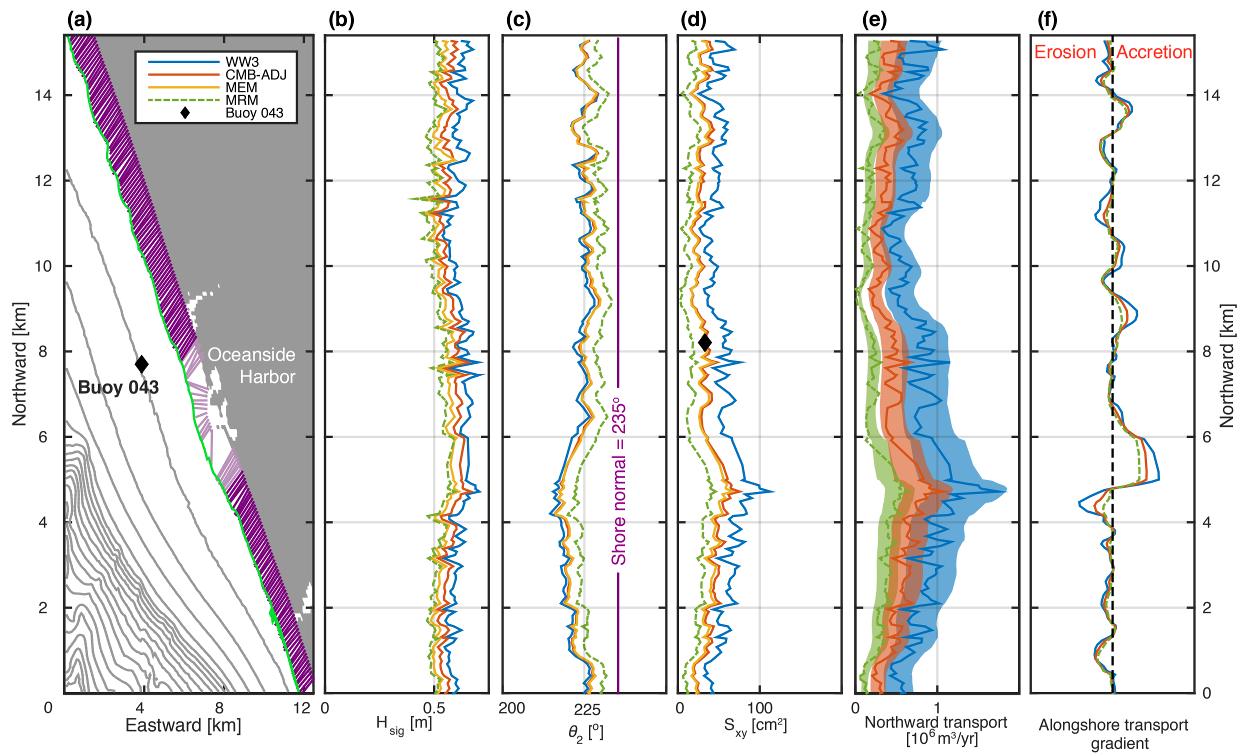

Figure 2.6: (a) Plan view of Oceanside Harbor with buoy 043 (black diamond) and depth contours (grey curves, 20m intervals). Local beach normal (magenta) are based on nearest distance from backshore point to 10m depth contour (green curve). Predicted and observed, time-averaged, (b) H_{sig} and (c) θ_2 in 10m depth versus alongshore distance for different boundary conditions (see legend). (d) Predicted mean S_{xy} at 10m depth versus alongshore distance is estimated using the alongshore mean shore normal (magenta) that excludes the harbor region where shore normal are poorly defined (light magenta in (a)). Buoy measured mean S_{xy} in 20m depth is also shown (black diamond). (e) Predicted sediment transport using CERC formula, $K = 0.6$, versus alongshore distance. Shaded colors show alongshore-smoothed (LOWESS 1.5km alongshore filter) transport estimates for the range of K values $0.4 < K < 0.8$. (f) Gradient of LOWESS filtered transport alongshore (e.g. the divergence of the drift) versus alongshore distance.

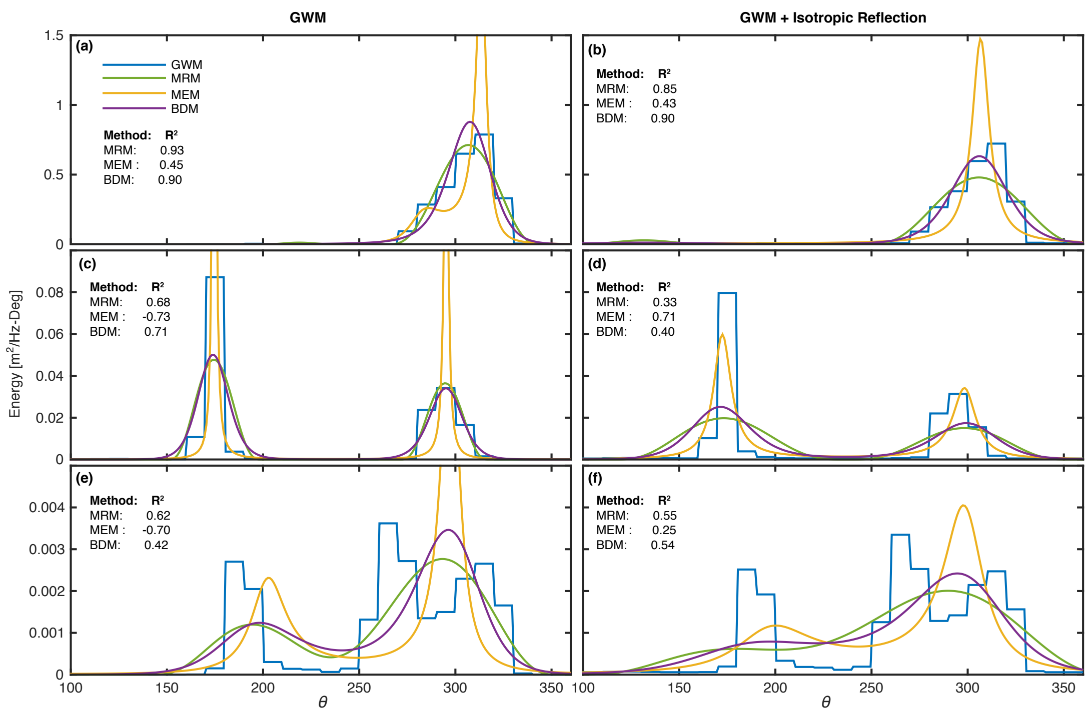

Figure 2.7: Offshore wave energy versus direction for three cases: (a) and (b) unimodal, (c) and (d) bi-modal, and (e) and (f) multi-modal. Left panels show GWM (NOAA-WW3) directional spectra (blue) and recreations using various smoothness methods (see Section 2.3) and 2nd order moments (a_1, b_1, a_2, b_2 in Eq 2) integrated from the GWM spectrum). Right panels show GWM spectrum with an added isotropic signal equal to 10% of the total spectrum energy simulating diffuse wave reflection, and corresponding smooth recreation. R^2 (see tables) of the recreation with the original spectrum (GWM or GWM+isotropic reflection) show that simple, uni-modal distributions are better recreated than mulit-modal shapes. R^2 varies substantially in the presence of isotropic noise as well as between recreation methods.

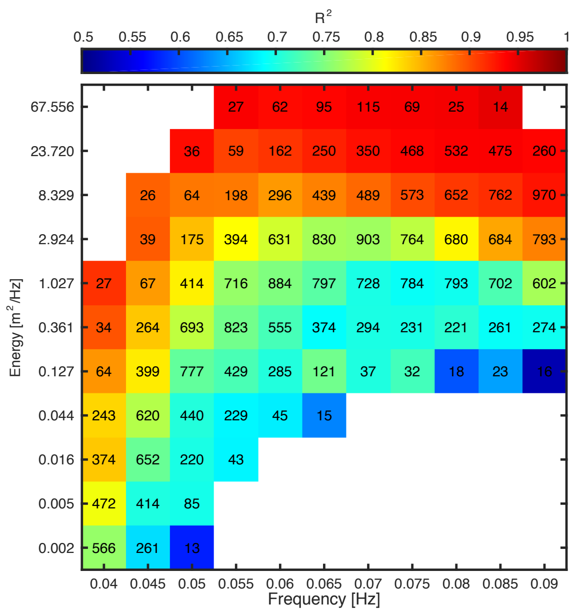

Figure 2.8: Mean R^2 between GWM directional spectrum compared and recreation with 2nd order moments (a_1, b_1, a_2, b_2 in Eq 2) and MRM smoothness method (Section 2.3) versus frequency (x-axis) and offshore GWM energy (y-axis). Black text is number of 3-hour GWM predictions in each frequency-energy bin for the 1-year (2006) of GWM predictions used. Note log-scale for energy (y-axis).

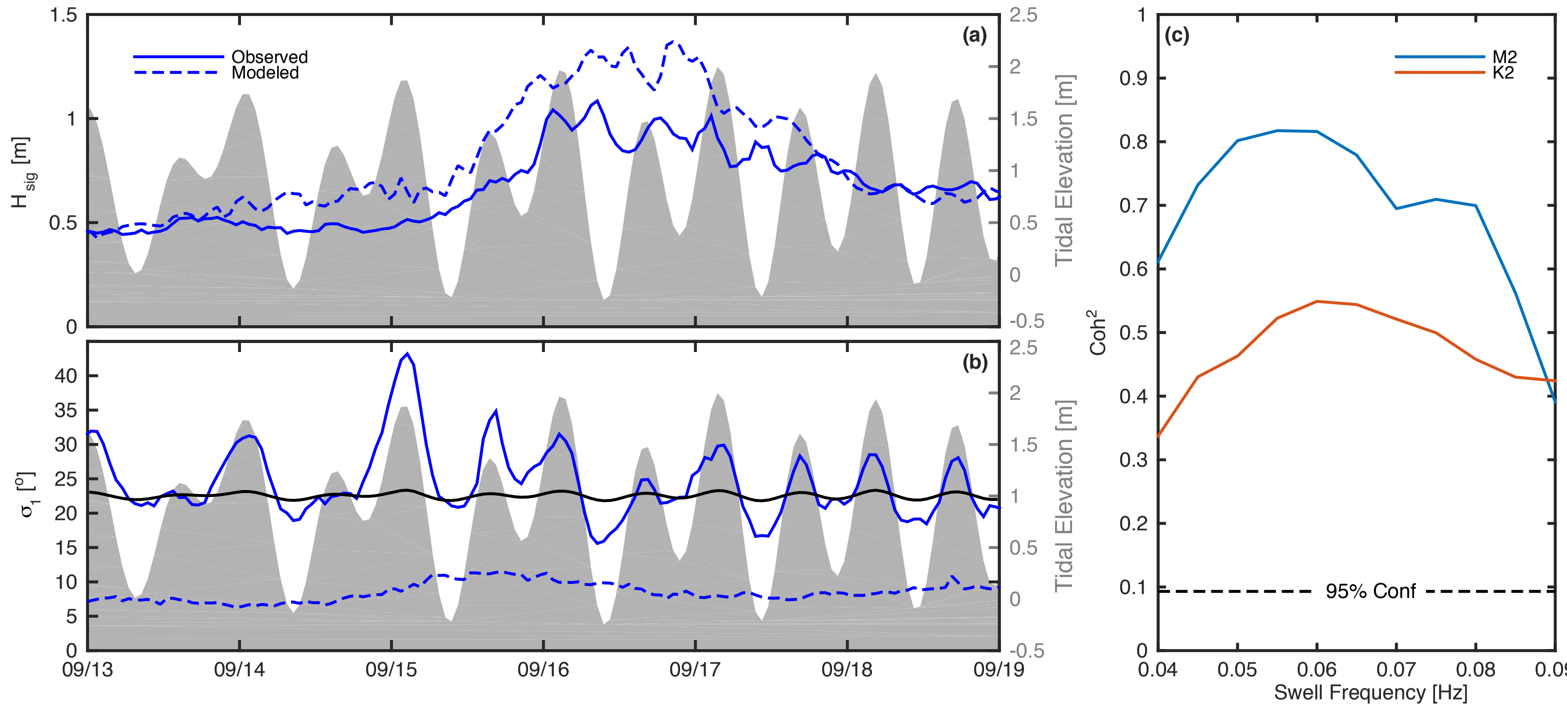

Figure 2.9: (a) H_{sig} and (b) directional spread (σ_1) versus time (UTC) for a low frequency swell event ($f \sim 0.06$Hz) at buoy 172 in 20m depth. Predicted tidal elevation in grey. The tidal modulation of σ_1 (solid blue), likely caused by coastal reflection, is not parameterized in modeled predictions (dashed blue, CMB-ADJ boundary condition). Modulation due to increased refraction at lower tidal levels (directional narrowing) is small, as shown for a constant σ of 22.5-deg (black). (c) Coherence between tidal elevation and $\sigma_1(f)$ at M2 and K2 tidal frequencies (see legend) for one complete year of buoy observations is significantly high for wave energy where $0.04\text{Hz} \leq f \leq 0.09\text{Hz}$ (x-axis). Black dashed line shows the 95% coherence confidence level.

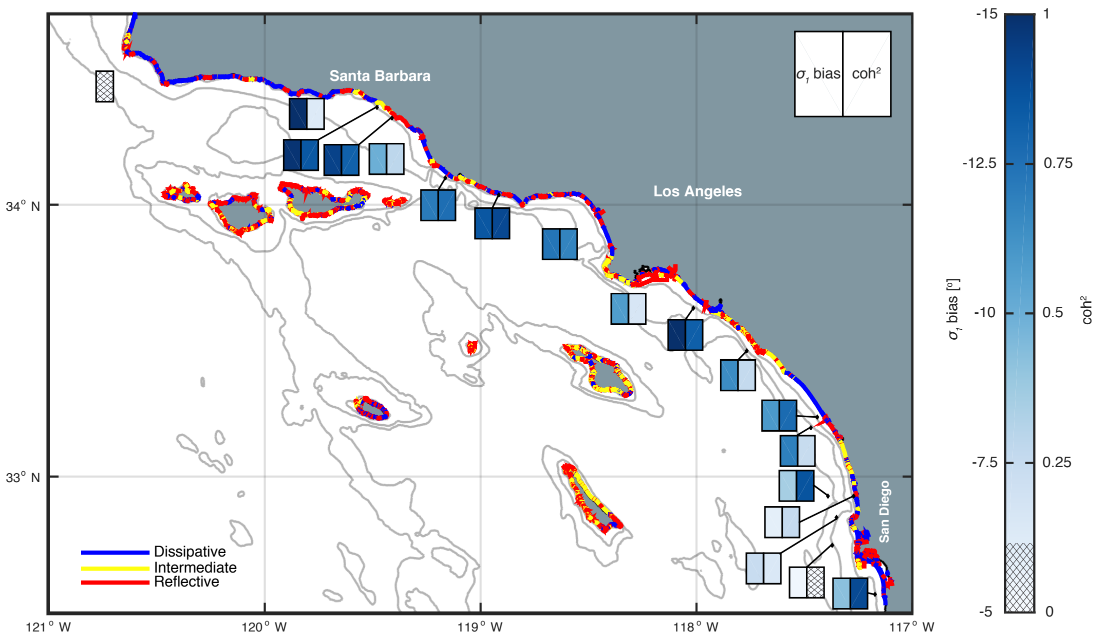

Figure 2.10: Model (CMB-ADJ boundary condition) directional spread (σ_1) prediction bias at local buoy sites shown in color (see colorbar) in left half of square. Right half shows coherence at the M2 tidal frequency (1.9 cycle-per-day) of buoy-observed $\sigma_1(f = 0.055\text{Hz})$ and local tidal elevation (see colorbar). Hatched colors indicate insignificant coherence levels at 95% confidence. The coastline is classified as dissipative (fine to coarse sand), intermediate (gravel), and reflective (riprap, rocky cliffs, seawall) types shown in color (see legend bottom left).

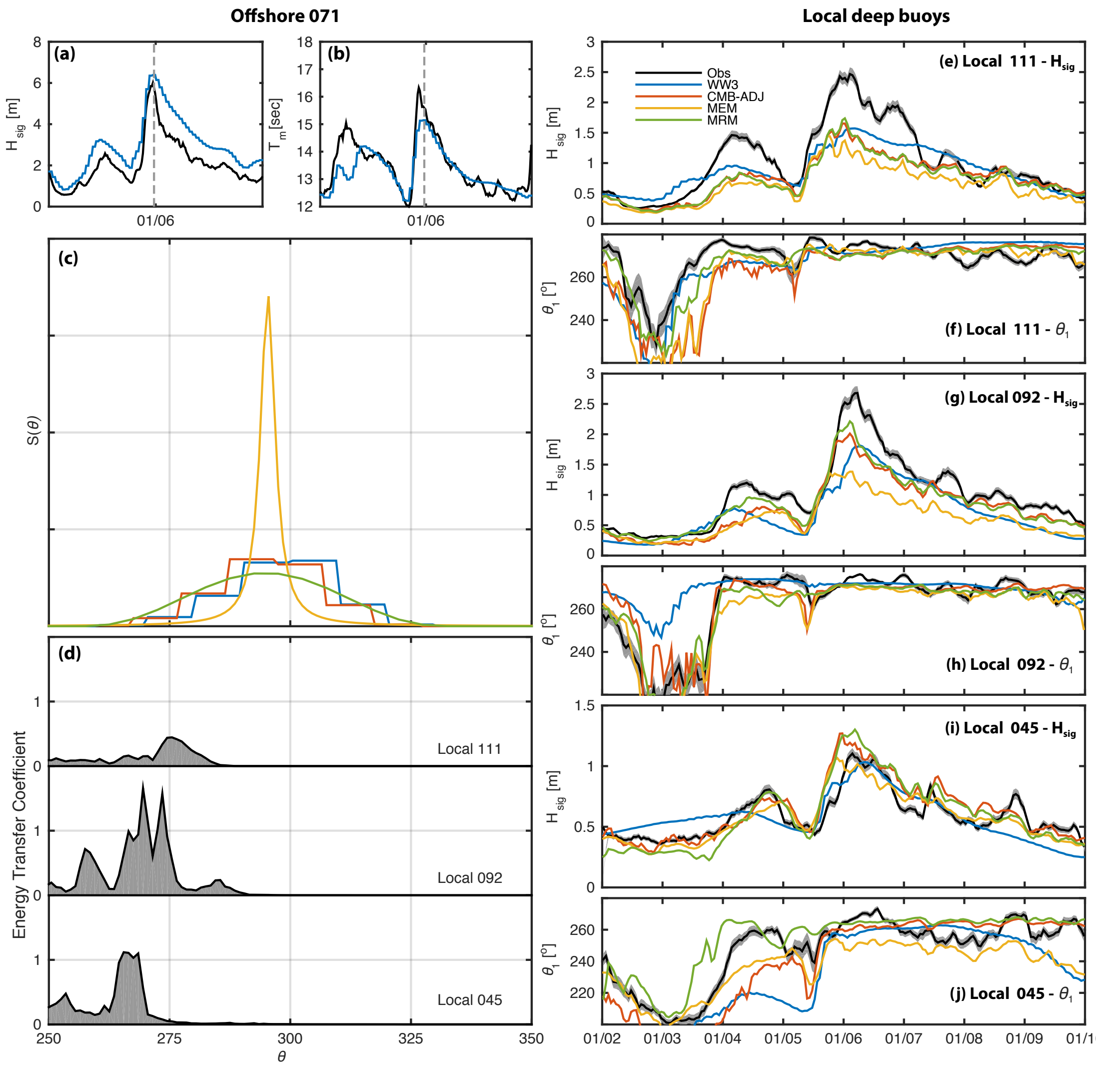

Figure 2.C.1: Extreme wave conditions during January 2008. Offshore (a) H_{sig} and (b) T_c versus time, in UTC. (c) Normalized offshore $S(\theta)$ versus θ at the mean period, $T_m = 1/f_m = \int E(f)\,df / \int fE(f)\,df$, and time marked by grey dashed line in (a) and (b). (d) Offshore energy transfer function versus θ at T_c for local buoys. Nearshore observations and predictions (see legend) also shown at local buoy sites (e-f) 111, (g-h) 092, and (i-j) 045. Note vertical scales vary. Grey shading around observations shows 5th and 95th percentile confidence bounds for the 3-hour smoothed record.

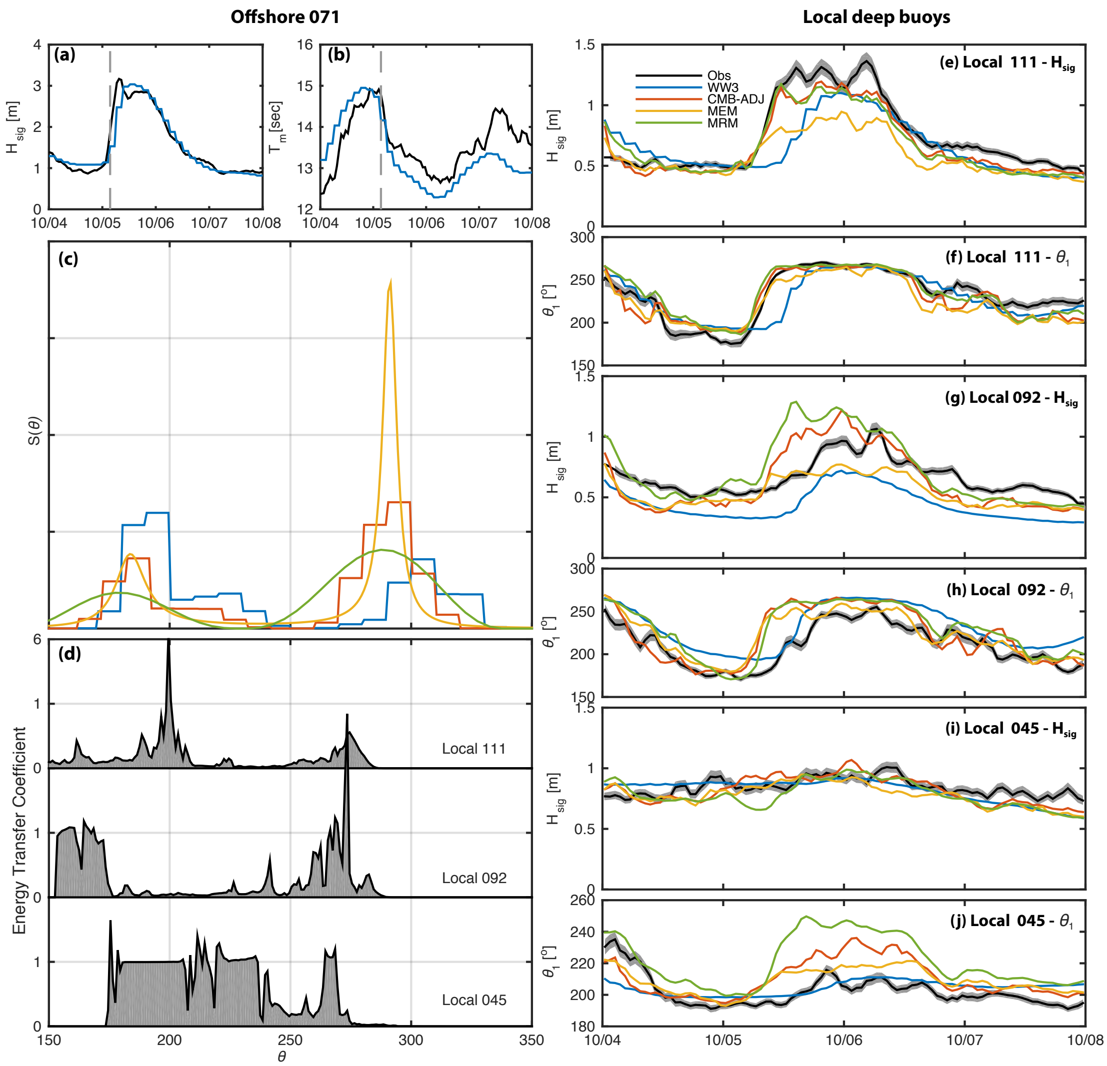

Figure 2.C.2: Same as Fig. 2.C.1, but for October 2008.

Chapter 3

Regional assimilation framework

3.1 Introduction

Coastally incident wave energy drives nearshore processes including beach erosion, along- and cross-shore transport, and flooding and inundation. High-resolution nearshore wave predictions support beach and boater safety, coastal risk assessment, and nearshore process research. Regional wave estimate errors are often dominated by uncertainties in the offshore boundary forcing (O'Reilly and Guza, 1993; Rogers et al., 2007; O'Reilly et al., 2016) that can be reduced by assimilating nearshore observations. Widely-available directional buoy observations have low directional resolution (Ochoa and Delgado-González, 1990). However, multiple observations sheltered from varying directions can be combined to increase resolution, similar to scatter in inhomogeneous media (Borcea et al., 2002). Though current operational wave models, e.g. Simulating WAves Nearshore (SWAN) or Wave Watch III (WW3), do not yet assimilate local wave observations, progress is being made. Recent developments (Veeramony et al., 2010; Orzech et al., 2013) use variational methodologies, relying on an adjoint model to propagate prediction misfits at local observation sites backwards to the model boundary. An analytical adjoint (Walker, 2006), developed originally for Synthetic Aperture Radar satellite observations, has been extended to wave spectra (Veeramony et al., 2010), however, simulations were limited to linear wave processes (shoaling and refraction) and stationary conditions with homogeneous boundary forcing. Numerical methods have been developed to estimate an adjoint by linearizing the SWAN model (Orzech et al., 2013), however, initial tests are restricted to linear wave processes and stationary conditions. More recently adjoint-free techniques have been developed, though initial testing has been restricted to synthetic data (Panteleev et al., 2015).

Linear wave propagation assumptions are valid for low frequency wave energy in many nearshore regions where local fetch is limited and dissipation on a narrow shelf is negligible, e.g. the Southern California Bight (SCB) (O'Reilly and Guza, 1993; O'Reilly et al., 2016). However in regions as large as the SCB ($\sim$ 350km), propagation time-lags are up to 10 hours and cannot be ignored (Rogers et al., 2007). Here, we present an alternative methodology for assimilating nearshore buoy observations that incorporates propagation time lags in a linear wave model. The preliminary analysis of O'Reilly and Guza (1998) (that includes time lags) is extended to include global wave model (GWM) predictions. A comparatively more general inversion framework is developed that incorporates observation uncertainty and a priori information. In contrast to recent assimilation work with SWAN, our alternative approach takes advantage of self-adjoint ray projection. Using historically under-appreciated backwards ray-tracing techniques (Dorrestein, 1960; Longuet-Higgins, 1957) linear transfer coefficients between offshore and nearshore sites are generated. The resulting linear model and adjoint for wave energy propagation greatly reduces computational expense compared with variational systems (Veeramony et al., 2010; Orzech et al., 2013), and allows for high spatial, temporal, and directional resolution. Our case studies with real buoy observations in the SCB show that inverted offshore wave conditions are plausibly smooth in time and direction, and that assimilation of nearshore buoys increases the predictive skill at validation buoy sites not included in the assimilation.

This linear approach is limited to wave conditions, frequencies, and distances where dissipation and nonlinear spectral energy transfers are negligible. Offshore GWM predictions in Southern California (spatial scales of a few 100km) suggest that linear wave propagation assumptions are valid for swell frequencies <0.09Hz, which contains 60% of total offshore energy flux (Crosby et al., 2016, - Appendix A). Assimilation of higher frequency observations requires more sophisticated techniques, more similar to current variational methodology. However, the feasibility of representing non-linear wind-wave growth, dissipation, and spectral energy transfers accurately in a numerically tractable model adjoint remains to be demonstrated.

Wave buoy observations are discussed in Section 3.2, followed by details of the linear forward model in Section 3.3. The assimilation methodology (Section 3.4 and applications to synthetic and real observations in Section 3.5 are followed by a discussion of the model constraints and implications for buoy array design in Section 3.6. Section 3.7 summarizes.

3.2 Observations

Hourly, quality-controlled, Datawell directional buoy observations (Table 3.1) from the Coastal Data Information Program (CDIP, http://cdip.ucsd.edu) are smoothed with a 3-hour running mean. Comparison with a tower-mounted array of pressure sensors shows Datawell directional buoys accurately measure energy and four directional moments (O'Reilly et al., 1996). At the i^{th} buoy mooring location, at each frequency, f, the observed moments, $\tilde{\mathbf{y}}$, are related to the phase averaged wave spectrum, $E(f,\theta)$

(Longuet-Higgins et al., 1963),

$$\tilde{\mathbf{y}}(i,f) = \begin{bmatrix} a_0(f) \\ a_1(f) \\ b_1(f) \\ a_2(f) \\ b_2(f) \end{bmatrix} = \begin{bmatrix} \int E(f,\theta)\,d\theta \\ \int E(f,\theta)\cos\theta\,d\theta \\ \int E(f,\theta)\sin\theta\,d\theta \\ \int E(f,\theta)\cos 2\theta\,d\theta \\ \int E(f,\theta)\sin 2\theta\,d\theta \end{bmatrix}. \tag{3.1}$$

These integral moments, $\tilde{\mathbf{y}}$, of the directional wave spectrum can be transformed into several mean properties, e.g. mean direction (θ_m), directional spread, and others (Kuik et al., 1988), but do not define a unique discrete directional spectrum (Ochoa and Delgado-González, 1990; Crosby et al., 2016). Additionally, observed buoy moments contain statistical uncertainty owing to finite-length observation records (Long, 1980), see also the Appendix B.

Buoy locations in the SCB (Fig. 3.1) were determined by user needs (e.g. harbor entrances) and logistics (e.g. mooring depth constraints). Shallow ($\sim$20m) and deep ($>$300m) water buoys are denoted by S# and D# respectively.

3.3 Forward model

The SCB shelf is narrow, and swell energy transformation is assumed to be dominated by island sheltering and bathymetry-controlled refraction. Wind generation, spectral energy transfers, wave-current interactions, and dissipation are neglected (O'Reilly and Guza, 1993; O'Reilly et al., 2016). Wind generation and dissipation were negligible on the similarly narrow Pacific Northwest shelf (García-Medina et al., 2013). Refraction and shoaling are modeled using backwards ray-tracing techniques (Longuet-Higgins, 1957; Dorrestein, 1960). Ray trajectories, traced backwards from each buoy site into deep water, are used to create transfer coefficients, $K^2(i, f, \theta)$, relating nearshore wave conditions to the offshore spectrum. Backwards traced rays that terminate at islands indicate sheltered directions. Ignoring energy travel time lags, from linear theory and geometric optics (Dorrestein, 1960), the transfer function, K^2, is

$$K^2(i, f, \theta^{(o)}) = \frac{E^{(n)}(f, \theta)}{E^{(o)}(f, \theta)} = \frac{c_g^{(o)}(f)}{c_g^{(n)}(f)} \left| \frac{\Delta\theta^{(n)}}{\Delta\theta^{(o)}} \right| , \tag{3.2}$$

where c_g is the linear group velocity, θ are ray directions, and (o) and (n) indicate offshore and nearshore properties respectively. $\Delta\theta$ indicates the change in nearshore or offshore angle for two adjacent rays.

At the partially sheltered buoy D8, the relationship between $\theta^{(o)}$ and $\theta^{(n)}$ is complicated (Fig. 3.2a). Owing to refraction over shoals and island topography, waves with the same offshore direction can arrive at several nearshore directions (e.g. when $\theta^{(o)} = 230$, $\theta^{(n)} = 230, 255, 285$). Though $\theta^{(n)}$ versus $\theta^{(o)}$ is not monotonic, careful integration over discrete $\theta^{(o)}$ ranges of (3.2) can yield accurate transfer coefficients (Dorrestein, 1960). At D8, for a fixed frequency, K^2 contains many relatively narrow peaks and valleys (individual grey curves in Fig. 3.2b). Forward model transfer coefficients are generated at fine frequency (0.0005Hz) and directional ($< 1^{o}$) resolutions, and averaged to 0.005 Hz, the buoy observational bandwidth for swell, and 1^{o}, our desired directional resolution. Fine-scale features remaining, often with adjacent peaks and valleys (black in Fig. 3.2b), are blurred by the low order moment-measuring buoys. Similar to energy in (3.2), sheltered buoy directional moments are related to offshore conditions by the forward model with transfer coefficients,

$$\mathbf{K^2}(i,f,\theta^{(o)}) = \frac{c_g^{(o)}(f)}{c_g^{(n)}(f)} \left|\frac{\Delta\theta^{(n)}}{\Delta\theta^{(o)}}\right| \begin{bmatrix} 1 \\ \cos\theta^{(n)} \\ \sin\theta^{(n)} \\ \cos 2\theta^{(n)} \\ \sin 2\theta^{(n)} \end{bmatrix}. \tag{3.3}$$

Hereafter, (o) and (n) notation is dropped and θ now refers only to offshore wave directions. Nearshore buoy moments and offshore wave spectra are related by the forward model,

$$\tilde{\mathbf{y}}(i,f) = \int \mathbf{K}^2(i,f,\theta)E(f,\theta)\,d\theta, \tag{3.4}$$

The forward model is independent at each frequency band and hereafter f is dropped for clarity; it is implied that operations are repeated independently across frequency bands. For a single frequency band, in matrix notation,

$$\tilde{\mathbf{y}} = \tilde{\mathbf{H}}\mathbf{x}, \tag{3.5}$$

Transfer coefficients form the model kernel, $\tilde{\mathbf{H}}$, with rows indicating buoy locations and measured moments, and columns indicating directions. The vector, $\tilde{\mathbf{y}}$, comprises buoy observations at i locations, and the vector, $\mathbf{x}$, is the offshore directional spectrum, $E(\theta)$. Expected forward model error is not treated formally and will be absorbed into data misfit (Section 3.5.2). The model resolution matrix is $\mathrm{res}(\tilde{\mathbf{H}}) = \tilde{\mathbf{H}}^{-\mathbf{g}}\tilde{\mathbf{H}}$, where $\tilde{\mathbf{H}}^{-\mathbf{g}} = \tilde{\mathbf{H}}^{\mathbf{T}}(\tilde{\mathbf{H}}\tilde{\mathbf{H}}^{\mathbf{T}})^{-\mathbf{1}}$, the generalized inverse of the time-invariant version of the forward model (i.e. time lags are neglected). For a perfectly resolved model $\mathrm{res}(\tilde{\mathbf{H}}) = \mathbf{I}$, where $\mathbf{I}$ is the identity matrix. In most practical systems the non-zero off-diagonal elements of $\mathrm{res}(\tilde{\mathbf{H}})$ represent blurring of the true model solution (Parker, 1994) while in a well-resolved system the diagonal values of res($\tilde{\mathbf{H}}$) are near unity. Transfer coefficients for deep water buoy sites D1-8 (Fig. 3.3a), those with the longest records, are used to estimate res($\tilde{\mathbf{H}}$) (Fig. 3.3b). The time-invariant model resolution (the diagonal values) is highly variable at 1-deg resolution, ranging from 0.2 to 0.8, with low values indicating blurring across directional bands. The available buoy array (D1-8) has the highest theoretical resolution between 160-180^o and 240-280^o, and lowest at directions $> 300^o$, as only buoy site D1 is unsheltered to those directions. While this procedure could determine the array with the best theoretical resolution, the important effects of observational uncertainty and forward model error are not captured.

In (3.4) wave energy travel times are neglected, but are as large as 12 hours in the $\sim$ 350km model domain. Time lags, $\tau(\theta)$, are estimated with great circle paths between nearshore prediction site and wave energy front (observed at buoy D1) for each direction (O'Reilly et al., 2016, Fig. B1). Additionally, offshore wave energy is assumed to be homogeneous in the along-crest direction, a valid assumption for frequencies <0.09Hz (Crosby et al., 2016, Appendix A). Including time lags in (3.4) yields

$$\tilde{\mathbf{y}}(i,t) = \int \mathbf{K}^2(i,\theta)E(\theta,t-\tau(\theta))\,d\theta\,. \tag{3.6}$$

Predictions at any given time and nearshore location depend on offshore spectra at many recent times because waves at each frequency arrive from a range of directions (τ depends on θ). The time-dependent forward model is discretized at 1-hour time steps, and similar to (3.5), in matrix notation is

$$\mathbf{Hx} = \mathbf{y}\,. \tag{3.7}$$

where $\mathbf{H}$, the model kernel, contains buoy site transfer coefficients. Rows of $\mathbf{H}$ span nearshore locations, buoy-measured moments, and time-steps, while columns span offshore directions and time steps, lagged appropriately by $\tau(\theta)$. The time-dependent forward model formulation, (3.7), is the same as O'Reilly and Guza (1998), but computational advances allow higher directional (1-deg) and temporal (1-hour) resolution estimates of offshore spectra.

3.4 Inverse Model

The forward model, (3.7), is under-determined and observations are noisy. Solutions are therefore non-unique (Ochoa and Delgado-González, 1990; Parker, 1994). A unique solution is obtained by minimizing the log-likelihood cost function [with notation suggested by Ide et al. (1997)],

$$\mathcal{J} = (\mathbf{Hx}-\mathbf{y})^{\mathbf{T}}\mathbf{R}^{-1}(\mathbf{Hx}-\mathbf{y}) + (\mathbf{x}-\mathbf{x_p})^{\mathbf{T}}\mathbf{B}^{-1}(\mathbf{x}-\mathbf{x_p})\,, \tag{3.8}$$

and requiring non-negative energy,

$$\mathbf{x} \geq 0\,. \tag{3.9}$$

The solution minimizes the squared sum of normalized misfit to observations, $\mathbf{y}$, and the normalized adjustments to model prior, $\mathbf{x_p}$ (Wunsch, 2006; Aster et al., 2013), under the assumption that observation and model prior uncertainty are normally distributed. The first RHS term of (3.8), the data misfit, is weighted by $\mathbf{R}^{-1}$, the data error covariance inverse. $\mathbf{R}$ is known for directional buoy observations (Long, 1980; Borgman et al., 1982); however, off-diagonal data covariance terms are set to zero for simplicity (Appendix B). The conservative approach increases the assumed observational uncertainty, but may bias the least squares solution. The second RHS term of (3.8) is the adjustment to the model prior, where $\mathbf{x_p}$ is WW3 directional spectra predictions from the National Oceanic and Atmospheric Administration's 1979-2009 hindcast reanalysis (Tolman, 2009; Chawla et al., 2013). Complete frequency-directional WW3 spectra at buoy site

D1 are linearly interpolated to our model resolution (1° and 1-hour), and additionally linearly interpolated from their logarithmic frequency resolution to typical buoy swell band resolution (0.005 Hz).

We posit that WW3 makes good predictions of average incoming wave directions because storm locations are well-defined by satellite wind observations that drive global wave models. In contrast, model swell energies and detailed directional properties depend on many modeling approximations, and may have significant error. Therefore, before specifying $\mathbf{x_p}$ with interpolated WW3 predictions, two adjustments are made using energy observed at offshore buoy site D1. First, for each 4-day case study, WW3 predictions are shifted in time to achieve maximum correlation with observed energy at buoy D1 (shifts in case examples are $\leq$ 3-hours). Second, WW3 spectra energy at each f are adjusted to D1 observations.

The prior adjustment in (3.8) is weighted by the prior uncertainty covariance, $\mathbf{B}$, where

$$\mathbf{B} = \mathbf{WCW}, \tag{3.10}$$

constructed by weighting the model uncertainty correlation matrix, $\mathbf{C}$, with the diagonal matrix, $\mathbf{W}$, containing the standard deviations, σ_x, of $\mathbf{x_p}$ uncertainty. Although the uncertainty in WW3 bulk parameters can be estimated by comparison with buoy observations, e.g. RMSE of WW3 offshore mean direction (θ_m) in the SCB is $\sim 10^{\circ}$ for swell-band waves (Crosby et al., 2016), the details of $\mathbf{x_p}$ uncertainty are unknown.

The hypothesis that WW3 makes good predictions of peak wave directions is implemented by specifying the variance of $\mathbf{x_p}$ uncertainty, $\sigma_x(\theta)$, with the convolution,

$$\sigma_x(\theta) = \alpha \int B(\theta') x_p(\theta - \theta')\, d\theta', \tag{3.11}$$

where α, is a constant $O(1)$, and $B(\theta')$ is a boxcar,

$$B(\theta') = \begin{cases} 1/2L_B & \text{if} \quad |\theta'| < L_B \\ 0 & \text{otherwise} \end{cases} . \tag{3.12}$$

In the limit $L_B = 1^o$ (the model resolution), the uncertainty simply scales with the predicted energy level. However, with $L_B > 1$ the convolution in (3.11) allows uncertainty in the peak direction. Values of $\alpha = 0.5$ and $L_B = 25^o$ produced plausible uncertainties, e.g. see the grey-shading around the dot-dashed spectrum in Fig. 3.4.

Model smoothness is specified in the model uncertainty correlation matrix **C**, by a Gaussian decay function,

$$C(\Delta\theta, \Delta t) = \exp\left[-\left(\frac{\Delta\theta}{L_\theta}\right)^2 - \left(\frac{\Delta t}{L_t}\right)^2\right] . \tag{3.13}$$

The decay constants L_θ and L_t define model smoothness scales in direction and time respectively, and likely vary by frequency and storm location (e.g. distant storms versus local seas); however, GWM predictions may provide a plausible initial guess. Decorrelation length scales, estimated from WW3 predictions [best-fit to the Gaussian decay function (Eq. 3.13)], range from 10-30 hours and 16-20^o with some dependence on frequency band (Fig. 3.5), but weak cross correlation between direction and time (not shown). Ultimately, weak sensitivity to decay constants was observed in our case examples (Sections 3.5.2, 3.6.2).

C is challenging to invert because it is not diagonal, is often poorly conditioned, and is large (O 10^4 x 10^4) for a 4-day time span at 1-hour and 1-deg resolution). The number of model parameters is reduced by transforming to a truncated orthogonal eigenvalue space. Though not computationally trivial, the decomposition of **C** is performed only once for each set of needed L_θ, L_t as $\mathbf{B}$ scales linearly with $\mathbf{W}$. Alternatively, computation demands are significantly reduced by decomposing $\mathbf{C}$ in time and direction independently ($\mathbf{C}$ is separable in these dimensions), and would allow additional dimensions to be added to the methodology, e.g. frequency, advantageously allowing additional smoothness constraints. In either case the methodology remains the same: before truncation, the decomposition of $\mathbf{C}$ yields

$$\mathbf{C} = \mathbf{V}\mathbf{D}\mathbf{V}^\mathbf{T}, \tag{3.14}$$

where the diagonal matrix $\mathbf{D}$ contains eigenvalues, and $\mathbf{V}$ the orthogonal eigenvectors. The model covariance matrix is now

$$\mathbf{B} = \mathbf{W}\mathbf{V}\mathbf{D}\mathbf{V}^\mathbf{T}\mathbf{W}, \tag{3.15}$$

with formal inverse,

$$\mathbf{B}^{-\mathbf{1}} = \mathbf{W}^{-\mathbf{1}}\mathbf{V}\mathbf{D}^{-\mathbf{1}}\mathbf{V}^\mathbf{T}\mathbf{W}^{-\mathbf{1}}, \tag{3.16}$$

where only diagonal matrices need be inverted. Truncation of eigenvalues smaller than 10^{-3} of the largest eigenvalue produced stable solutions nearly identical to those without truncation. For $L_\theta > 25^\mathrm{o}$ and $L_t >$ 6-hours, truncation after the highest 500 eigenvalues satisfied our criterion, and those matrices are denoted with the subscript $\mathbf{k}$, where

$$\mathbf{B}^{-\mathbf{1}}{}_\mathbf{k} = \mathbf{W}^{-\mathbf{1}}\mathbf{V}_\mathbf{k}\mathbf{D}_\mathbf{k}^{-\mathbf{1}}\mathbf{V}_\mathbf{k}^\mathbf{T}\mathbf{W}^{-\mathbf{1}}, \tag{3.17}$$

The truncated model, $\mathbf{x_k}$, is related to the original by

$$\mathbf{x_k} = \mathbf{V}_\mathbf{k}^\mathbf{T}\mathbf{W}^{-\mathbf{1}}\mathbf{x} \quad \text{and} \quad \mathbf{x} = \mathbf{W}\mathbf{V}_\mathbf{k}\mathbf{x_k}. \tag{3.18}$$

The truncated model kernel is similarly

$$\mathbf{H_k} = \mathbf{HWV_k}\,. \tag{3.19}$$

The cost function, rewritten as

$$\mathcal{J} = (\mathbf{H_k x_k} - \mathbf{y})^{\mathbf{T}}\mathbf{R}^{-\mathbf{1}}(\mathbf{H_k x_k} - \mathbf{y}) + (\mathbf{x_k} - \mathbf{x_{pk}})^{\mathbf{T}}\mathbf{D_k^{-1}}(\mathbf{x_k} - \mathbf{x_{pk}})\,, \tag{3.20}$$

with the altered non-negativity constraint,

$$\mathbf{WV_k x_k} \geq 0\,. \tag{3.21}$$

can be solved rapidly with quadratic programming minimization techniques (MATLAB 2016a Optimization Toolbox) in the equivalent form (Aster et al., 2013),

$$\text{Minimize} \quad \left|\left| \begin{bmatrix} \mathbf{R}^{-1/2}\mathbf{H_k} \\ \mathbf{D_k^{-1/2}} \end{bmatrix} \mathbf{x_k} - \begin{bmatrix} \mathbf{R}^{-1/2}\mathbf{y} \\ \mathbf{D_k^{-1/2}x_{pk}} \end{bmatrix} \right|\right|^2 . \tag{3.22}$$

The numerical solution to (3.22) without the non-negativity constraint in (3.21) was tested and differs negligibly from the analytical solution to the unconstrained minimization (Wunsch 2006),

$$\mathbf{x}^* = \mathbf{BH^T}(\mathbf{HBH^T} + \mathbf{R})^{-\mathbf{1}}\mathbf{y}, \tag{3.23}$$

confirming the numerics.

The minimum solution to (3.20) with (3.21) was slightly negatively biased at the offshore buoy site D1 because event peak energies are consistently under-predicted [owing to the smoothness constraint and proportionality of observed energy uncertainty to itself (Appendix B)]. The bias is corrected with the additional constraint that the event-averaged offshore inverse and observed energy (D1) match. This constraint is applied only at offshore site D1, as forward model errors and observational uncertainty make it problematic to satisfy at all buoy locations.

3.5 Case studies

3.5.1 Synthetic input

A synthetic case study of the time-invariant forward problem (for simplicity) demonstrates that the minimum solution to (3.20) with (3.21) behaves as expected, given the forward model assumptions (e.g. linear wave propagation, along-crest homogeneity, and no wave reflection) are satisfied. A plausible offshore directional spectrum (inspired by WW3 predictions) is used to represent the true offshore energy distribution for an example frequency band, 0.06Hz (solid-black in Fig. 3.4a). The forward model, $\tilde{\mathbf{H}}$, is created with the set of transfer coefficients at synthetic buoy site using backwards ray-tracing. Synthetic buoy observations are generated with the forward model and the true offshore spectrum, and perturbed randomly by the expected observational uncertainty for a 3-hour buoy record at 0.005Hz frequency resolution (Appendix B). Additionally, the model prior, $\mathbf{x_p}$, is generated by shifting the true directional distribution (dashed-dot in Fig. 3.4a). The model covariance is estimated with $L_\theta = 25^o$, $L_B = 25^o$, and $\alpha = 0.5$, and decomposed into an orthogonal eigenvalue space and truncated. Estimated offshore spectra, minimizing (3.20) with (3.21), are found using various combinations of synthetic buoy observations (and corresponding forward models), specifically 1-buoy: D1; 2- buoy: D1, D5; 3-buoy: D1, D5, D6 and 4-buoy: D1, D5, D6, D8 (colored lines in Fig. 3.4a). As additional buoy observations are assimilated, solutions become increasingly similar to the true spectrum (despite relatively large directional error in $\mathbf{x_p}$) and prediction errors in energy and mean direction, θ_m, decrease compared to $\mathbf{x_p}$ predictions at non-assimilated (validation) synthetic buoy sites (D2, D3, D4, D7, S2, S6) (Fig. 3.4b).

3.5.2 Real data input

Case studies with real buoy observations demonstrate the assimilation method's skill in practice, where forward model assumptions are necessarily violated to some extent. Six moderate to large NW wave events were selected (Table 3.2), and various combinations of buoys were used in the assimilation. For simplicity, the additionally available offshore buoy observations near San Nicolas Island and offshore of Pt. Loma, used to drive CDIP's operational wave predictions (O'Reilly et al., 2016), are not included. For each wave event, offshore conditions were found that minimize (3.20) with (3.21) using varying sets of regional buoy observations and adjusted WW3 predictions at buoy site D1. Each 4-day period, bracketing the event, was analyzed at 1-hour and 1-deg resolutions. The first and last 12-hours are discarded as the solution to (3.20) cannot consider lagged observations outside of the 4-day period (travel time lags are $\leq$ 12-hours). For each wave event, offshore conditions were found that minimize (3.20) with (3.21) using varying sets of regional buoy observations and adjusted WW3 predictions at buoy D1. Hereafter spectra generated from minimization of (3.20) and predictions from those spectra are denoted by INV.

Tests with $L_\theta = 25^o$, $L_t =$ 6-hour, $L_B = 25^o$, and $\alpha = 0.5$ and all available buoy observations generated plausibly smooth offshore spectra, similar to the model prior, but with modest adjustments. For example, the INV spectrum at peak frequency in case #4 (Fig. 3.6c) is similar to the adjusted WW3 spectrum (Fig. 3.6b), but with more directional asymmetry, increased temporal smoothness, and some additional features. The misfit between INV energy predictions and buoy observations used in the minimization are are generally small (right panels of Fig. 3.6). A notable exception is buoy site D2, where peak observed wave energy is more than twice that predicted by INV and WW3.

INV spectra with $L_t = 6$hr, $L_\theta = 25^o$, $\alpha = 0.5$, $L_B = 25^o$, and all available buoy observations [availability varies with case study (Table 3.2)] are generated for all cases at all swell-band frequencies. Frequency-integrated and time-averaged observed and INV predicted energies (Fig. 3.7) show good agreement in many cases, but highlight a particularly severe bias (misfits up to 3 standard deviations) at buoys D2 and D3, both located in the eastern half of the Santa Barbara Channel (Fig. 3.1). These deep water buoys are highly sheltered from NW swell by Pt. Conception, and we hypothesize forward model errors are large. Relaxation of smoothness constraints, e.g. $L_\theta = 10^{\mathrm{o}}$ and $L_t = 3$-hours, improved fits negligibly (not shown), and suggest that no plausibly smooth spectrum exists that can fit all observations within their uncertainty. Santa Barbara Channel nearshore buoys S1 and S2 are also biased low (Fig. 3.7) and the persistent negative bias in the region suggests that additional energy may be directed into the Santa Barbara Channel by diffraction around Pt. Conception, reflection off the Channel islands, or refraction by surface currents. Additionally, previous studies suggest waves in the SBC are difficult to model accurately (Rogers et al., 2007; O'Reilly et al., 2016; Crosby et al., 2016). Buoy S4, located just offshore Huntington Beach, is also poorly fit in case #2, but more cases are needed to determine if there is systematic forward model error at this site.

3.6 Discussion

3.6.1 Assimilation method skill

Nearshore prediction skill is improved by corrections to the offshore boundary condition and forward model. Here, only boundary condition corrections are considered. Assimilating observations at sites with significant forward model error can reduce overall model skill, and therefore buoys D2 and D3 are excluded from the following analysis.

The skill of INV solutions with selected assimilated sites (D1, D5, D6, D8) is assessed with comparisons of predictions and observations at non-assimilated (validation) buoy locations. By design, improvement is expected at assimilated buoy sites (Fig. 3.6), however, skill improvement at validation sites suggest that the INV offshore spectrum is increasingly accurate, and prediction skill improvement is region-wide. For all cases, assimilation improves skill for swell-band integrated bulk wave parameters, H_s and θ_m (Table 3.2). Both H_s and θ_m RMSE is reduced by 20-50% relative to WW3 when buoys sites D1, D5, D6, and D8 are assimilated. Assimilated model skill is also higher than predictions made with observations at D1 and the Maximum Entropy Method (MEM, Lygre and Krogstad, 1986), a commonly used technique to estimate directional spectra from buoy directional moments. MEM is currently used in CDIP's operational wave, but with an heuristic blend of multiple offshore buoy observations (O'Reilly et al., 2016). Overall INV predictions are most highly skilled, followed by MEM and WW3 predictions respectively.

3.6.2 Model prior, B

The model prior and model covariance uncertainty select a solution from a theoretically infinite set by imposing desired characteristics, e.g. smoothness or similarity to a preferred model. Smoothness is set by the model correlation matrix, **C**, parameterized by a Gaussian decay function, (3.13), with two adjustable parameters, L_θ and L_t. WW3 spectra predictions suggest that decorrelation length scales in time and direction increase slightly with frequency and range from 10-28 hours and 16-21^o (Fig. 3.5). The trend in temporal decorrelation scale may appear counter-intuitive as low frequency energy from distant storms may persist for days, whereas local-generated seas varies over hours. However, owing to the dispersion of low-frequency energy over long travel distances, energy at very low frequency (e.g. 0.05hz) decorrelates more quickly than high frequencies (e.g. 0.09 Hz).

Model solutions were generally insensitive to prior assumptions. INV spectra skill at validation sites was insensitive to the following parameter ranges: $10^{\mathrm{o}} \leq L_\theta \leq 40^{\mathrm{o}}$, 3-hour $\leq L_t \leq$ 18-hour, $0.25 \leq \alpha \leq 1$, and $25^{\mathrm{o}} \leq L_B \leq 50^{\mathrm{o}}$. Ultimately $L_\theta = 25^o$ was chosen because it yielded slightly higher prediction skill; $L_t = 6$-hour because it agreed well with time scales in regional buoy observations; and $L_B = 25^o$ and $\alpha = 0.5$ because the specified model prior uncertainty appeared plausible (e.g. Fig. 3.4). Variable parameter values were also considered; L_θ was set on a event-by-event, frequency-by-frequency basis, to the directional decorrelation of WW3 predictions, however, resulting INV skill changed negligibly. Though optimal parameter values vary by frequency and event, the insensitivity suggests small adjustments are unnecessary.

The model prior uncertainty, σ_x, controls the influence of WW3 predictions in the INV solution. Previous studies, with an effectively constant σ_x, were plagued with spurious directional peaks from unlikely directions (Long and Hasselmann, 1979; Crosby et al., 2016). The present σ_x parameterization, (3.11), harshly penalizes energy far from peak energy in WW3 predictions (note the lack of spurious energy in Fig. 3.6c). Improved estimates of σ_x would undoubtedly help constrain offshore wave conditions in regional assimilations, but require a high-resolution ground truth.

The assumption of Gaussian statistics throughout the inversion framework makes the search for a solution within a large model space computationally feasible. Although buoy measured moments, (3.1), are χ^2 distributed, for the present high degrees of freedom (196 given 3-hour 0.005Hz data, see Appendix B) the χ^2 distribution is well approximated as Gaussian. Gaussian uncertainty is formally inconsistent with the non-negativity on the INV solutions (e.g. grey shading of uncertainty in Fig. 3.4). However, the effect is likely small because solutions without the non-negativity constraint in, (3.23), contained relatively small amounts of negative energy ($\sim 10\%$)

3.6.3 Implications for buoy array design

An optimal buoy array provides accurate nearshore predictions at acceptable cost. Buoy costs depend on ease of servicing, mooring depth, exposure to shipping and fishing, and other factors. Buoy benefits include improvement in skill locally and in regional models. Offshore buoys are of primary importance, providing unsheltered, deep water, observations free from forward model errors, and several hours before waves arrive at the coast. Energy travel time lags in the SCB vary with wave direction, and both a southerly located buoy (e.g. Pt. Loma) and northerly located buoy (e.g. Harvest) are needed to provide nowcast and short-term forecast predictions (O'Reilly et al., 2016). In smaller regions one offshore buoy may be sufficient. Nearshore buoy locations have historically been determined by funding sources and local community needs, however, assimilation methods provide estimates of the overall added predictive skill and may help assess optimal buoy placement.

Our case studies are not comprehensive, but initial analysis suggests that assimilation of nearshore buoy D8 yields the largest improvement in overall swell prediction (mainly H_s), given that offshore buoy D1 is included (Fig. 3.8a). Both H_s and θ_m RMSE are reduced at validation sites as additional buoy observations are assimilated (Fig. 3.8a), and these incremental improvements help quantify the value of each additionally buoy. Here, H_s RMSE reduction is negligibly small after buoys D1 and D8 are assimilated, and θ_m RMSE reduction is negligible after D1 is assimilated.

Accurate unbiased directional buoy observations have historically been difficult and expensive to acquire. Some buoy directional moments contained bias [e.g. the National Buoy Data Center 3-m discus, (O'Reilly et al., 1996)]. More recently inexpensive GPS sensors have been shown to yield accurate energy spectra and 2nd order directional moments, but poorly resolve vertical motions resulting in biased 1st order directional moments (Herbers et al., 2012). While the high value of accurate offshore directional moments for regional swell prediction is clear (O'Reilly et al., 2016; Crosby et al., 2016), our analysis suggests less value for nearshore directional information. RMSE errors for INV predictions generated with and without assimilation of nearshore directional buoy observations are similar (Fig. 3.8a). Note that directional observations from offshore buoy D1 are included in both inversions. Regional skill is most efficiently improved improved by D1 energy and directional observations, and D8 energy observations. The negligible improvement in regional skill by nearshore directional information may be attributed to (1) the lack of shoreline reflection in the forward model (shoreline incident energy is assumed to completely dissipate) that affects directional observations significantly more than energy (Herbers et al., 1999; Crosby et al., 2016); and/or (2) in increasingly sheltered regions directional observations become nearly redundant to energy observations because waves arrive from a single known direction. The only useful information is the magnitude and timing of arriving energy, the arrival direction is already known. Although adding relatively little to regional swell prediction (given the non-reflective, linear forward model), directional nearshore observations may provide useful local wave information, e.g. providing robust estimates of local radiation stress (Longuet-Higgins and Stewart, 1964).

Theoretically, additional buoy observations add the most skill when their offshore transfer functions (Fig. 3.3) are most unique, providing additional constraints on the offshore spectrum. The mean array resolution (Fig. 3.8b) is estimated by averaging the res($\tilde{\mathbf{H}}$) diagonal weighted by the 2000-2009 WW3 offshore spectra climatology (resolving power is needed most at the most common arrival directions). Perhaps fortuitously, the mean resolution indicates the largest theoretical improvement from buoy D8 given D1, the same result observed in the case studies with real observations. This analysis focuses on existing buoy sites, applicable to identifying redundant observations and regions of significant forward model error. If the forward model is trusted, ideal buoy sites could be determined by the added theoretical resolution, similar to analysis by O'Reilly and McGehee (1994). However, the forward model fails in some locations (e.g. east end of SBC). Short-term buoy deployment (e.g. 1-2 years) at selected sites could test the existing forward model, identifying well-predicted regions, those where the model fails, and sites that add the most value to swell prediction region-wide. This application of our inverse methods is preliminary; the incorporation of multiple offshore buoy sites, the addition of shoreline reflection (Ardhuin and Roland, 2012), and the comprehensive analysis of additional observations are needed.

3.7 Summary

Here, we developed methods to assimilate nearshore directional wave buoy observations of frequency spectra and offshore global wave model (GWM) predictions of frequency-directional spectra. Assimilation yields accurate, high-resolution (direction and time) offshore wave spectra used to produce accurate high-resolution (space and time) coastal wave predictions. Methods use linear (shoaling and refraction) wave propagation assumptions, valid on narrow continental shelves, e.g. the US West Coast, at swell-band frequencies (0.04-0.09 Hz). The linear wave energy propagation model, generated with backwards ray-tracing techniques, requires minimal computation and enables relatively rapid assimilation (compared to 4DVAR techniques). Regional prediction skill improvements are relatively insensitive to user-determined constraints. Nearshore buoy observations poorly fit by assimilated offshore spectra identify sites where forward model error is likely, i.e. significant wave physics are missing from the linear model. Overall improvements to regional swell prediction skill from assimilation are modest, and increments become insignificant after 2-3 buoys are assimilated. Varying the buoy observations included in the assimilation provides insight into optimal array design for regional swell prediction. The Bayesian framework of the assimilation advantageously incorporates prior information easily, e.g. offshore GWM spectra predictions. Future improvements to GWM predictions, and an improved understanding of their uncertainty, will ultimately improve regional prediction skill. Though methods are restricted to regions and frequencies where wave propagation is approximately linear, these computationally rapid methods could be incorporated into a larger assimilation scheme, providing estimates for low-frequency energy and/or a first-guess for more sophisticated non-linear techniques.

3.8 Acknowledgements

Chapter 3, in full, is a reprint with some additions and modifications of the paper, ”Assimilating global wave model predictions and deep water wave observations in nearshore swell predictions” that is currently under review by the Journal of Atmospheric and Oceanic Technology. Authors include by S. C. Crosby, B. D. Cornuelle, W. C. O’Reilly, and R. T. Guza. The dissertation/thesis author was the primary investigator and author of this paper.

This study was funded by the California Department of Parks and Recreation, Division of Boating and Waterways Oceanography Program, the United States Army Corps of Engineers, and the California Sea Grant Traineeship Program. Buoy data was obtained from the Coastal Data Information Program (CDIP, http://cdip.ucsd.edu/). C. B. Olfe (CDIP) helped with model and data access.

Table 3.1: Deep and shallow water buoys site CDIP (Coastal Data Information Program) and NOAA (National Oceanic and Atmospheric Administration) identification numbers.

ID	CDIP ID	NOAA ID	Name	Depth [m]
Deep Water				
D1	071	46218	Harvest	550
D2	107	46216	Goleta	182
D3	111	46217	Anacapa	114
D4	028	46221	Santa Monica	363
D5	092	46222	San Pedro	457
D6	096	46223	Dana Point	373
D7	045	46224	Oceanside	220
D8	100	46225	Torrey Pines	550
D9	093	46231	Mission Bay	201
D10	095	46226	Pt La Jolla	181
Shallow Water				
S1	131	-	Rincon Point	20
S2	141	46234	Port Hueneme	20
S3	118	-	Leo Carillo	20
S4	172	46230	Huntington Beach Nearshore	20
S5	043	46242	Camp Pendleton	20
S6	155	46235	Imperial Beach	20

Table 3.2: Mean RMSE of H_s and θ_m at validation buoy sites for each case study with WW3, INV, and MEM boundary conditions. INV solutions estimated with buoys D1, D5, D6, D8 included in the inversion.

			Peak	Peak	RMSE - H_s[m]			RMSE - $\theta_m[^o]$		
Case #	Dates	Validation sites	H_s [m]	Freq [Hz]	WW3	INV	MEM	WW3	INV	MEM
1	Jan. 11-15, 2004	D4 D7 D10 S3	3.0	0.06	0.27	0.13	0.18	6.5	3.0	4.3
2	Dec. 20-24, 2005	D4 D7 S1 S4	4.9	0.06	0.36	0.21	0.27	7.6	5.9	7.5
3	Dec. 26-30, 2006	D4 D7 D9 S1 S6	7.0	0.07	0.29	0.23	0.43	5.4	5.3	9.7
4	Jan. 11-15, 2008	D4 D7 D9 S2 S6	3.1	0.06	0.24	0.19	0.28	7.4	3.9	5.9
5	Feb. 9-13, 2008	D4 D7 D9 S2 S6	3.2	0.05	0.19	0.13	0.17	12.3	4.6	8.0
6	Nov. 12-16, 2008	D4 D7 D9 S5 S6	2.2	0.08	0.32	0.21	0.30	7.4	5.7	10.0

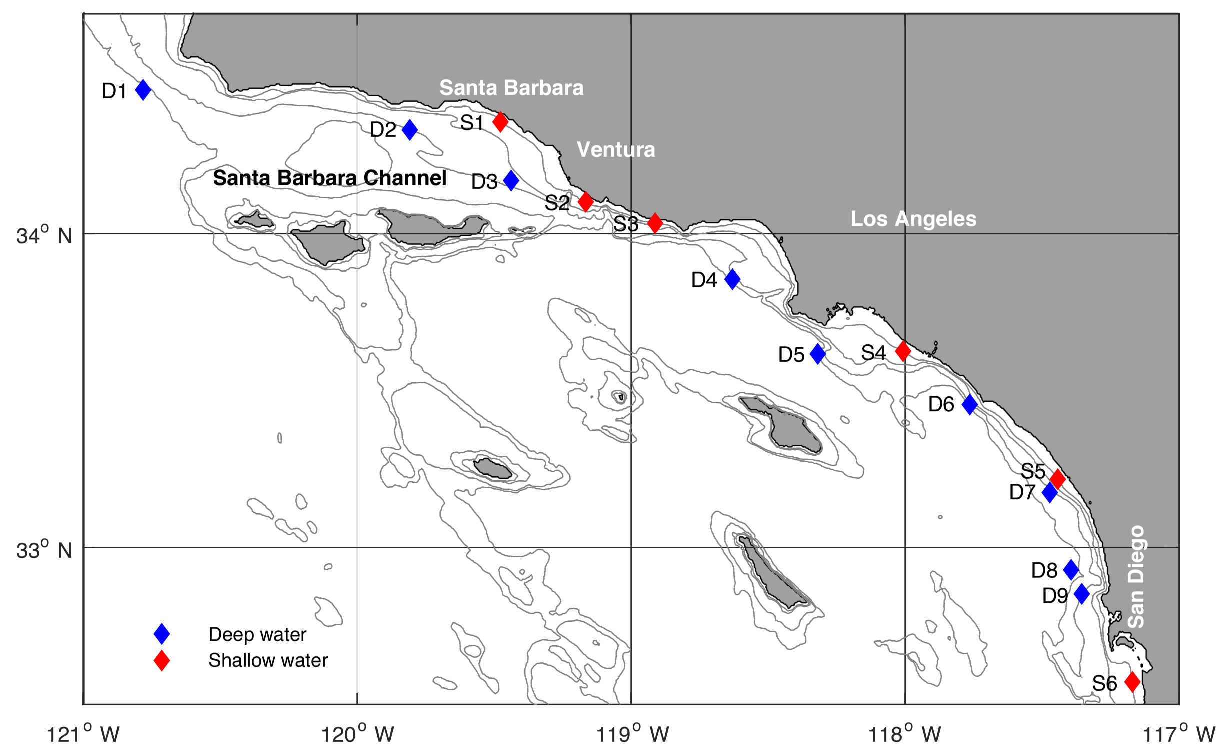

Figure 3.1: Southern California Bight (SBC) mooring locations of deep (D) and shallow (S) water CDIP wave buoys. Grey contours show 20m, 50m, 200m, and 500m isobaths

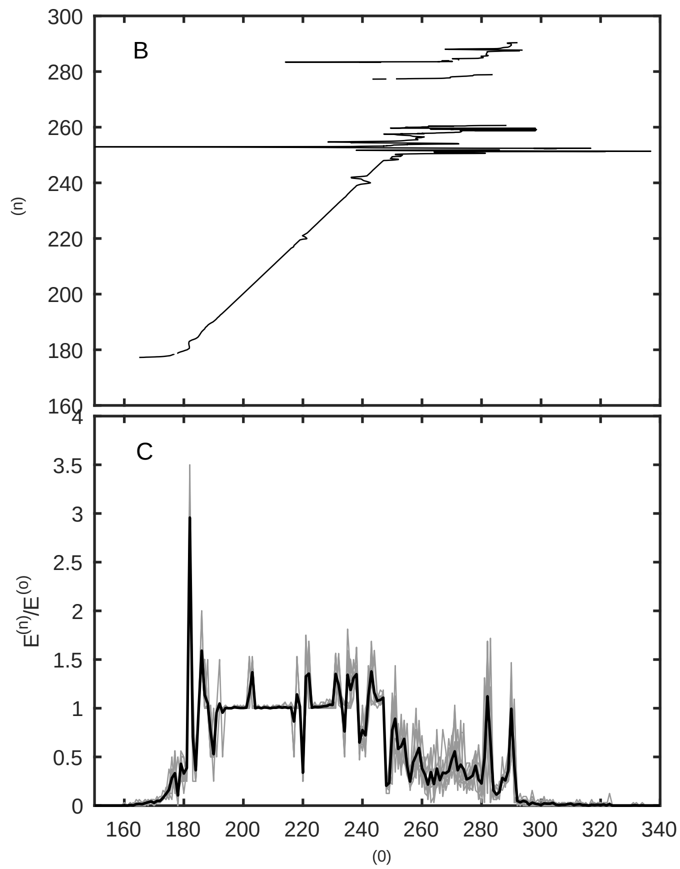

Figure 3.2: (a) Nearshore ray angle versus offshore ray angle for rays traced backwards from buoy site D8 traced with 0.07Hz wave energy phase speeds. Integration at 1-deg resolution yields (b) energy transfer coefficients at buoy site D8. Grey estimates are at finely spaced frequencies (0.0675-0.0725Hz at 0.0005Hz spacing) and then averaged to represent each frequency band (black).

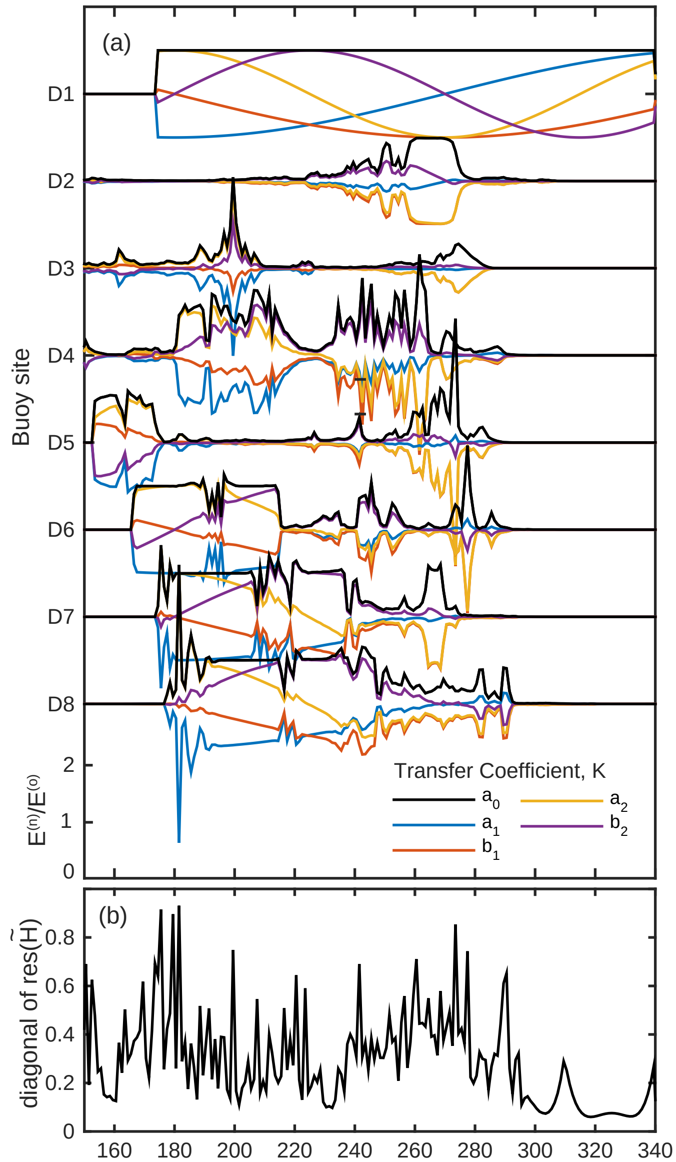

Figure 3.3: (a) Time-invariant transfer coefficient versus offshore direction at deep water SCB buoy sites (labeled) for energy, a_o, (black) and directional moments: a_1 (blue), b_1 (red), a_2 (yellow), and b_2 (purple). (b) Diagonal values of resolution matrix, res($\tilde{\mathbf{H}}$), versus offshore direction.

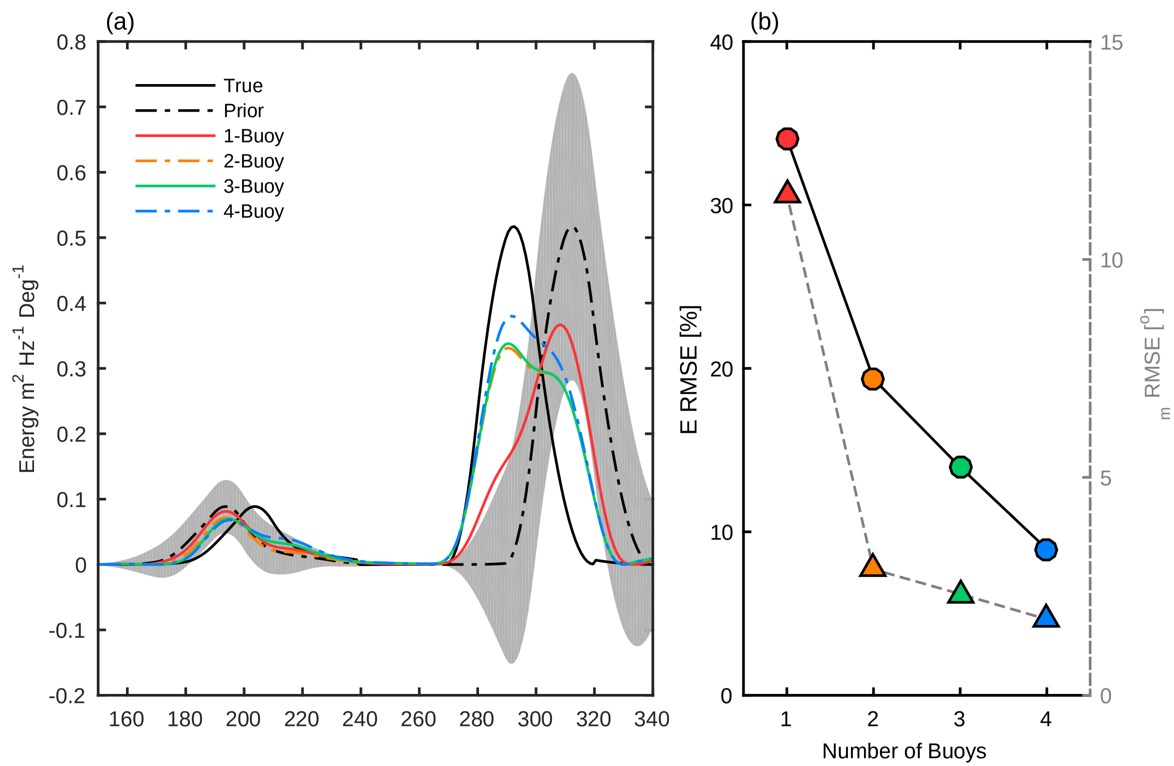

Figure 3.4: A synthetic example of the assimilation technique: (a) Energy versus direction at 0.06Hz for plausible bi-modal wave conditions. Synthetic observations are created with true spectra (black) run through the time-invariant forward model (Eq. 3.5) and perturbed by expected uncertainty in a 3-hour record (Appendix B). Model prior (dot-dashed) and associated 1σ uncertainty (grey-shading) is used with various combinations of synthetic buoys observations (1-buoy: D1; 2-buoy: D1, D5; 3-buoy: D1, D5, D6 and 4-buoy: D1, D5, D6, D8) to solve for the offshore spectra (colored lines). (b) Prediction errors at validation sites (D2, D3, D4, D7, S2, S6) for offshore spectra estimates versus the number of buoys included in the estimate [colors correspond to spectra in (a)]. Solid-black line with circles show %-energy RMSE and dashed-grey line with triangles show θ_m RMSE in degrees.

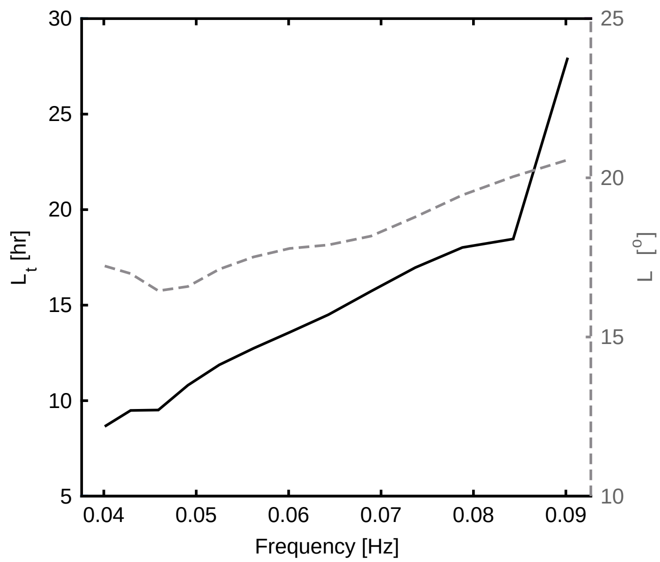

Figure 3.5: WW3 time (solid, left-axis) and direction (dashed, right-axis) decorrelation length scales versus frequency. Deccorrelation length scales are determined by best fit to gaussian (Eq. 3.13) of WW3 autocorrelation function.

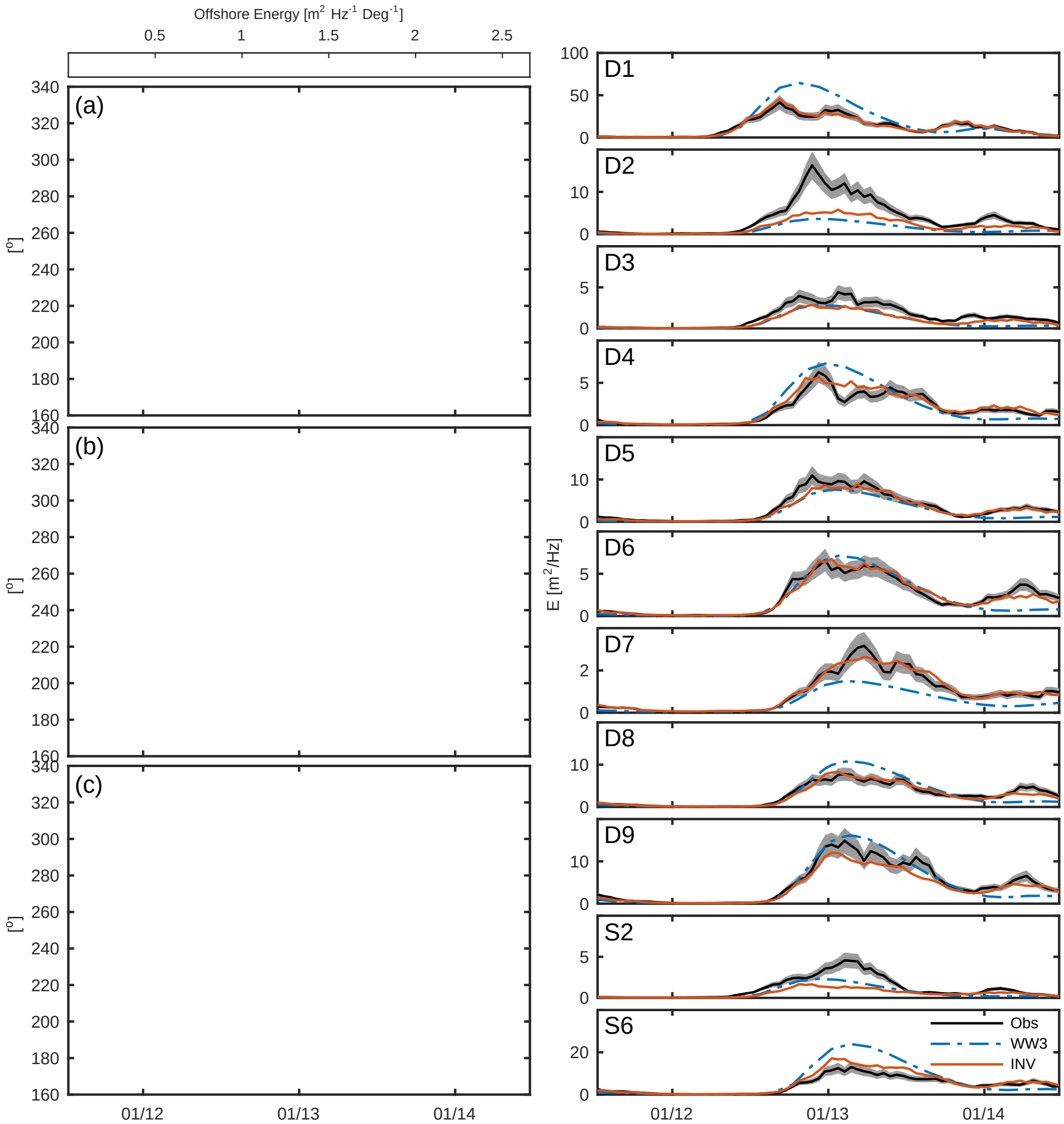

Figure 3.6: Offshore directional spectra (left) and energy observations and predictions at buoy sites (right) at the 0.06Hz swell band frequency for a wave event during January 2008 (Case #4). Grey shading indicates observational uncertainty at 95% confidence. (a) WW3 spectra, (b) WW3 spectra is shifted 1-hour backward in time and adjusted to match total energy observed at buoy D1, (c) INV spectra generated using all buoy observations (left) and adjusted WW3 spectra in the minimization of (3.22) with $L_t = 6$-hours, $L_\theta = 25^o$, $\alpha = 0.5$, and $L_B = 25$. The largest misfits to buoys D2 and S2 are likely owing to forward model errors in the eastern Santa Barbara Channel.

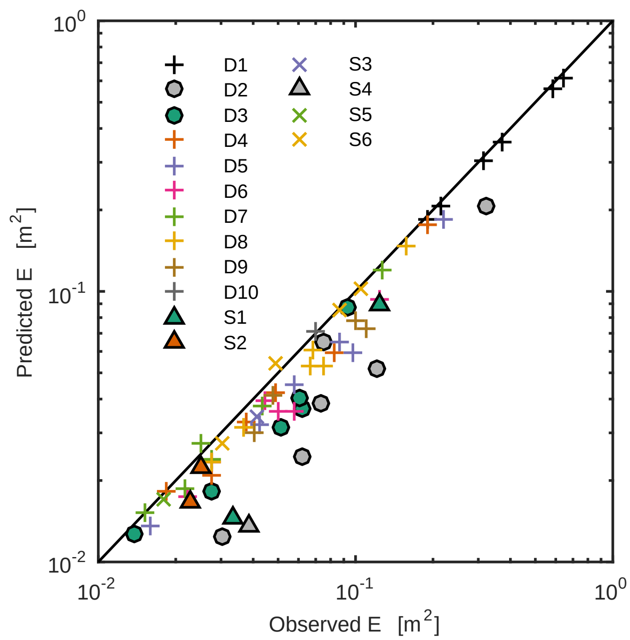

Figure 3.7: Predicted versus observed E, integrated across swell frequency bands and temporally averaged, for each case study. Predictions with INV solutions use all available buoy observations. Some observations are not well fit by the INV methods and indicate forward model errors, e.g. D2, D3, S1, S2, and S4.

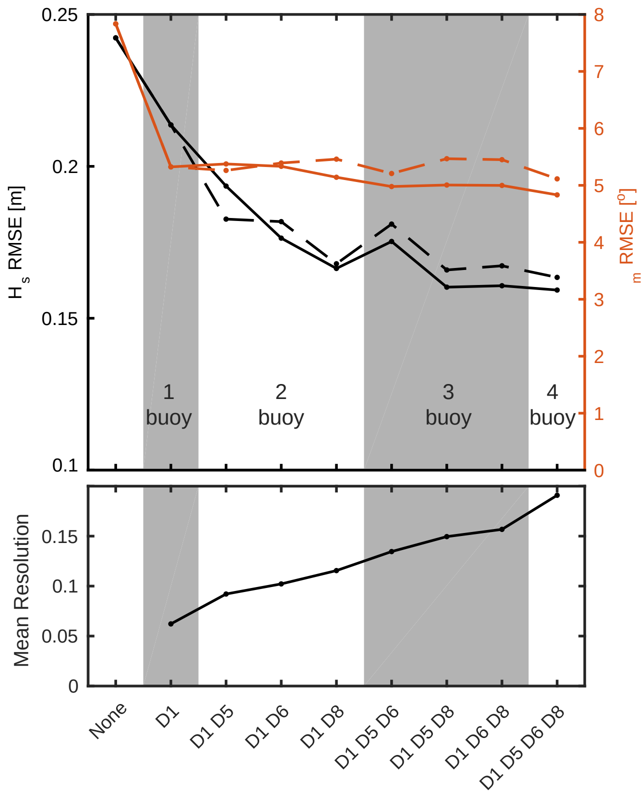

Figure 3.8: (a) H_s (black, left-axis) and θ_m (red, right-axis) RMSE of INV predictions at specified validation sites (Table 3.2) averaged across all cases versus varying combinations of assimilated buoy observations ($L_t = 6$-hours, $L_\theta = 25^o$, $\alpha = 0.5$, and $L_B = 25$). 'None' corresponds to the un-adjusted WW3 prediction, and has the largest errors. Solid lines show assimilation of nearshore buoy observations including directional moments, while dashed lines show assimilation of only nearshore buoy energy observations. Overall error is reduced with additional buoy observations, and assimilation of nearshore directional observations have minimal impact. (b) Mean of the res($\tilde{\mathbf{H}}$) diagonal weighted by the 2000-2009 WW3 offshore spectra climatology for the given buoy array (x-axis).

Appendix A

Linear propagation and along-crest homogeneity

Low frequency energy arriving from distant sources, e.g. high southern and northern latitudes, is along-crest homogeneous on the scale of the SC domain (300km), much less than the travel distance (Fig. A.1). Additionally, at these spatial scales, low frequency energy is assumed to propagate at the theoretical group velocity, c_g, with negligible dissipation, generation, and non-linear energy transfers. Under these assumptions, energy is transformed at each frequency and direction as

$$E(f_i, \theta_j, x_k, t) = K^2(f, \theta)\, E[f_i, \theta_j, x_p, t + \tau(f_i, \theta_j, \Delta x)]\,, \tag{A.1}$$

where the transfer coefficient, K^2, captures the effect of bathymetry induced refraction, shoaling, and island shadowing. The time lag, τ, for each location (x_k), frequency, and direction is

$$\tau(f_i, \theta_j, \Delta x) = \frac{\Delta x \cos\theta_j}{c_g(f_i)}\,, \tag{A.2}$$

and illustrated in Fig. A.1.

Assumptions (A.1) and (A.2) are tested offshore, with no bathymetry effects (i.e. $K^2 = 1$), using complete frequency-direction WW3 predictions, $F_{ww3}(f,\theta)$, that do not make these assumptions. Buoy observations, with inherent directional uncertainty (Section 2.3), are less reliable for this test of assumptions. $F_{ww3}(f,\theta)$ predictions at NOAA buoy site 46042 (Fig. A.2a) are used in (A.1) and (A.2) to predict wave conditions at buoy locations 46028, 46011, 46069, and 46047. These linear predictions are compared with $F_{ww3}(f,\theta)$ predictions at the buoy sites. The predictive skill of the assumptions in (A.1,A.2) is shown in Fig. A.2b using the R^2 metric. Skill declines sharply above 0.09Hz for prediction sites furthest from buoy 46042 (Fig A.2) and was similar for varying wave directions (not shown). The high skill of equations (A.1) and (A.2) confirms the validity of both long-crest homogeneity and linear wave energy propagation assumptions for frequencies < 0.09Hz.

Here, these assumptions are used with transfer coefficients to predict waves nearshore, however, they can be additionally used to parameterize a typical regional wave model boundary with a single point-based observation or GWM prediction. E.g. locations along the thick black line in Fig. A.1, representing a wave model boundary, could be well predicted using equations (A.1) and (A.2) for similar spatial scales (O 100km) at similar frequencies (0.04-0.09Hz).

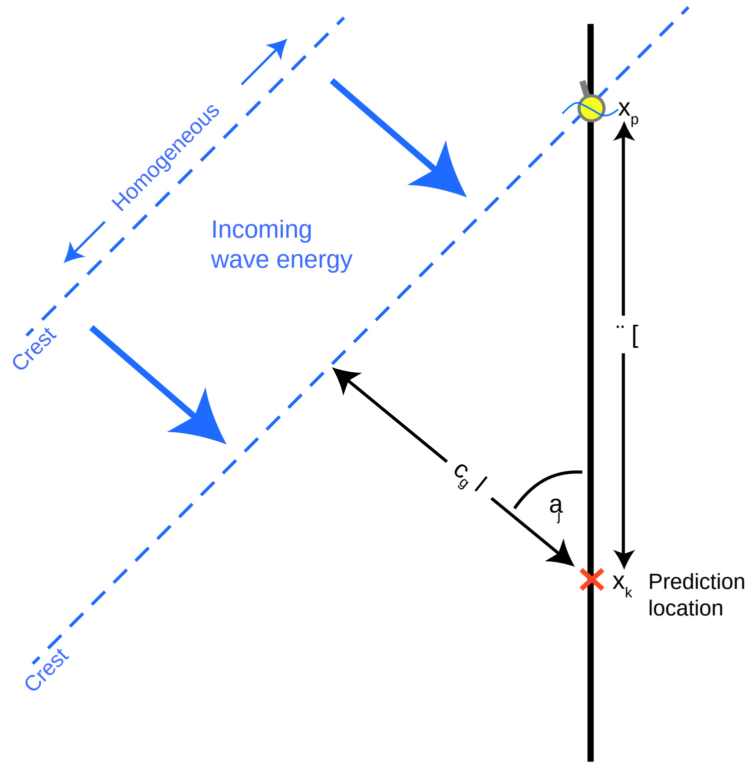

Figure A.1: Schematic of along-crest spatial homogeneity assumption and linear wave propagation at the group velocity, c_g. Wave conditions (buoy observations or GWM predictions) at yellow symbol are used to predict waves at the red x. The time lag, $\tau(f,\theta,\Delta x)$, is used with complete frequency-directional spectra, $E(f,\theta,t)$, to make predictions at location x_k.

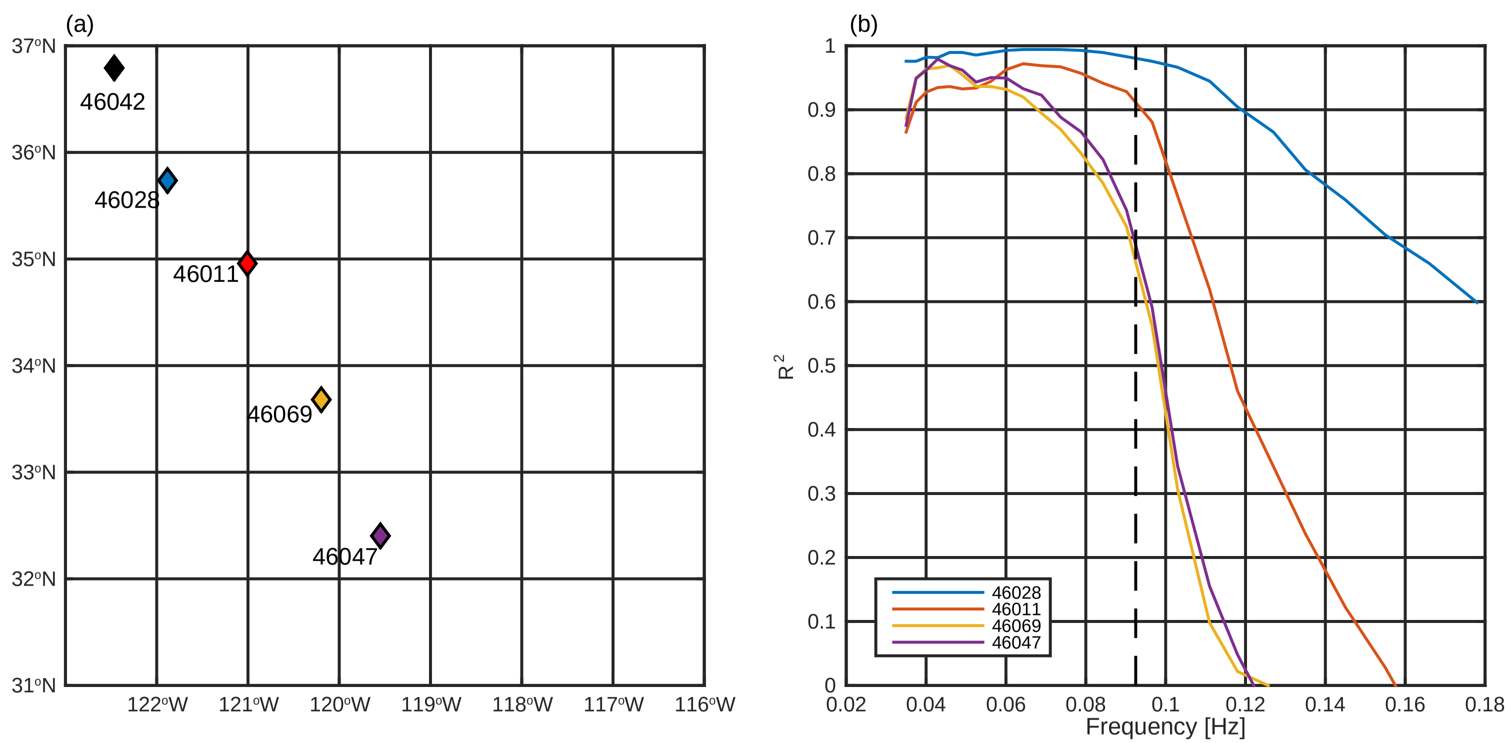

Figure A.2: (a) Map of southern and central California showing locations of $E(f,\theta)$ GWM (NOAA-WW3) predictions for 2000-2007 (NOAA buoy observations are not used here). GWM predictions at northerly buoy 46042 are used, with simple linear propagation and along-crest homogeneity assumptions (Appendix A), to predict swell at the southerly sites. These model predictions are compared with the full frequency-direction GWM predictions at each site. (b) R^2 skill versus frequency at southerly locations (see legend). The high prediction skill for frequencies $\leq$ 0.9Hz (vertical dashed line) is similar for all approach directions (the average is shown), and supports the method of boundary condition specification used here.

Appendix B

Directional buoy observational uncertainty

Directional wave buoys measure vertical (z) and horizontal (x, y) translations or pitch, heave, and roll equivalently, and from these observations constraints on the phase-averaged wave energy spectrum, $E(f, \theta)$, can be obtained. Cross-spectra estimates at each frequency, f, can be related to the first five moments of the directional distribution's Fourier series (Longuet-Higgins 1963)

$$\mathbf{y} = \begin{bmatrix} a_0 \\ a_1 \\ b_1 \\ a_2 \\ b_2 \end{bmatrix} = \begin{bmatrix} S_{zz} \\ Q_{zx}/[S_{zz}(S_{xx}+S_{yy})]^{1/2} \\ Q_{zy}/[S_{zz}(S_{xx}+S_{yy})]^{1/2} \\ (S_{xx}-S_{yy})/(S_{xx}+S_{yy}) \\ 2C_{xy}/(C_{xx}+C_{yy}) \end{bmatrix}, \tag{B.1}$$

and are frequently normalized as shown above to reduce errors from instrument gain (Long, 1980). Here, S, C, Q are power, co, and quad spectra. Low-order moments in $\mathbf{y}$

are related to the directional spectrum at each frequency by

$$\begin{bmatrix} a_0 \\ a_1 \\ b_1 \\ a_2 \\ b_2 \end{bmatrix} = \begin{bmatrix} \int D(\theta)\, d\theta \\ \int D(\theta) \cos\theta\, d\theta \\ \int D(\theta) \sin\theta\, d\theta \\ \int D(\theta) \cos 2\theta\, d\theta \\ \int D(\theta) \sin 2\theta\, d\theta \end{bmatrix}. \tag{B.2}$$

Variance and covariance estimates of $\mathbf{y}$ have been derived (Long, 1980; Borgman et al., 1982) and used in Chapter 2. In Chapter 3 unnormalized moments are used such

$$\tilde{\mathbf{y}} = \begin{bmatrix} S_{zz} \\ Q_{zx} \\ Q_{zy} \\ S_{xx} - S_{yy} \\ 2C_{xy} \end{bmatrix}, \tag{B.3}$$

with variance (Bendat and Piersol, 1971)

$$\mathrm{var}(\tilde{\mathbf{y}}) = \frac{1}{\sqrt{n_d}} \begin{bmatrix} S_{zz}^2 \\ \frac{1}{2}(S_{zz}S_{xx} + Q_{zx}^2) \\ \frac{1}{2}(S_{zz}S_{yy} + Q_{zy}^2) \\ S_{xx}^2 + S_{yy}^2 - \gamma_{xy}^2 S_{xx}S_{yy} \\ 2(S_{xx}S_{yy} + C_{xy}^2) \end{bmatrix}, \tag{B.4}$$

where $2 \times n_d =$ degrees of freedom, and γ is the signal coherence. At 0.005Hz frequency resolution and 3-hour smoothed temporal resolution $n_d = 48$. Onboard Datawell (http://www.datawell.nl/) buoy processing slightly smooths observations across frequency, increasing the degrees of freedom ($n_d = 96$). Note, however, that neighboring frequency-band observations are no longer statistically independent.

Although covariances between buoy moments have been estimated (Long, 1980; Borgman et al., 1982; Bendat and Piersol, 1971), for computational simplicity they are often ignored (O'Reilly and Guza, 1998). The simplification significantly reduces inversion computation time in Chapter 3 by allowing transformation to an orthogonal model space. Advantageously, the rapid transformed inverse methods could be expanded to frequency space, allowing additional smoothness constraints. Assuming independent variance (zero covariance) overestimates observation uncertainty, and may partially compensate for forward model errors (e.g. missing physics in wave propagation).

Bibliography

Adams, P. N., Inman, D. L., and Graham, N. E. (2008). Southern California Deep-Water Wave Climate: Characterization and Application to Coastal Processes. *Journal of Coastal Research*, 244:1022–1035.

Ardhuin, F., O'Reilly, W. C., Herbers, T. H. C., and Jessen, P. F. (2003). Swell Transformation across the Continental Shelf. Part I: Attenuation and Directional Broadening. *Journal of Physical Oceanography*, 33(9):1921–1939.

Ardhuin, F., Rogers, E., Babanin, A. V., Filipot, J.-F., Magne, R., Roland, A., van der Westhuysen, A., Queffeulou, P., Lefevre, J.-M., Aouf, L., and Collard, F. (2010). Semiempirical Dissipation Source Functions for Ocean Waves. Part I: Definition, Calibration, and Validation. *Journal of Physical Oceanography*, 40(9):1917–1941.

Ardhuin, F. and Roland, A. (2012). Coastal wave reflection, directional spread, and seismoacoustic noise sources. *Journal of Geophysical Research: Oceans*, 117(C11):n/a–n/a.

Ardhuin, F. and Roland, A. (2013). The Development of Spectral Wave Models: Coastal and Coupled Aspects. In *Coastal Dynamics*, number May, pages 25–38.

Aster, R. C., Borchers, B., and Thurber, C. H. (2013). *Parameter estimation and inverse problems*. Academic Press.

Backus, G. E. and Gilbert, J. F. (1967). Numerical Applications of a Formalism for Geophysical Inverse Problems. *Geophysical Journal of the Royal Astronomical Society*, 13(1-3):247–276.

Beji, S. and Battjes, J. A. (1993). Experimental investigation of wave propagation over a bar. *Coastal Engineering*, 19(1-2):151–162.

Bendat, J. S. and Piersol, A. G. (1971). *Random data : analysis and measurement procedures*. Wiley, New York, 4th edition.

Booij, N., Ris, R. C., and Holthuijsen, L. H. (1999). A third-generation wave model for coastal regions: 1. Model description and validation. *Journal of Geophysical Research*, 104(C4):7649–7666.

Borcea, L., Papanicolaou, G., and Tsogka, C. (2002). Imaging and time reversal in random media. *Inverse Problems*, 18(5):303.

Borgman, L. E., Hagan, R. L., and Kuik, A. J. (1982). Statistical precision of directional spectrum estimation with data from a tilt-and-roll buoy. *Topics in Ocean Physics*, pages 418—-438.

Boyd, S. and Vandenberghe, L. (2004). *Convex optimization*, volume 25. Cambridge University Press.

Camus, P., Mendez, F. J., and Medina, R. (2011). A hybrid efficient method to downscale wave climate to coastal areas. *Coastal Engineering*, 58(9):851–862.

Camus, P., Mendez, F. J., Medina, R., Tomas, A., and Izaguirre, C. (2013). High resolution downscaled ocean waves (DOW) reanalysis in coastal areas. *Coastal Engineering*, 72:56–68.

Cavaleri, L., Alves, J., Ardhuin, F., and Babanin, A. (2007). Wave modellingthe state of the art. *Progress in Oceanography*, 75(4):603–674.

Chawla, A., Spindler, D., and Tolman, H. L. (2011). A thirty year wave hindcast using the latest NCEP Climate Forecast System Reanalysis winds. In *12th Int. Workshop on Wave Hindcasting and Forecasting*, number 70, pages 89–206. U.S. Amry Corps of Engineers.

Chawla, A., Spindler, D. M., and Tolman, H. L. (2013). Validation of a thirty year wave hindcast using the Climate Forecast System Reanalysis winds. *Ocean Modelling*, 70:189–206.

Chawla, A. and Tolman, H. L. (2008). Obstruction grids for spectral wave models. *Ocean Modelling*, 22(1-2):12–25.

Constable, S. C., Parker, R. L., and Constable, C. G. (1987). Occam's inversion: A practical algorithm for generating smooth models from electromagnetic sounding data. *Geophysics*, 52(3):289.

Crosby, S. C., O'Reilly, W. C., Guza, R. T., Crosby, S. C., O'Reilly, W. C., and Guza, R. T. (2016). Modeling Long-Period Swell in Southern California: Practical Boundary Conditions from Buoy Observations and Global Wave Model Predictions. *Journal of Atmospheric and Oceanic Technology*, 33(8):1673–1690.

Dobson, R. S. (1967). Some applications of a digital computer to hydraulic engineering problems.

Dorrestein, R. (1960). Simplified method of determining refraction coefficients for sea waves. *Journal of Geophysical Research*, 65(2):637–642.

Elgar, S. (1987). Bias of Effective Degrees of Freedom of a Spectrum. *Journal of Waterway, Port, Coastal, and Ocean Engineering*, 113(1):77–82.

Elgar, S., Herbers, T. H. C., and Guza, R. T. (1994). Reflection of Ocean Surface Gravity Waves from a Natural Beach.

García-Medina, G., Özkan-Haller, H. T., Ruggiero, P., and Oskamp, J. (2013). An Inner-Shelf Wave Forecasting System for the U.S. Pacific Northwest. *Weather and Forecasting*, 28(3):681–703.

Grant, M. C. and Boyd, S. P. (2013). CVX: Matlab software for dis- ciplined convex programming.

Gull, S. F. and Skilling, J. (1984). Maximum entropy method in image processing. *IEE Proceedings*, 131(6):646–659.

Guza, R. T., Thorton, E., and Christensen Jr, N. (1986). Observations of steady longshore currents in the surf zone. *American Meteorological Society*, 16(11):1959–1969.

Haas, K. A. and Hanes, D. M. (2004). Process Based Modeling of Total Longshore Sediment Transport. *Journal of Coastal Research*, 203:853–861.

Hashimoto, N. and Kobune, K. (1988). Directional spectrum estimation from a Bayesian approach. In *21st Conference on Coastal Engineering*, pages 62–76. B. L. Edge, Ed.

Hasselmann, K., Barnett, T. P., Bouws, E., Carlson, H., Cartwright, D. E., Enke, K., Ewing, J. A., Gienapp, H., Hasselmann, D. E., Kruseman, P., Meerburg, A., Muller, P., Olbers, D. J., Richter, K., Sell, W., and Walden, H. (1973). Measurements of Wind-Wave Growth and Swell Decay during the Joint North Sea Wave Project (JONSWAP). *Ergnzungsheft zur Deutschen Hydrographischen Zeitschrift Reihe*, A(8)(8 0):p.95.

Hasselmann, S., Hasselmann, K., Allender, J. H., and Barnett, T. P. (1985). Computations and Parameterizations of the Nonlinear Energy Transfer in a Gravity-Wave Specturm. Part II: Parameterizations of the Nonlinear Energy Transfer for Application in Wave Models. *Journal of Physical Oceanography*, 15(11):1378–1392.

Hayes, W. D. (1970). Conservation of action and modal wave action. *Proceedings of the Royal Society of* . . . , 320(1541):187–208.

Herbers, T. H. C., Elgar, S., and Guza, R. T. (1999). Directional spreading of waves in the nearshore. *Journal of Geophysical Research: Oceans*, 104(C4):7683–7693.

Herbers, T. H. C. and Guza, R. T. (1990). Estimation of directional wave spectra from multicomponent observations.

Herbers, T. H. C., Jessen, P. F., Janssen, T. T., Colbert, D. B., and MacMahan, J. H. (2012). Observing Ocean Surface Waves with GPS-Tracked Buoys. *Journal of Atmospheric and Oceanic Technology*, 29(7):944–959.

Holthuijsen, L. H., Herman, A., and Booij, N. (2003). Phase-decoupled refraction-diffraction for spectral wave models. *Coastal Engineering*, 49(4):291–305.

Ide, K., Courtier, P., Ghil, M., and Lorenc, A. C. (1997). Unified Notation for Data Assimilation : Operational, Sequential and Variational (gtSpecial IssueltData Assimilation in Meteology and Oceanography: Theory and Practice). *Journal of the Meteorological Society of Japan. Ser. II*, 75(1B):181–189.

Inman, D. and Frautschy, J. (1965). Littoral processes and the development of shorelines. *Coastal Engineering*, pages 511–536.

Kobune, K. and Hashimoto, N. (1986). Estimate of directional spectra from the maximum entropy principle. In *PARI Rep*, pages 123–146. Port and Harbour Research Institute, Ministry of Transport.

Komar, P. and Inman, D. (1970). Longshore sand transport on beaches. *Journal of Geophysical Research*, 75(30):5914–5927.

Kuik, A. J., van Vledder, G. P., Holthuijsen, L. H., Kuik, A. J., van Vledder, G. P., and Holthuijsen, L. H. (1988). A Method for the Routine Analysis of Pitch-and-Roll Buoy Wave Data. *Journal of Physical Oceanography*, 18(7):1020–1034.

Lawson, L. M. and Long, R. B. (1983). 1520-0485%281983%29013-0474%3Ampotsw-2%2E0%2Eco%3B2.pdf.

Long, R. B. (1980). The Statistical Evaluation of Directional Spectrum Estimates Derived from Pitch/Roll Buoy Data. *Journal of Physical Oceanography*, 10(6):944–952.

Long, R. B. and Hasselmann, K. (1979). A Variational Technique for Extracting Directional Spectra from Multi-Component Wave Data. *Journal of Physical Oceanography*, 9(2):373–381.

Longuet-Higgins, M., Cartwright, D., and Smith, N. (1963). Observations of the directional spectrum of sea waves using the motions of a floating buoy. In *Ocean Wave Spectra*, pages 111–136, Easton, Maryland.

Longuet-Higgins, M. and Stewart, R. (1964). Radiation stresses in water waves; a physical discussion, with applications. *Deep Sea Research and Oceanographic Abstracts*, 11(4):529–562.

Longuet-Higgins, M. S. (1957). On the transformation of a continuous spectrum by refraction. *Mathematical Proceedings of the Cambridge Philosophical Society*, 53(01):226.

Lygre, A. and Krogstad, H. E. (1986). Maximum Entropy Estimation of the Directional Distribution in Ocean Wave Spectra. *Journal of Physical Oceanography*, 16(12):2052–2060.

Mehaute, L. B. and Wang, J. (1982). Wave Spectrum Changes on Sloped Beach. *Journal of the Waterway, Port, Coastal and Ocean Division*, 108(1):33–47.

Mínguez, R., Espejo, A., Tomás, A., Méndez, F. J., and Losada, I. J. (2011). Directional calibration of wave reanalysis databases using instrumental data. *Journal of Atmospheric and Oceanic Technology*, 28(11):1466–1485.

Nicholls, R. J. (2010). Impacts of and Responses to Sea-Level Rise. In *Understanding Sea-Level Rise and Variability*, pages 17–51. Wiley-Blackwell, Oxford, UK.

NOAA (2006). Sensitivity of coastal environments and wildlife to spilled oil. Technical report, NOAA/Office of Response and Restoration.

Ochoa, J. and Delgado-González, O. E. (1990). Pitfalls in the estimation of wind wave directional spectra by variational principles. *Applied Ocean Research*, 12(4):180–187.

Oltman-Shay, J. and Guza, R. (1984). A data-adaptive ocean wave directional-spectrum estimator for pitch and roll type measurements. *Journal of physical oceanography*, 14(11):1800–1810.

O'Reilly, W. and Guza, R. (1993). A comparison of two spectral wave models in the Southern California Bight. *Coastal Engineering*, 19(3):263–282.

O'Reilly, W., Olfe, C. B., Thomas, J., Seymour, R., and Guza, R. (2016). The California coastal wave monitoring and prediction system. *Coastal Engineering*, 116:118–132.

O'Reilly, W. C. and Guza, R. T. (1998). Assimilating Coastal Wave Observations in Regional Swell Predictions. Part I: Inverse Methods. *Journal of Physical Oceanography*, 28(4):679–691.

O'Reilly, W. C., Herbers, T. H. C., Seymour, R. J., Guza, R. T., O'Reilly, W. C., Herbers, T. H. C., Seymour, R. J., and Guza, R. T. (1996). A Comparison of Directional Buoy and Fixed Platform Measurements Of Pacific Swell. *Journal of Atmospheric and Oceanic Technology*, 13(1):231–238.

O'Reilly, W. C. and McGehee, D. D. (1994). Design of Regional Wave Monitoring

Networks: A Case Study for the Southern California Bight. Technical report, US Army Corps of Engineers, Vicksburg Mississippi.

Orzech, M. D., Veeramony, J., Ngodock, H., Orzech, M. D., Veeramony, J., and Ngodock, H. (2013). A Variational Assimilation System for Nearshore Wave Modeling. *Journal of Atmospheric and Oceanic Technology*, 30(5):953–970.

Panteleev, G., Yaremchuk, M., and Rogers, W. E. (2015). Adjoint-Free Variational Data Assimilation into a Regional Wave Model. *Journal of Atmospheric and Oceanic Technology*, 32(7):1386–1399.

Parker, R. L. R. L. (1994). *Geophysical inverse theory*. Princeton University Press.

Rascle, N., Ardhuin, F., Queffeulou, P., and Croizé-Fillon, D. (2008). A global wave parameter database for geophysical applications. Part 1: Wave-current-turbulence interaction parameters for the open ocean based on traditional parameterizations. *Ocean Modelling*, 25(3-4):154–171.

Ricciardulli, L. and Wentz, F. (2011). Reprocessed QuikSCAT (V04) wind vectors with Ku-2011 geophysical model function. *Remote Sensing Systems Technical Report*, pages 1–8.

Rogers, W. E., Kaihatu, J. M., Hsu, L., Jensen, R. E., Dykes, J. D., and Holland, K. T. (2007). Forecasting and hindcasting waves with the SWAN model in the Southern California Bight. *Coastal Engineering*, 54(1):1–15.

Snodgrass, F. E., Groves, G. W., Hasselmann, K. F., Miller, G. R., Munk, W. H., and Powers, W. H. (1966). Propagation of Ocean Swell across the Pacific. *Philosophical Transactions of the Royal Society A: Mathematical, Physical and Engineering Sciences*, 259(1103):431–497.

Stocker, T. F., Qin, D., Plattner, G.-K., Tignor, M. M. B., Allen, S. K., Boschung, J., Nauels, A., Xia, Y., Bex, V., and Midgley, P. (2013). *IPCC 2013: Climate Change 2013: The Physical Science Basis - Working Group I Contribution to the Fifth Assessment Report of the Intergovernmental Panel on Climate Change*. Cambridge University Press, New York.

Tolman, H. L. (2009). User manual and system documentation of WAVEWATCH-IIITM version 3.14. *Technical note*, (3.14):220.

Veeramony, J., Walker, D., and Hsu, L. (2010). A variational data assimilation system for nearshore applications of SWAN. *Ocean Modelling*, 35(3):206–214.

Walker, D. T. (2006). Assimilation of SAR Imagery in a Nearshore Spectral Wave Model. Technical report, Office of Naval Research, Arlington VA.

Wunsch, C. (2006). *Discrete inverse and state estimation problems : with geophysical fluid applications*. Cambridge University Press.